Title
Probing Many-body Localization with a Programmable Superconducting Quantum Processor

Author
Chiaro, Benjamin Thomas

Publication Date
2020

UNIVERSITY of CALIFORNIA
Santa Barbara

Probing Many-body Localization with a Programmable Superconducting Quantum Processor

A dissertation submitted in partial satisfaction of the
requirements for the degree of

Doctor of Philosophy

in

Physics

by

Benjamin Thomas Chiaro

Committee in charge:

Professor John Martinis, Chair

Dr. Pedram Roushan

Professor Ben Mazin

Professor Matthew Fischer

March 2020

The dissertation of Benjamin Thomas Chiaro is approved:

Dr. Pedram Roushan

Professor Ben Mazin

Professor Matthew Fischer

Professor John Martinis, Chair

March 2020

Acknowledgements

The Martinis lab owes its success to the guidance, leadership, and vision of John Martinis. It has been both an honor and a pleasure to have had the opportunity to conduct my Ph.D. studies in his lab. I can't imagine a more thorough, rigorous, comprehensive, or illuminating education. It has been truly transformative.

The greatest gift that an advisor can give his student is to provide a fertile environment in which to study. John's students have all of the critical resources, equipment, and boundless opportunities, but most importantly we become members of a world class team of scientists. The experience of being part of this community is irreplaceable. Thank you.

The success of our project is built on the contributions of each of our team members and depends critically on each person in the lab. Thank you to everyone for your technical contributions, nourishing conversations, and friendship. I'm happy that so many of John's students have remained with the group and also that we've added so many great new members. I'm sure that we have great times ahead!

The first senior scientist that I worked with was Shinobu Ohya. We had the difficult task of developing a new material system (Titanium Nitride) and understanding how to deposit it to make long coherence devices. It was an incredible educational experience to work along-side such a skilled material science expert. I learned a great deal about how to form a comprehensive understanding of a material system during this project. Working with Shinobu during this formative part of my education gave me a solid foundation for my later years, and I continue to benefit from the experience. Thank you Shinobu for your guidance and patience as we worked through one of my first graduate school projects.

John once told me that "Once you have learned to measure noise with a qubit every measurement that you make afterward will be easier" and so far he has been right. In learning to make qubit noise measurements I benefited immensely from the contributions and guidance of Dan Sank. Dan has a sharpness and clarity in his approach to metrology that is hard to find and extremely valuable. He is also generous with his time, especially when a younger student is in need. I've always had a particular fondness for these noise measurements. Dan, thank you for helping me understand this subtle and beautiful subject. I'm forever enriched by this knowledge.

Since I joined the gmon team Charles Neill has been my go-to person for technical questions. Whether I need a quick sanity check on a calculation, help interpreting a data set, or am stuck with direction and need some conceptual brainstorming, a few minutes with Charles generally sorts me out. Charles, thanks for everything, it has been great working with you.

Pedram Roushan has been my day-to-day mentor for the past few years. He has also been my day-to-day friend. Pedram has a deep appreciation for the beauty of physics and it has been a lot of fun to explore quantum dynamics with him. Pedram's no-holds-barred, get things done, the only true laws are the laws of physics, approach to experimental physics is to be admired. It certainly keeps things exciting! Thank you Pedram for your guidance and leadership over these past few years. I see some beautiful physics on the horizon, and a few day trips with our families too.

Mom and Dad if I were to point to a single determining factor in the success of my Ph.D. it would be the Midwestern work ethic that I got from you. I feel that I am the most fortunate person in the world because of all of the opportunities and support that I had growing up. I know that it's not easy to keep two kids in full time activities 12 months per year, in addition to your jobs. We had a lot of fun along the way and you gave me an excellent foundation for a fruitful life. The "Throwback Thursdays" are great reminders of these times and provide continuous inspiration for raising my own family so that I can send Thursday messages to my kids in the future. I can't wait to retrace a few of those summer vacations with Alison, Fiona, Leo, and Naomi.

Many people say that they "would do anything for their children", but few go as far as leaving their jobs and moving across the country for a year just to be a bigger part of their children's lives and help out. Thank you for your continuing support and effort at staying connected with us, whether it is timing your visits for when we have a childcare gap or the weekend video calls that you have with the kids.

Thank you especially for your friendship throughout graduate school. Our phone calls keep me in good spirits and I know that I can count on good advice when I need it most.

Chris and Robin, I appreciate the kindness that you've shown me and especially the help with our kids. The kids always look forward to your weekend video calls. You can't imagine how helpful it is when you make a long weekend visit to help when the kids are out of school. I'm looking forward to more family time after graduation and it will be great to see more of you, whether it's evening card games or activities with the kids. Thank you for your support.

Nick, you're my brother and my best friend. Through thick and through thin, brothers are blood. I'm proud to call you my brother and feel an extra boost of confidence knowing that I have you in my corner. Thanks for your support and friendship, I'm looking forward to spending more time with you after I graduate.

A graduate degree requires as much commitment from the family as from the student. Thank you Alison, Fiona, Leo, and Naomi for making the journey with me. You've brought friendship, joy, and fulfillment into my life. You give me meaning and purpose as well as hope and happiness. I'm very thankful for your contributions and am looking forward to sharing the next phase of life with you all. Having a family is truly life's greatest joy. I love you.

Curriculum Vitæ

Benjamin Thomas Chiaro

Education

2020	Ph.D., Physics Advisor: John Martinis University of California - Santa Barbara
2014	M.A., Physics Advisor: John Martinis University of California, Santa Barbara
2006	B.S., Physics University of Wisconsin - Madison
2002	High School Mt. Horeb High School, Mt. Horeb, WI

Professional Experience

2017 - 2020	Graduate student researcher - On site at Google quantum hardware lab University of California - Santa Barbara
2011 - 2017	Graduate student researcher University of California - Santa Barbara
2010 - 2011	Teaching assistant University of California - Santa Barbara
2008 - 2010	Junior test engineer Opticomp Corporation, Zephyr Cove, NV
2003 - 2006	Student research assistant - Atomic collisions group University of Wisconsin - Madison

Primary publications

“Growth and preservation of entanglement in a many-body localized system”, B. Chiaro, et al. *Submitted* (2019)

“Dielectric surface loss in superconducting resonators with flux-trapping holes”, B. Chiaro, et al. *SUST*, **29** (2016)

“Room temperature deposition of sputtered TiN films for superconducting coplanar waveguide resonators”, S. Ohya, B. Chiaro, et al. *SUST*, **27** (2014)

Abstract

Probing Many-body Localization with a Programmable Superconducting Quantum Processor

by

Benjamin Thomas Chiaro

In many-body localized (MBL) systems, entanglement propagates throughout the system despite the absence of transport. Early experiments have relied on population measurements to indirectly probe these entanglement dynamics. However, because the entanglement results from phase relationships between localized orbitals, it is more naturally probed with phase sensitive algorithms and measurement. In this thesis, we use an array of nearest neighbor coupled superconducting qubits to introduce phase sensitive protocols to the experimental study of MBL systems. We establish that system is MBL by demonstrating disorder induced ergodicity breaking and the presence of effective nonlocal interactions. We then use density matrix reconstructions to observe the hallmark slow growth of entanglement and provide a site-resolved spatial and temporal map of the developing entanglement. We also inspect the capacity of the MBL phase to preserve quantum correlations by observing the decay of distillable entanglement when Bell pair embedded in an MBL environment and dephased by remote excitation.

In superconducting quantum processors, such as that used in the MBL study above, dissipation leads to computational errors and must be minimized. To that end, we also describe coherence engineering experiments in terms of the low power internal quality factor Q_i of coplanar waveguide (CPW) resonators, a figure of merit characterizing dissipation in the quantum computing regime. We investigate titanium nitride as a superconducting base metal for quantum circuits. By optimizing the deposition conditions, we achieve a record low-power Q_i in CPW resonators. We also characterize the dielectric loss due to flux trapping hole arrays. Since flux traps are commonly used to prevent magnetic vortex formation and dielectric loss is a limiting dissipation mechanism, it is important to estimate the contribution of flux traps to the dielectric dissipation budget. We find that for reasonable hole patterns the dielectric loss can be small while preventing vortex formation.

Contents

Chapter 1

Introduction

1.1 Historical context

In 1926 Erwin Schrödinger proposed a wave theory governing the dynamics of microscopic systems.[1] In the succeedng years, quantum mechanics would prove to be extraordinarily accurate in predicting the subtle and surprising behavior of electrons, photons, and atoms alike. Despite the success of the theory, the resulting equations developed a reputation for being unmanagable with only the simplest cases being exactly solvable. For this reason, approximation schemes have been an essential part of quantum physics since the early days. With the developement of computers, numerical methods have become among the most important of these approximation schemes when applying quantum theory to real physical systems. The challenge is that for all but the simplest systems the computational resources required are immense.

For this reason, people have long considered how to efficiently simulate quantum systems using computers. In a 1982 lecture that is often considered the birth of quantum simulation, Richard Feynman suggested that quantum systems could be efficiently simulatable using quantum computational resources.[2] An insight that arose around the same time Feynman's was that the relevance of quantum mechanics is not limited to microscopic objects. In particular, SQUIDs were identified as likely candidates for the observation of macroscoptic quantum tunneling.[3] In 1985, Martinis et al. demonstrated that macroscopic electrical circuits can also behave quantum mechanically and thus form the basis of a superconducting quantum processor.[4] The superconducting quantum bit (qubit), a controllable, macroscopic two level system was demonstrated in 1999. [5]

Since that demonstration, superconducting qubit architectures have continuously improved qubit performance and increased the number of qubits in a processor. This progress culminated in the achievement of quantum supremacy in 2019, when a superconducting quantum processor performed a well defined computational task that is not possible to perform on a modern classical supercomputer.[6] This achievement heralds the onset of an era in which quantum resources can meaningfully contribute to computational tasks considered intractable on classical hardware alone. It is likely that many of the early contributions of quantum computers will be to understanding the behavior of quantum systems, as was originally envisioned by Feynman. In that spirit, the final chapter of this thesis uses a quantum processor as a programmable quantum simulator to probe the entanglement dynamics of a many-body localized system.

1.2 What is a qubit and why is it powerful?

Whereas one classical bit of information can be represented as either 0 or 1, the state of a single ideal qubit can be represented as a vector pointing to the surface of a sphere. This sphere is referred to as the Bloch sphere, and provides excellent physical intuition for the behavior of a qubit.

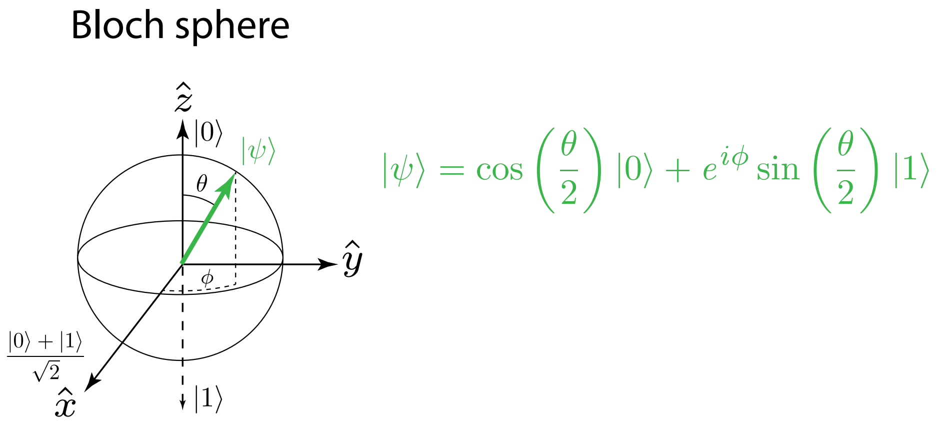

Figure 1.1: Bloch sphere representation of the single qubit density matrix. The states $|\psi\rangle = \cos\left(\frac{\theta}{2}\right)|0\rangle + e^{i\phi}\sin\left(\frac{\theta}{2}\right)|1\rangle$ for $\theta \in [0, \pi]$ and $\phi \in [0, 2\pi]$ are on the surface of the Bloch sphere. The ground state $|0\rangle$ and excited state $|1\rangle$ are located at the North and South poles.

The points at the North and South poles of the Block sphere correspond to the logical $|0\rangle$ and $|1\rangle$. The points away from the poles have amplitude in both the $|0\rangle$ state and the $|1\rangle$ state and are said to be "in superposition". A generic pure state of a single qubit $|\psi\rangle$ can thus be written in terms of the single qubit basis states $|0\rangle$ and $|1\rangle$ as

$$|\psi\rangle = \cos\left(\frac{\theta}{2}\right)|0\rangle + e^{i\phi}\sin\left(\frac{\theta}{2}\right)|1\rangle \tag{1.1}$$

where the angle θ characterizes the relative amplitude between the $|0\rangle$ state and the $|1\rangle$ state, while ϕ characterizes the relative phase between the single qubit basis states.

The ability to encode superposition states in a single qubit suggests that quantum bits provide a mechanism for higher density information encoding than is possible with their classical counterparts. After all, the complete description a pure qubit state requires the specification of θ and ϕ, two continuous variables, rather than the simple one or zero description of a classical bit. However, the true power of a quantum processor comes from the way that multiple qubits combine. For a system of N qubits, the state of the composite system is described by 2^N complex amplitudes. For instance, the state of a two qubit system can be written as

$$|\psi_{2q}\rangle = c_{00}|00\rangle + c_{01}|01\rangle + c_{10}|10\rangle + c_{11}|11\rangle \tag{1.2}$$

The fact that quantum systems combine in this way leads directly to the exponential scaling of the power of a quantum processor. Whereas a classical processor requires four times the physical resources to represent the complex amplitudes c_{00},

c_{01}, c_{10}, c_{11} as it would to represent any one of them, the quantum processor is able to represent them all simultaineously on the same physical qubits. The straightforward - but amazing - consequence is that, roughly speaking, in order to double the capacity of a classical processor you would need to double the number of classical bits. In contrast, if you wish to double the capacity of the quantum processor you only need to add one more qubit. The advantages of the quantum computer over its classical counterpart arise from this ability to store and process exponentially more information in an intrinsically parallel way.

1.3 Challenges

Although there is great promise in quantum computing, there are challenges that must be overcome before a quantum computer can be realized. Foremost among these challenges is that the information in a quantum computer is unstable and prone to degradation. The errors arising from this instability can be roughly divided into two main categories: relaxation and dephasing. These are illustrated in Fig. 1.2.

Relaxation events as illustrated in Fig. 1.2(a), arise when energy is lost from the qubit system. Errors of this variety arise, for example, when a computational photon is absorbed by a parasitic two-level system (TLS)[7]. Relaxation events manifest as unintended downward transistions from the logical $|1\rangle$ state to the $|0\rangle$ state. An example of characterizing this type of dissipation is provided in chapter 4. Dephasing, as illustrated in Fig. 1.2(b), results from an increasing uncertainty in the relative phase between the $|0\rangle$ state and $|1\rangle$ state of the qubit. Errors of this variety arise, for example, as the energy difference between $|0\rangle$ state and $|1\rangle$ state fluctuates in response to random, time varying, magnetic fields. Reducing the noise and dissipation of superconducting qubit devices is a primary research direction and will continue to be for the forseeable future.

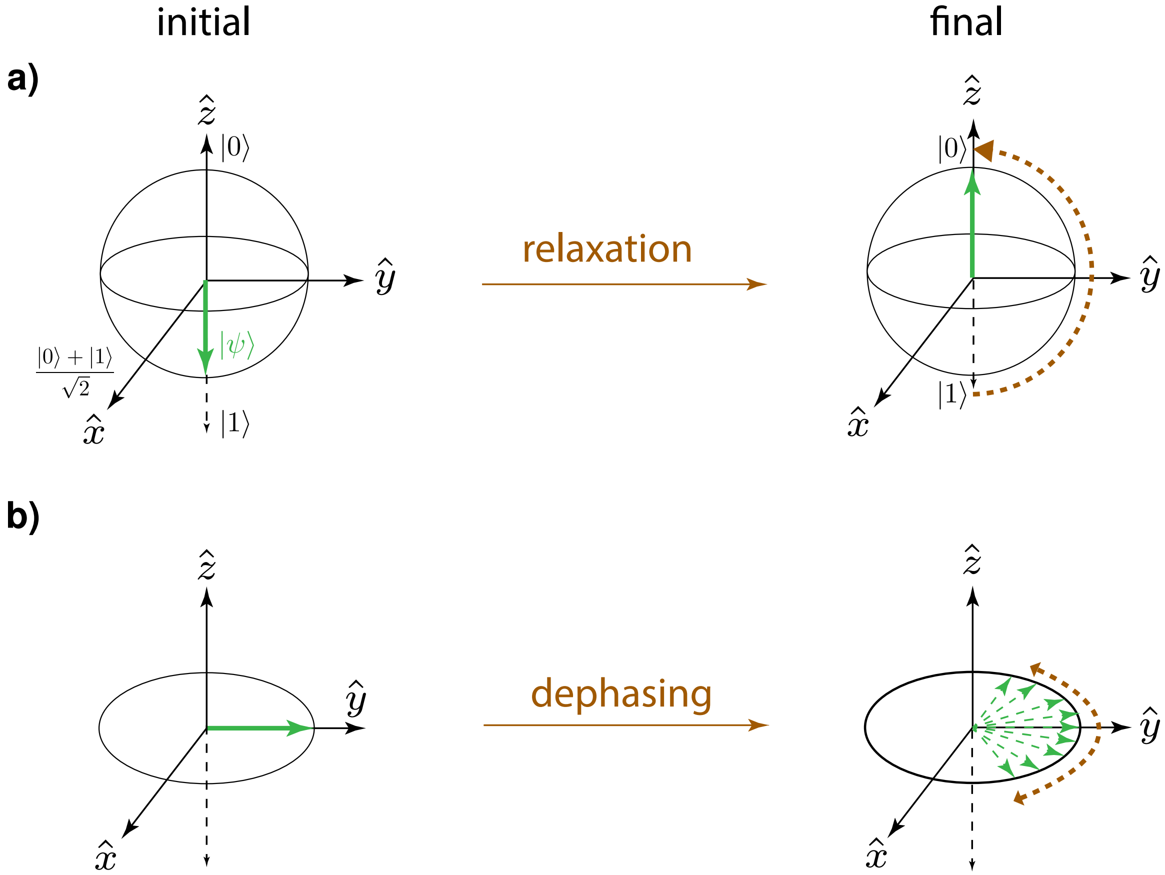

Figure 1.2: a) Schematic of relaxation. Over time the excited state of the qubit $|1\rangle$ tends to decay to the ground state $|0\rangle$ causing a logical error. b) Schematic of dephasing. Over time uncertainty in the phase between the $|1\rangle$ and $|0\rangle$ states grows.

1.4 Overview of this thesis

In this thesis we share contributions to the development of a superconducting quantum processor and demonstrate the use of one as a programmable quantum simulator to probe the phenomenon of many-body localization. In chapter 2, we summarize the essential theory necessary to understand the experiments in the later chapters. In chapter 3, we share a contribution to the basic materials science underlying the construction of a quantum processor by investigating Titanium Nitride, a high kinetic inductance compound superconductor with excellent coherence properties - if made correctly. In chapter 4, we discuss a device characterization where we isolate the excess dielectric loss due to the incorporation of flux trapping hole arrays. These flux traps are commonly used to protect from magnetic vortex loss, but may introduce excess dielectric loss. This is an important consideration as we strive for the longest coherence times possible. Finally, in chapter 5, we perform a system level algorithm demonstration where we use a 9 qubit, nearest-neighbor coupled, linear chain device, featuring tunable qubit frequencies and tunable interqubit coupling to compute the entanglement dynamics of an interacting, localized system.

Chapter 2

Superconducting circuits for quantum computation

In this chapter we give a practical introduction to superconducting circuits for quantum computing applications. The derivations here follow closely those found in refs [8–18]. For completeness we summarize the essential results from these sources as necessary to describe the experiments in this thesis.

2.1 Coplanar waveguide (CPW) resonator

The CPW resonator is a ubiquitious resource in superconducting circuits. Here we state the basic physics of CPW transmission lines, show that an oscillator can be

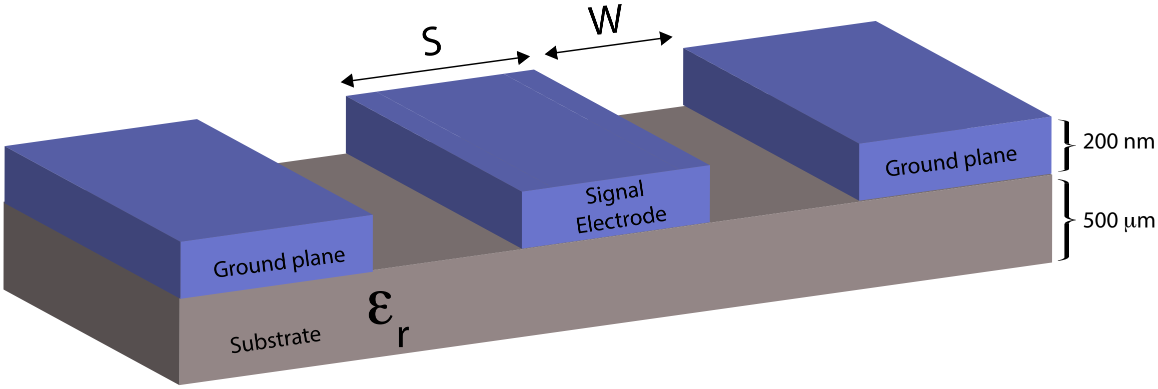

Figure 2.1: A schematic diagram of a coplanar waveguide (CPW), shown in cross section.

made from a terminated strip of transmission line, and outline the relationship of this device with coherence metrology.

2.1.1 The CPW resonator as an LC oscillator

A coplanar waveguide (CPW) transmission line consists of a signal electrode that is isolated from a surrounding ground plane. A cross sectional view of the basic CPW geometry is shown in cross section in fig. 2.1. This device supports a propagating transverse electromagnetic (TEM) mode with phase velocity [8]

$$v_p = \frac{1}{\sqrt{C_l L_l}} \tag{2.1}$$

The capacitance per unit length C_l between the signal electrode and the ground plane is due to the geometry of the electrodes and the relative dielectric constant of the substrate ϵ_r. C_l can be calculated from Schwarz-Christoffel conformal mapping [9], the result is:

$$C_l = \left(\frac{1+\epsilon_r}{2}\right)\epsilon_0 \frac{4K(k)}{K(k')} \tag{2.2}$$

where K is the elleptic integral of the first kind, $k = S/(S+2W)$, and $k' = \sqrt{1-k}$.

The total inductance per unit length L_l consists of the geometric L_g as well as kinetic inductance L_k, which can be significant in superconducting devices.

$$L_l = L_g + L_k \tag{2.3}$$

L_g can be calculated in similar fashion to C_l [9]

$$L_g = \frac{\mu_0}{4}\frac{K\left(k'\right)}{K\left(k\right)} \tag{2.4}$$

The kinetic inductance, due to the inertia of superconducting Cooper pairs, is dependent both on the superconducting material and the geometry of the transmission line.

$$L_k = gL_s \tag{2.5}$$

The surface inductance of the superconductor L_s depends on the normal metal resistivity and the thickness of the electrode. [19]

$$L_s = \frac{\hbar\rho_n}{\pi\Delta_0 t} \tag{2.6}$$

The geometric factor g can be estimated analyticaly for the CPW geometry [9, 10]

$$
\begin{aligned}
g \;=\;& \frac{1}{4S(1-k^2)K^2(k)}\left(\pi + \log\frac{4\pi S}{t} - k\log\frac{1+k}{1-k}\right) + \qquad (2.7)\\
& \frac{k}{4S(1-k^2)K^2(k)}\left(\pi + \log\frac{4\pi(S+2W)}{t} - \frac{1}{k}\log\frac{1+k}{1-k}\right) \qquad (2.8)\\
& \qquad (2.9)
\end{aligned}
$$

For high resistivity superconductors, such as titanium nitride considered in Chapter 3, L_k can be significant and even dominate L_l.

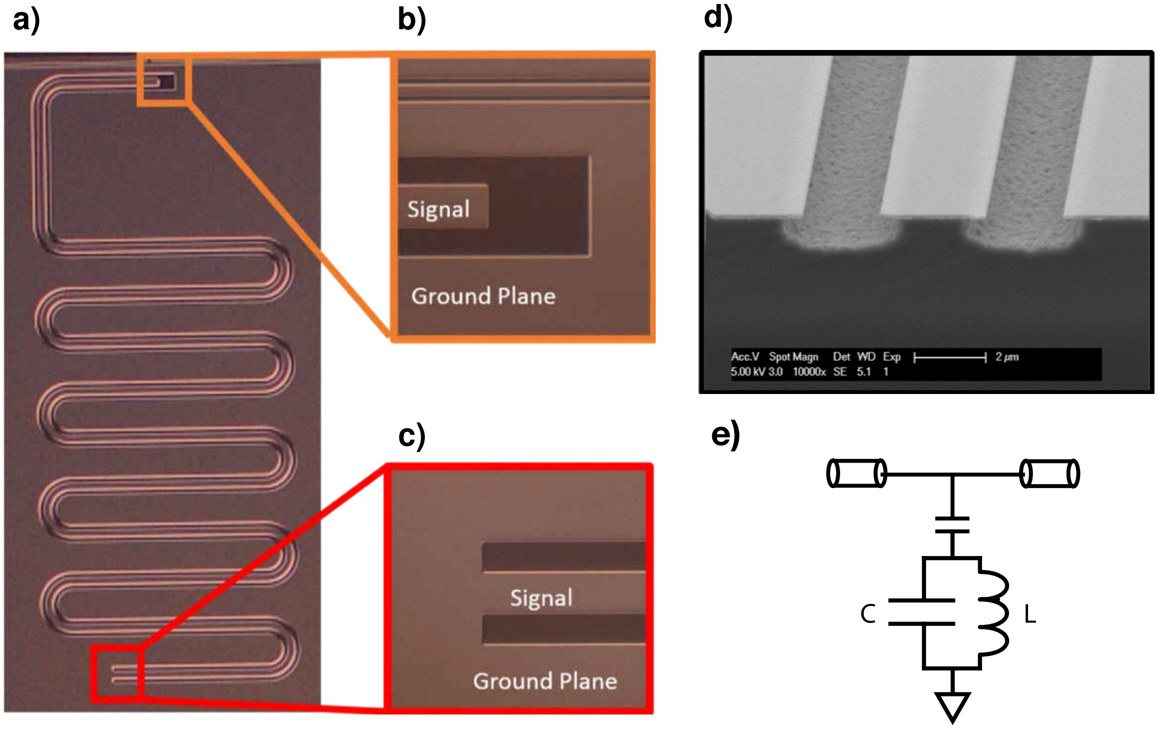

Figure 2.2: a) An optical micrograph of a CPW resonator. b) The voltage antinode of the CPW resonator. c) The voltage node of the CPW resonator. d) A crosssectional SEM image of a CPW resonator. e) The circuit representation of an LC oscillator capacitively coupled to a transmission line.

We can construct a quarter wave resonator by terminating a segment of the transmission line in a short circuit to the ground plane. The physical layout of such a device is the subject of Fig. 2.2. The resonance condition for the quarter wave resonator can be found from the relation $v_p = f\lambda$.

$$f_0 = \frac{1}{4l}\frac{1}{\sqrt{L_l C_l}} \tag{2.10}$$

A consequence of eq. 2.10 is that high kinetic inductance materials can make resonators smaller in size while maintaining a constant frequency resonator. However, eq. 2.10 also implies that in high kinetic inductance devices, the materials parameters (in particular the thin film resistivity) must be tightly controlled to prevent inductance variability.

Following [8], it is apparent that a terminated segment of lossy transmission line should behave like a damped parallel RLC oscillator by inspecting the input impedance of such a line

$$Z_{in} = Z_0 \tanh\left(\alpha + i\beta\right) l = Z_0 \frac{1 - i\tanh\alpha l \cot\beta l}{\tanh\alpha l - i\cot\beta l} \tag{2.11}$$

where α and β are the attenuation and propagation parameters of a TEM wave on the line. For a transmisssion line with small loss and near resonance so that $\omega = \omega_0 + \Delta\omega$ this is approximated as

$$Z_{in} = \frac{1}{1/R + 2i\Delta\omega/2\omega_0} \tag{2.12}$$

which has the same form as Z_{in} for a "lumped circuit" parallel RLC oscillator.

2.1.2 Coherence metrology with CPW resonators

Resonator qubit relationship

The superconducting qubit considered later in this chapter is also a weakly damped LC oscillator. The damping is important because it causes relaxation events of the variety sketched in Fig. 1.2(a), which in turn contribute to the qubit's logical error rate. Thus, in order to achieve the best qubit performance the dissipation must be minimized.

Throughout the history of superconducting qubits the resonator has been used for coherence engineering. This is because superconducting qubits and resonators are subject to many of the same dissipation mechanisms, including quasiparticle loss, magnetic vortex loss, and dielectric loss. This is not surprising given the similarity of their construction. Fig. 2.3(a) shows an Xmon transmon superconducting qubit. It can be thought of as two intersecting strips of CPW transmission line, such as those that create the CPW resonator in Fig. 2.3(c). However, the resonator has the virtue of being much simpler than the qubit. This permits rapid fabrication iterations and protects against the performance degradation that can result from complex multi-step fabrication sequences. For both of these reasons, the resonator is widely used in the material science and fabrication of superconducting quantum circuits.

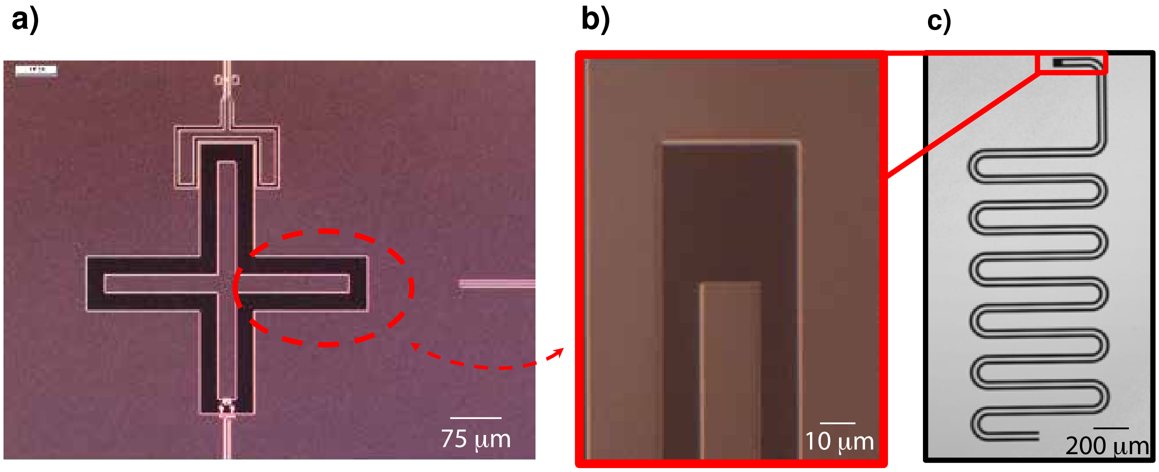

Figure 2.3: a) an Xmon transmon qubit, b) The capacitive end of a $\lambda/4$ resonator. c) The full CPW resonator structure.

Quality factor

The figure of merit describing resonator dissipation is the quality factor Q, which characterizes the rate at which energy stored in the resonator is lost from it. Q is the number of oscillations the circuit performs within one energy relaxation time constant, which can in turn be related to the qubit relaxation time T_1.

$$Q = \frac{\omega E}{P} = \omega T_1 \tag{2.13}$$

The rate at which energy is lost from the resonator depends both on its coupling to external circuitry as well as its internal dissipation so that

$$1/Q_{total} = 1/Q_c + 1/Q_i \tag{2.14}$$

where Q_c and Q_i refer to the coupling and internal quality factors respectively. Note that the quality factors sum in reciprocal since the energy loss rates are additive. The internal quality factor Q_i may be further decomposed in terms of the constituent loss mechanisms.

$$1/Q_i = 1/Q_{quasiparticle} + 1/Q_{vortex} + 1/Q_{dielectric} + ... \tag{2.15}$$

For a quarter wave resonator capacitively coupled to a transmission line, the internal quality factor Q_i and the coupling quality factor Q_c can be extracted separately from simple transmission measurements. This is done by parametrically fitting measurements of transmission S - parameter S_{21} vs frequency[20]

$$S_{21}^{-1} = 1 + \frac{Q_i}{Q_c} \frac{1}{1 + i2Q_i\left(\frac{f-f_0}{f_0}\right)}. \tag{2.16}$$

In chapters 3 and 4 of this thesis we focus on minimizing the internal dissipation $\frac{1}{Q_i}$ to improve the relaxation times of our qubits. Further discussion of the setup of such an experiment can be found in chapter 4 and appendix A.

2.2 Quantum LC Oscillator

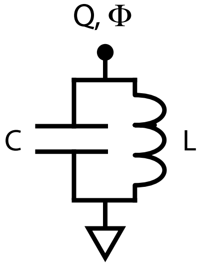

Figure 2.4: An LC oscillator with position and momentum coordinates Φ and Q

The linear LC harmonic oscillator is closely related to the more complicated qubit circuits and provides an excellent starting point for understanding superconducting qubits. At low temperatures the LC oscillator behaves quantum mechanically. As such its dynamics in this regime are described by the Schrödinger equation

$$i\hbar\frac{d}{dt}\left|\psi(t)\right\rangle = H\left|\psi\right\rangle. \tag{2.17}$$

Here we derive the Hamiltonian and show that the LC oscillator behaves as a harmonic oscillator. The derivations here follow closely those found in refs [12–18].

The instantaneous power dissipated by a circuit element is

$$P = IV, \tag{2.18}$$

and therefore the energy stored within a lossless element can be written as

$$E = \int_{t'=t_0}^{t'=t} I(t')V(t')dt', \tag{2.19}$$

where t_0 is normally taken to be $-\infty$, at which time $I(-\infty) = 0$ and $V(-\infty) = 0$.

The customary approach for deriving the Hamiltonian H is to write down the Lagrangian for a generalized coordinate of the circuit and compute H via the Lagendre transformation. This approach ensures that we arrive at a Hamiltonian in terms of a generalized coordinate and it's conjugate momentum. We choose the flux Φ, indicated in Fig. 2.4, as our generalized coordinate. Φ is also known as the node flux or branch flux. Φ is defined in terms of the voltage across the inductor.

$$\Phi(t) = \int_{-\infty}^{t} V(t')\,dt' \tag{2.20}$$

The current I and voltage V at the node are simply related to Φ

$$I = \Phi/L \tag{2.21}$$

$$V = \dot{\Phi} \tag{2.22}$$

We can also write the energy of the capacitor and inductor in terms of Φ.

$$E_{capacitor} = \int_{t'=t_0}^{t'=t} I(t')\,V(t')\,dt' = \int_{t'=t_0}^{t'=t} C\frac{dV}{dt'}\,V(t')\,dt' = \frac{1}{2}CV^2 = \frac{1}{2}C\dot{\Phi}^2 \tag{2.23}$$

and

$$E_{inductor} = \int_{t'=t_0}^{t'=t} I(t')\,V(t')\,dt' = \int_{t'=t_0}^{t'=t} I(t')L\frac{dI}{dt'}\,dt' = \frac{1}{2}LI^2 = \frac{1}{2L}\Phi^2 \tag{2.24}$$

By associating the potential energy with the position dependent term and the kinetic energy with the velocity dependent term we can write the Lagrangian for the system

$$\mathcal{L} = \mathcal{T} - \mathcal{U} = \frac{1}{2}C\dot{\Phi}^2 - \frac{\Phi^2}{2L} \tag{2.25}$$

We calculate the momentum conjugate to Φ by differentiating the Lagrangian.

$$\frac{\partial \mathcal{L}}{\partial \dot{\Phi}} = C\dot{\Phi} = CV = Q \tag{2.26}$$

We recognize the conjugate momentum as the charge on the capacitor and hence denominate it Q. The Hamiltonian H is obtained from $\mathcal{L}$ as

$$H = Q\dot{\Phi} - \mathcal{L} = C\dot{\Phi}^2 - (\frac{1}{2}C\dot{\Phi}^2 - \frac{\Phi^2}{2L}) = \frac{1}{2}C\dot{\Phi}^2 + \frac{\Phi^2}{2L} \tag{2.27}$$

or

$$H = \frac{1}{2}CV^2 + \frac{1}{2}LI^2 \tag{2.28}$$

which is the sum of the electric energy stored in the capacitor and the magnetic energy stored in the inductor.

The quantum mechanical Hamiltonian for the electrical LC oscillator can be obtained by substituting the flux and charge operators $\hat{\Phi}$ and $\hat{Q}$ in place of classical coodinate Φ and momentum Q in Eq. 2.27.

$$H = \frac{\hat{Q}^2}{2C} + \frac{\hat{\Phi}^2}{2L} \tag{2.29}$$

We recognize this as the Hamiltonian of a harmonic oscillator in the charge and flux coordinates. Thus the device inherits the properties of a harmonic oscillator. The operators representing the conjugate variables obey the commutation relation

$$\left[\hat{\Phi}, \hat{Q}\right] = i\hbar \tag{2.30}$$

Additionally, we get the familiar ladder of energy levels.

$$E_n = \hbar\omega_0 \left(n + \frac{1}{2} \right) \tag{2.31}$$

Where we have introduced the characteristic frequency

$$\omega_0 = \frac{1}{\sqrt{LC}} \tag{2.32}$$

We can also express the annihiliation and creation operators in terms of the charge and flux operators:

$$\hat{a} = \frac{1}{\sqrt{2\hbar Z_0}} \left(\hat{\varPhi} + i\hat{Q}Z_0 \right) \tag{2.33}$$

and

$$\hat{a}^\dagger = \frac{1}{\sqrt{2\hbar Z_0}} \left(\hat{\varPhi} - i\hat{Q}Z_0 \right) \tag{2.34}$$

where we have introduced the characteristic impedance

$$Z_0 = \sqrt{\frac{L}{C}} \tag{2.35}$$

The Hamiltonian is often expressed in terms of the annihilation and creation operators:

$$H = \hbar\omega_0 \left(\hat{a}^\dagger \hat{a} + \frac{1}{2} \right) = \hbar\omega_0 \left(\hat{n} + \frac{1}{2} \right) \tag{2.36}$$

The use of the number operator $\hat{n} = \hat{a}^\dagger \hat{a}$ makes it clear that the eigenstates of the system are Fock states corresponding to the number of photonic excitations in the oscillator. The equal spacing of the energy levels makes the linear harmonic oscillator unusable as a qubit because we cannot drive the $|0\rangle \rightarrow |1\rangle$ transition independently of the $|1\rangle \rightarrow |2\rangle$ and higher transitions since all of the transitions are at the same frequency. This challenge is resolved by introducing nonlinearity into the circuit by incorporating a Josephson inductance.

It is convenient to write H in terms of the number of charges on the island $\hat{n}$ and the phase across the inductor $\hat{\phi}$.

$$\hat{n} = \frac{\hat{Q}}{2e} \tag{2.37}$$

$$\hat{\phi} = \frac{2\pi\hat{\Phi}}{\Phi_0} \tag{2.38}$$

where e is the electronic charge and we have introduced the magnetic flux quantum

$$\Phi_0 = \frac{h}{2e} \tag{2.39}$$

We define the charging energy as

$$E_c = \frac{e^2}{2C} \tag{2.40}$$

and the inductive energy

$$E_L = \frac{\Phi_0^2}{4\pi^2 L} \tag{2.41}$$

In these coordinates

$$H = 4E_c\hat{n}^2 + \frac{1}{2}E_l\hat{\phi}^2 \tag{2.42}$$

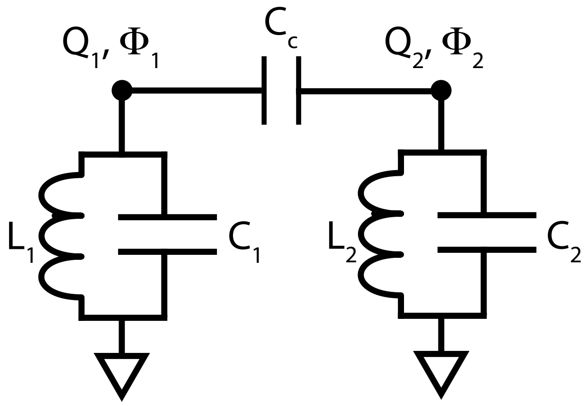

Figure 2.5: Two capacitively coupled LC oscillators

2.3 Coupled resonators

The advantages of quantum computing stem from the exponential scaling of the Hilbert space dimension as we combine quantum systems. Useful quantum circuits, therefore, must provide a means for multiple qubits to interact. For superconducting qubits the coupling mechanism may be either capacitive or inductive in nature. In this section we show how these coupling mechanisms lead to a hopping term in the Hamiltonian. The derivations here follow closely those found in refs [12–18].

2.3.1 Capacitive coupling

The circuit diagram for two capacitively coupled oscillators is shown in Fig. 2.5. Maintaining the convention of associating the node fluxes Φ with potential energy and the node charges Q with kinetic energy, we can immediately write down the Lagrangian for the capacitively coupled system.

$$\mathcal{L} = \mathcal{T} - \mathcal{U} = \left[\frac{1}{2}C_1\dot{\mathit{\Phi}}_1^2 + \frac{1}{2}C_2\dot{\mathit{\Phi}}_2^2 + \frac{1}{2}C_c\left(\dot{\mathit{\Phi}}_1 - \dot{\mathit{\Phi}}_2\right)^2\right] - \left[\frac{1}{2L_1}\mathit{\Phi}_1^2 + \frac{1}{2L_2}\mathit{\Phi}_2^2\right] \tag{2.43}$$

Which can be written as

$$\mathcal{L} = \frac{1}{2}\dot{\boldsymbol{\Phi}}^T\boldsymbol{C}\dot{\boldsymbol{\Phi}} - \frac{1}{2}\boldsymbol{\Phi}^T\boldsymbol{L}^{-1}\boldsymbol{\Phi} \tag{2.44}$$

Where

$$\boldsymbol{\Phi} = \begin{bmatrix}\mathit{\Phi}_1\\ \mathit{\Phi}_2\end{bmatrix}, \boldsymbol{C} = \begin{bmatrix}C_1 + C_c & -C_c\\ -C_c & C_2 + C_c\end{bmatrix}, \text{ and } \boldsymbol{L} = \begin{bmatrix}L_1 & 0\\ 0 & L_2\end{bmatrix} \tag{2.45}$$

We find the conjugate momenta by differentiating the Lagrangian:

$$Q_1 = \frac{\partial\mathcal{L}}{\partial\dot{\mathit{\Phi}}_1} = C_1\dot{\mathit{\Phi}}_1 + C_c(\dot{\mathit{\Phi}}_1 - \dot{\mathit{\Phi}}_2) \tag{2.46}$$

$$Q_2 = \frac{\partial\mathcal{L}}{\partial\dot{\mathit{\Phi}}_2} = C_2\dot{\mathit{\Phi}}_2 + C_c(\dot{\mathit{\Phi}}_2 - \dot{\mathit{\Phi}}_1) \tag{2.47}$$

We can solve for the $\dot{\mathit{\Phi}}$ in terms of the Q_i by writing the above expressions as a matrix equation.

$$\begin{bmatrix}Q_1\\ Q_2\end{bmatrix} = \begin{bmatrix}C_1 + C_c & -C_c\\ -C_c & C_2 + C_c\end{bmatrix}\begin{bmatrix}\dot{\mathit{\Phi}}_1\\ \dot{\mathit{\Phi}}_2\end{bmatrix} \tag{2.48}$$

or

$$Q = C\dot{\mathit{\Phi}} \tag{2.49}$$

We can invert this expression to get the $\dot{\Phi}_1$ and $\dot{\Phi}_2$ in terms of the cannonical momenta of the coupled system.

$$\begin{bmatrix} \dot{\Phi}_1 \\ \dot{\Phi}_2 \end{bmatrix} = \mathbf{C}^{-1}\mathbf{Q} = \frac{1}{(C_1 + C_c)(C_2 + C_c) - C_c^2} \begin{bmatrix} C_2 + C_c & C_c \\ C_c & C_1 + C_c \end{bmatrix} \begin{bmatrix} Q_1 \\ Q_2 \end{bmatrix} = \begin{bmatrix} C_{11}^{-1} & C_{12}^{-1} \\ C_{21}^{-1} & C_{22}^{-1} \end{bmatrix} \begin{bmatrix} Q_1 \\ Q_2 \end{bmatrix} \tag{2.50}$$

We can write the Lagrangian in terms of the Q_i. Since:

$$Q = C\dot{\Phi} \implies \dot{\Phi} = C^{-1}Q \tag{2.51}$$

and

$$\dot{\Phi}^T = \left(C^{-1}Q\right)^T \implies \dot{\Phi}^T = Q^T {C^{-1}}^T \implies \dot{\Phi}^T = Q^T C^{-1} \tag{2.52}$$

Now we can write the lagrangian in terms of the node fluxes and the conjugate charges.

$$\mathcal{L} = \frac{1}{2}Q^T C^{-1} Q - \frac{1}{2}\Phi^T L^{-1} \Phi \tag{2.53}$$

which is explicitly written as

$$\begin{aligned} \mathcal{L} &= \frac{1}{2}\begin{bmatrix} Q_1 & Q_2 \end{bmatrix} \begin{bmatrix} C_{11}^{-1} & C_{12}^{-1} \\ C_{21}^{-1} & C_{22}^{-1} \end{bmatrix} \begin{bmatrix} Q_1 \\ Q_2 \end{bmatrix} - \frac{1}{2}\begin{bmatrix} \Phi_1 & \Phi_2 \end{bmatrix} \begin{bmatrix} \frac{1}{L_1} & 0 \\ 0 & \frac{1}{L_2} \end{bmatrix} \begin{bmatrix} \Phi_1 \\ \Phi_2 \end{bmatrix} && (2.54) \\ &= \frac{1}{2}\left[C_{11}^{-1}Q_1^2 + C_{12}^{-1}Q_1 Q_2 + C_{21}^{-1}Q_1 Q_2 + C_{22}^{-1}Q_2^2\right] - \left[\frac{1}{2L_1}\Phi_1^2 + \frac{1}{2L_2}\Phi_2^2\right] && (2.55) \end{aligned}$$

The Hamiltonian is

$$H = \sum_i \dot{x}_i \frac{\partial \mathcal{L}}{\partial \dot{x}_i} - \mathcal{L} = \sum_i \dot{x}_i p_i - \mathcal{L} = \sum_i \dot{\Phi}_i Q_i - \mathcal{L} \tag{2.56}$$

We can compute the sum by 2.50 and 2.53 into 2.56

$$\dot{\Phi}_1 Q_1 + \dot{\Phi}_2 Q_2 = (C_{11}^{-1} Q_1 + C_{12}^{-1} Q_2) Q_1 + (C_{21}^{-1} Q_1 + C_{22}^{-1} Q_2) Q_2 \tag{2.57}$$

So that

$$H = \frac{1}{2} \left[C_{11}^{-1} Q_1^2 + 2 * C_{12}^{-1} Q_1 Q_2 + C_{22}^{-1} Q_2^2 \right] + \left[\frac{1}{2L_1} \Phi_1^2 + \frac{1}{2L_2} \Phi_2^2 \right] \tag{2.58}$$

This Hamiltonian is the Hamiltonian of two harmonic oscillators with increased effective capacitances and the addition of a charge - charge interaction. The third term $C_{12}^{-1} Q_1 Q_2$ is the charge - charge interaction that permits excitations to transfer (swap) between qubits. Using the Harmonic oscillator relations in eqns 2.33 and 2.34

$$Q_1 Q_2 = (-i) \sqrt{\frac{\hbar}{2Z_0^1}} (a_1 - a_1^\dagger)(-i) \sqrt{\frac{\hbar}{2Z_0^2}} (a_2 - a_2^\dagger) = -\frac{\hbar}{2} \frac{1}{\sqrt{Z_0^1 Z_0^2}} (a_1 a_2 + a_1^\dagger a_2^\dagger - a_1 a_2^\dagger - a_2 a_1^\dagger) \tag{2.59}$$

The non photon conserving terms eliminated by the rotating wave approximation since they oscillate rapidly, and quickly average to zero.

$$Q_1 Q_2 \sim (a_1 a_2^\dagger + a_1^\dagger a_2) \tag{2.60}$$

Written in this way it is clear that the capacitive charge - charge coupling mediates a swapping interaction.

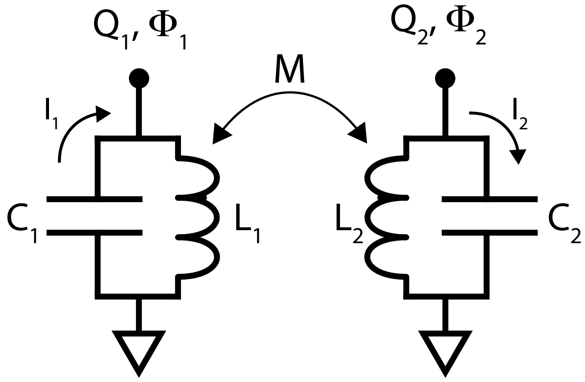

Figure 2.6: Two inductively coupled LC oscillators

2.3.2 Inductive coupling

The gmon circuit considered in this work features fixed capacitive coupling as described above in combination with a tunable inductive coupling. Fig. 2.6 shows the case of two inductively coupled oscillators. In this case we expect to generate a flux - flux interaction term in the Hamiltonian.

By the definition of mutual inductance we have

$$\Phi_1 = L_1 I_1 + M I_2, \tag{2.61}$$

$$\Phi_2 = L_2 I_2 + M I_1. \tag{2.62}$$

Which can be written as a matrix equation

$$\begin{bmatrix} \Phi_1 \\ \Phi_2 \end{bmatrix} = \begin{bmatrix} L_1 & M \\ M & L_2 \end{bmatrix} \begin{bmatrix} I_1 \\ I_2 \end{bmatrix} \tag{2.63}$$

Which implies

$$I = L^{-1}\Phi = \frac{1}{L_1L_2 - M^2}\begin{bmatrix} L_2 & -M \\ -M & L_1 \end{bmatrix}\begin{bmatrix} \Phi_1 \\ \Phi_2 \end{bmatrix} = \begin{bmatrix} L_{11}^{-1} & L_{12}^{-1} \\ L_{21}^{-1} & L_{22}^{-1} \end{bmatrix}\begin{bmatrix} \Phi_1 \\ \Phi_2 \end{bmatrix} \tag{2.64}$$

The energy in the inductors is written in terms of the flux variable is

$$E_{inductor} = \frac{1}{2}\mathbf{I}^T\mathbf{L}\mathbf{I} = \frac{1}{2}\Phi^T L^{-1}\Phi \tag{2.65}$$

The energy in the capacitors is the same as in the uncoupled case:

$$E_{capacitor} = \frac{1}{2}C_1\dot{\Phi_1}^2 + \frac{1}{2}C_2\dot{\Phi_2}^2 \tag{2.66}$$

The full Lagrangian is

$$\mathcal{L} = \left[\frac{1}{2}C_1\dot{\Phi_1}^2 + \frac{1}{2}C_2\dot{\Phi_2}^2\right] - \left[L_{11}^{-1}\Phi_1^2 + L_{12}^{-1}\Phi_1\Phi_2 + L_{21}^{-1}\Phi_1\Phi_2 + L_{22}^{-1}\Phi_2^2\right] \tag{2.67}$$

The conjugate momenta are

$$Q_1 = \frac{\partial\mathcal{L}}{\partial\dot{\Phi}_1} = C_1\dot{\Phi}_1 \tag{2.68}$$

$$Q_2 = \frac{\partial\mathcal{L}}{\partial\dot{\Phi}_2} = C_2\dot{\Phi}_2 \tag{2.69}$$

And finally the Hamiltonian is

$$H = \sum_i \dot{\Phi}_i Q_i - \mathcal{L} = \frac{Q_1^2}{2C_1} + \frac{Q_2^2}{2C_2} + L_{11}^{-1}\Phi_1^2 + 2 * L_{12}^{-1}\Phi_1\Phi_2 + L_{22}^{-1}\Phi_2^2 \tag{2.70}$$

This is again the Hamiltonian for a harmonic oscillator, but this time with a flux - flux coupling term $L_{12}^{-1}\Phi_1\Phi_2$ Since $\Phi = 2\sqrt{\frac{\hbar Z_0}{2}}(a^\dagger + a)$ and involking the RWA again, we find

$$\Phi_1\Phi_2 \sim (a_1 a_2^\dagger + a_1^\dagger a_2) \tag{2.71}$$

so that the flux - flux coupling also generates a hopping term in the Hamiltonian.

2.4 Josephson junction

As noted above the linear LC oscillator is not suitable for use as a qubit because of its ladder of equally spaced energy levels. This challenge is addressed by using the nonlinear inductance of a Josephson junction in place of the linear inductance considered above. This nonlinearity creates an unevenly spaced ladder of energy levels and gives rise to an interaction term in the Hamiltonian. The Josephson junction provides us with a lossless, nonlinear inductance.[21] The Josephson junction consists of two superconducting electrodes separated by a thin insulating barrier. This is illustrated in Fig. 2.7. The Josephson relations for the current through the junction I_j and the voltage across the junction V to the phase:

$$I_j = I_c \sin\delta \tag{2.72}$$

and

$$V = \frac{\Phi_0}{2\pi}\frac{d\delta}{dt} \tag{2.73}$$

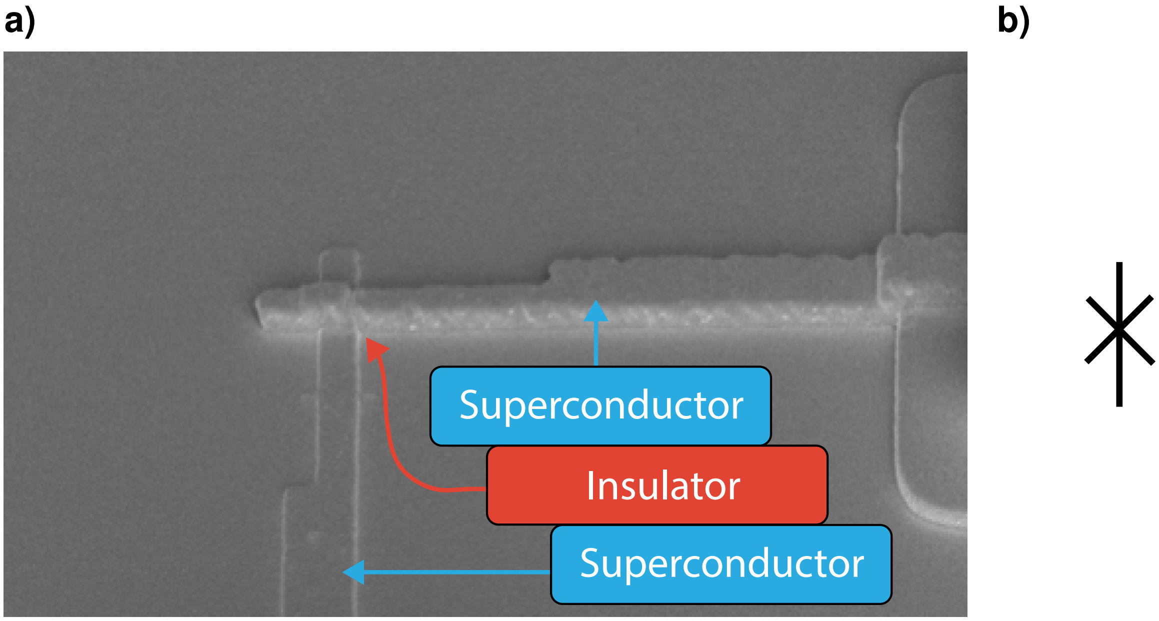

Figure 2.7: a) A Josephson junction b) The circuit symbol for a Josephson junction

from these we can compute the Josephson inductance

$$V = L\frac{dI}{dt} \implies L_j = \frac{\Phi_0}{2\pi I_c \cos\delta} \tag{2.74}$$

The parameter I_c is known as the critical current, which is the maximum supercurrent that the junction can support. The critical current is related to the normal resistance of the junction via the Ambegaokar - Baratoff Relation [22]

$$I_c R_n = \frac{\pi \Delta}{2e} \tanh\left(\frac{\Delta}{2k_b T}\right) \tag{2.75}$$

As the Josephson junction is dissipationless, work done on the junction is stored as energy within it. We can compute this energy from the Josephson relations above.

$$-\frac{dU}{dt} = IV = \big(I_c \sin\phi(t)\big)\left(\frac{\hbar}{2e}\frac{d\phi}{dt}\right) \tag{2.76}$$

$$-\int dU = I_c \frac{\hbar}{2e} \int \sin\phi d\phi \tag{2.77}$$

$$U = E_J \cos\phi, \quad E_J = I_c \frac{\hbar}{2e} \tag{2.78}$$

We can configure two Josephson junctions in parallel to form a DC squid. This device behaves as a Josephson junction with a critical current that is tunable with magnetic flux. The effective critical current of the DC squid is [15]

$$I_c(\varPhi_{ext}) = 2I_c \left| \cos \frac{\pi \varPhi_{ext}}{\varPhi_0} \right| \tag{2.79}$$

The tunability of the SQUID inductance forms the basis for frequency tunable superconducting qubits and coupling circuits that provide an adjustable interaction strength between the qubits. Such frequency and coupling tunability are essential capabilities for quantum simulations such as that in chapter 5 of this thesis.

2.5 Transmon superconducting qubits

The transmon is a variety of superconducting qubit that is realized by replacing the linear inductance of an LC oscillator with a Josephson junction. The resulting device can be thought of as a Josephson junction with a large shunting capacitance, making it a weakly anharmonic LC oscillator. The idea behind the transmon is that the shunting capacitance exponentially surpresses charge noise by trading away anharmonicity[16].

In 2011, a 3D version of the transmon was developed at Yale and demonstrated remarkable coherence properties.[23] This is due to the fact that the geometry of the device made it possible to store most of the qubit mode energy in the lossless vacuum, reducing dissipation. Challenges of this 3D implementation are that they are too large to scale easily, cannot be microfabricated, and it is difficult to retain the coherence properties when coupling two or more of these devices together. In 2013, planar variant of the transmon, compatible with standard microfabrication techniques and ammenable to scaled-up multi-qubit systems, was introduced.[24] Future iterations saw the device incorporate tunable inter-qubit coupling (gmon).[25] This design is the basis for the processor used in the quantum simulation of chapter 5 of this thesis.

2.5.1 Hamiltonian of the transmon

We obtain the transmon Hamiltonian by substituting the Josephson junction energy from Eq. 2.78 into the LC oscillator Hamiltonian Eq. 2.42 in place of the linear inductor energy.

$$H = 4E_c\hat{n}^2 - E_j \cos\hat{\phi} \tag{2.80}$$

A key point here is that increasing the capacitance decreases the charging energy. Thus by forming the oscillator with a large capacitor the device is less sensitive to fluctuations in the charge.

The nonlinear Josephason inductance slightly modifies the level structure of our (nearly) harmonic oscillator so that the energy levels are no longer evenly spaced. This has at least two important consequences. 1) For uncoupled qubits, we can drive the $|0\rangle$-$|1\rangle$ transition without exciting the $|1\rangle$-$|2\rangle$ transition. 2) The nonlinearity gives rise to a Hubbard interaction term in the Hamiltonian. This interaction is fundamental to the design of entangling gates between transmon qubits, is essential to integrability breaking in analog algorithms, and leads directly to the many-body entanglement propagation in the localized phase that we observe in the last chapter.

2.5.2 Nonlinearity of the transmon

Following [13, 16] we can compute the nonlinearity of the transmon from perturbation theory. For the purposes of our MBL simulation the nonlinearity gives rise to a Hubbard interaction and facilitates entanglement propagation without excitation transport. The large E_j/E_c ratio of the transmon motivates an expansion of the cosine potential in ϕ about $\phi = 0$. With this expansion the potential energy is

$$U = -E_j + E_j\left(\phi^2/2\right) - E_j\left(\phi^4/24\right) \tag{2.81}$$

The quadratc term combines with the term quadratic in the charge to give a harmonic oscilator with level spacing $\sqrt{8E_cE_j}$. The quartic term is responsible for the nonlinearity to leading order.

$$H = \sqrt{8E_cE_j}(a^\dagger a + 1/2) - E_j - E_c/12(a + a^\dagger)^4 \tag{2.82}$$

Here the a, $a^\dagger$ are the standard harmonic oscillator annihilation and creation operators operators. From perturbation theory, the first order correction to the energies for level n coming from the quartic term is is

$$\delta E_n = \langle n| \delta_H |n\rangle = E_c/12 \langle n| |(a + a^\dagger)^4| |n\rangle \tag{2.83}$$

$$\langle n| |a^2 a^{\dagger 2} + a^\dagger a a^\dagger a + a^\dagger a a a^\dagger + a a^\dagger a^\dagger a + a a^\dagger a a^\dagger + a^{\dagger 2} a^2| |n\rangle \tag{2.84}$$

$$\delta E_n = E_c/12 \left(6n^2 + 6n + 3\right) \tag{2.85}$$

2.6 Composite gmon Hamiltonian.

More complex devices, such as the gmon circuit employed in Chapter 5, can be understood by combining the concepts in the preceding sections [26]. A circuit schematic for the gmon is shown in fig. 2.8. The frequency detuning term $h_i \hat{n}_i$ can be understood as the energy of an LC harmonic oscillator with frequency h_i. The correction to the harmonic oscillator Hamiltonian due to the nonlinearity of the Josephson junctions

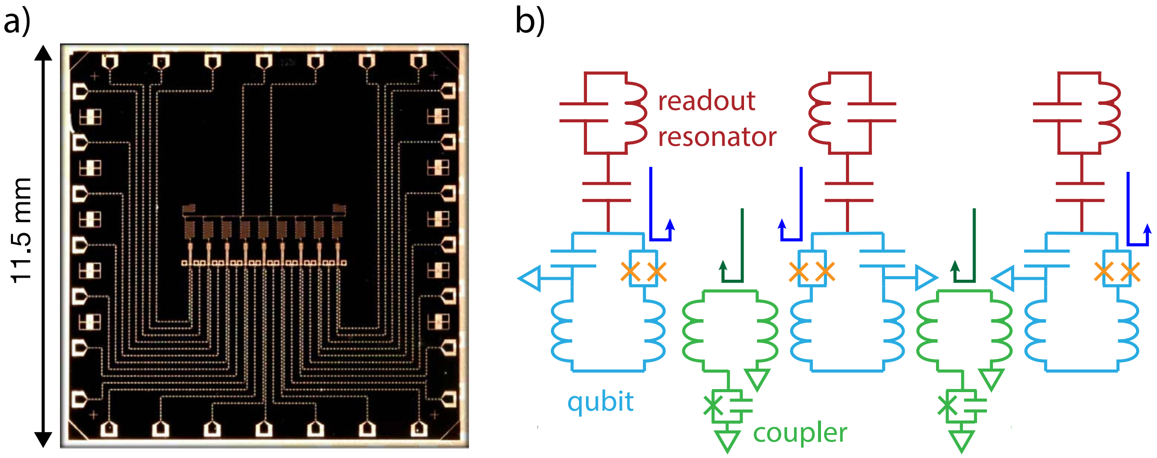

$$H_{BH} = \underbrace{\sum_{i}^{N_{coupler}} J_{i,i+1}\left(a_i^{\dagger} a_{i+1} + a_i a_{i+1}^{\dagger}\right)}_{\text{coupling (hopping)}} + \underbrace{\sum_{i}^{N_{qubit}} h_i n_i}_{\text{frequency detuning}} + \underbrace{\frac{U}{2}\sum_{i}^{N_{qubit}} n_i(n_i - 1)}_{\text{qubit nonlinearity}}$$

Figure 2.8: a) An optical micrograph of a gmon device. b) Circuit schematic for 3 qubit subsection of the gmon. c) The resulting Bose-Hubbard Hamiltonian that describes the gmon dynamics.

is represented by term $\frac{U}{2}\hat{n}(\hat{n}-1)$. It should be noted that this can be thought of as a single term in an expansion, it gives 0 for $n_i = 0, 1$ and U for $n = 2$. This expression is not valid for higher occupations. Finally, the hopping term $J(a_i a_{i+1}^{\dagger} + a_i^{\dagger} a_{i+1})$ arises from the sum of direct capacitive coupling between the qubits and inductive coupling mediated by the coupler circuit shown in green. In Appendix B, we provide benchmarking data confirming that the dynamics of the gmon circuit are described by the Bose-Hubbard Hamiltonian shown in fig. 2.8.

Chapter 3

Room temperature deposition of sputtered TiN films for superconducting coplanar waveguide resonators[1]

3.1 Introduction

Superconducting coplanar-waveguide (SCPW) resonators are used for photon detection and quantum information processing. Recently, there has been a growing

---

[1] This chapter was published as: "Room temperature deposition of sputtered TiN films for superconducting coplanar waveguide resonators",S. Ohya, B. Chiaro, et al. SUST **27**, 015009 (2014)

interest in titanium nitride (TiN) thin films due to their widely tunable critical temperature T_c, large surface inductance, and ability to produce high intrinsic quality-factor Q_i resonators.[27–38] Although excellent performance has been achieved with TiN SCPW resonators, their loss mechanisms are still not clear due to the complex properties of TiN. TiN films are known to absorb contaminants when they are exposed to air.[39–41] In fact, a high concentration of oxygen, up to ∼20%, has been reported in TiN films.[42–44] Since the contaminants absorbed from the air are strong candidates for two-level systems (TLSs) that can cause degradation in the performance of superconducting devices[7], a systematic investigation of the film quality of TiN is quite important. Although many studies have been done on TiN since the 1980's, it remains difficult to relate sputtering conditions to the properties of the resulting films and there is little information linking the film properties to the performance of microwave electronic devices made from the films. Here, we show a detailed analysis focusing on stoichiometric $Ti_{1-x}N_x$ films (x=0.5) obtained by adjusting the N_2 flow rate. We show that the kinetic energy of the sputtered TiN particles, which is a function of the pressure, radial position, and target-substrate (T-S) distance, plays a crucial role in determining film properties such as strain, resistivity, grain structure, crystallographic texture, and contaminant levels. We find that the quality factors of resonators made from TiN depend strongly on the material properties of the thin films. Specifically, we find the low power Q_i to be correlated with reduced film strain and increased O content. We find that resonators with a low power $Q_i > 10^6$ can be reliably produced from low film strain TiN.

3.2 Film preparation

TiN films were deposited by DC reactive magnetron sputtering in an ultra-high vacuum deposition chamber (AJA International, Inc.) with a background pressure in the lower 10^{-10} Torr range. This system has a high-vacuum load lock chamber connected to the main deposition chamber. We used a 6-inch gun with a 99.995% purity, 4-inch Ti target. The substrate and target face one another and are centered on a common axis. Ultra-high purity (99.9999%) Ar and N_2 gas sources were introduced to the deposition chamber through Micro Torr purifiers (SAES Pure Gas, Inc.). All depositions were done at room temperature with a fixed Ar flow rate of 15 sccm and with a constant DC plasma power of 600 W. Under these conditions the nominal incident energy of Ar^+ ions on the Ti target is from 350 to 380 eV, depending on the deposition pressure and N_2 flow rate. During deposition, the substrate holder was rotated at ∼30 rpm. No substrate bias was applied. We used high-resistivity Si(001) substrates (>10,000 Ω cm, Addison Engineering, Inc.) for all depositions. Before installing a Si substrate in the load lock, the substrate was cleaned with Nano-Strip (Cyantek Corp, Inc.) for 10 minutes, followed by buffered-HF cleaning for 1 minute to remove any native oxide and terminate the Si surface with hydrogen. We installed the Si substrate in the load lock as quickly as possible after cleaning, typically within 45 minutes. Before deposition of TiN, the Ti target was pre-sputtered for 2 minutes with the same conditions as for the subsequent TiN deposition. In sections 3.3 to 3.5 of this paper, we used a fixed target-substrate (T-S) distance of 88 mm, whereas in section 3.6, we investigated the effect of the T-S distance on the properties of the TiN films. Film thicknesses varied from 100 to 900 nm.

3.3 Basic properties

Figure 3.1(a)-(c) shows the N_2 flow-rate dependence of the TiN thin film room temperature resistivity, T_c, and composition x, defined as the N content divided by the sum of the Ti and N contents. The film thickness, T_c, and x were measured by scanning electron microscopy (SEM), a Physical Property Measurement System (Quantum Design, Inc.), and Rutherford Back Scattering (RBS), respectively. Using RBS we can determine the film composition with an error of 1-2%. In the RBS measurements, we detected Ti, N, C, and O signals. We did not see any clear Ar signal, which was previously reported in sputtered TiN films.[45] Resistivity values were measured within several hours of deposition. Although a gradual evolution in the film oxygen content has been reported over the timescale of 100 hours after deposition[41], our films only show 7% increase in resistivity one month after deposition, which means that our films are relatively stable. We measured T_c and x several weeks after deposition. Here, the films were deposited on quarter pieces of 3-inch Si wafers. All measurements were done near the center of these pieces.

Increasing the N_2 flow rate increases the N concentration on the target surface, which increases x. By comparing Fig. 3.1(a) with (c), we see that the resistivity minimum corresponds to the stoichiometric condition (x=0.5) regardless of deposition pressure. This is consistent with previous studies of TiN carried out at a relatively low deposition pressure.[46, 47] Our results show that the resistivity minimum of the resistance vs. N_2 flow at constant pressure curve is a good indicator of the stoichiometric point even with a high contamination density. This is important because in section 3.4 it will be shown that resistivity is a strong function of O content which varies from ~0.1% to ~10% over this pressure range. We note that the lowest resistivity film obtained in this study was 34.2 $\mu\Omega$ cm. This is a typical value obtained for TiN films deposited at room temperature and slightly higher than single-crystal TiN (18 $\mu\Omega$ cm).[48] In Fig. 3.1(b), T_c increases and saturates at 4.5 K while increasing the N_2 flow rate. As x increases in $Ti_{1-x}N_x$, the dominant phase of the film is changed from Ti_2N, whose T_c is 50 mK, to TiN, with T_c around 5.6 K.[49–51] This phase change can explain the steep change of T_c when x<0.5. In Fig. 3.1(b), we see that the T_c of the stoichiometric TiN film decreases by increasing the deposition pressure, which we believe is due to the increase in contaminant concentrations discussed in

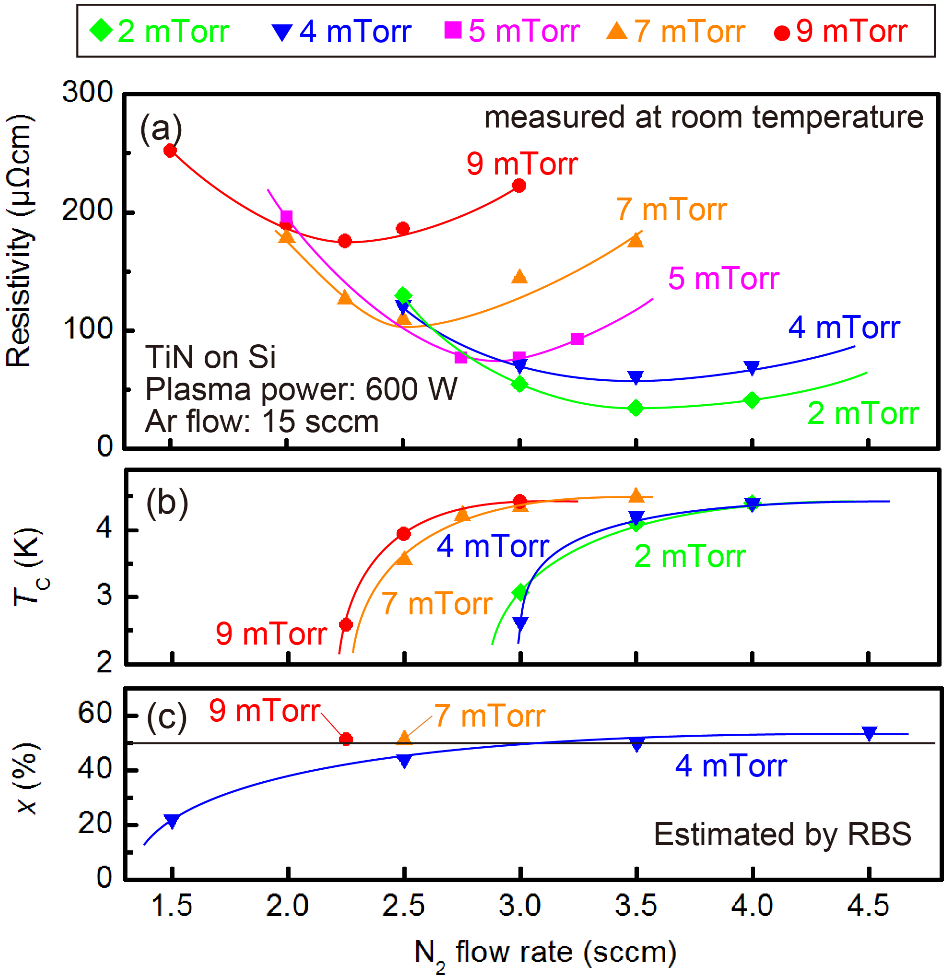

Figure 3.1: (Color) N_2 flow-rate dependence of the (a) room-temperature resistivity, (b) T_c, and (c) x of $Ti_{1-x}N_x$ films deposited at 2, 4, 5, 7, and 9 mTorr, where we estimated x by using RBS. The curves are guides for eyes. All of these depositions were done at room temperature with the Ar flow rate fixed at 15 sccm and the plasma power of 600 W. For the measurements of the resistivity and T_c, the film thickness was ∼200 nm for the TiN films deposited at 2 mTorr and was ∼100 nm for others.

section 3.4 (See Fig. 3.1 with the N_2 flow rate at 3.5, 3.5, 2.5, and 2.25 sccm when the deposition pressure is 2, 4, 7, and 9 mTorr, respectively).

In Fig. 3.1(a), the resistivity rises substantially when increasing the deposition pressure, and the stoichiometric point shifts to a smaller N_2 flow rate. The resistivity increase can be explained by the morphology and contamination changes discussed below. The shift of the stoichiometric point is probably due to the effect of the Ar neutrals reflected from the Ti target to the substrate during sputtering. These neutrals have the same order of mean free path as the sputtered particles,[52] and re-sputter the TiN film surface during the deposition. It is known that the film surface is always covered with a stable N-rich TiN thin layer due to the high reactivity of atomic N, which has an important role in determining the N content of the film. When the reflected Ar neutrals have a high energy at a low deposition pressure, re-sputtering by the Ar neutrals removes this N-rich surface. However, at high pressure, this effect becomes less important due to the higher collision probability of the Ar neutrals, so stoichiometric TiN is obtained at a smaller N_2 flow rate as the deposition pressure increases.[53]

3.4 Properties of stoichiometric films

In this section, we focus on nearly stoichiometric $Ti_{1-x}N_x$ films ($x \simeq 0.5$). Films were deposited by setting the N_2 flow rate at 3.5, 3.5, 3.0, 2.5, and 2.25 sccm when the deposition pressure was 2, 4, 5, 7, and 9 mTorr, respectively. These N_2 flow rates correspond to the resistivity minimum points in Fig. 3.1(a). We fixed the Ar flow rate at 15 sccm and the T-S distance at 88 mm.

Figure 3.2(a) and (b) show SEM images of the stoichiometric TiN films for deposition pressures of 2 and 9 mTorr, respectively. The incident electron-beam direction is tilted by 70° from the film-surface normal. These images were taken near the center of the substrates (quarter pieces of 3-inch Si wafers). We see that these TiN films are polycrystalline with columnar grains. In the film deposited at 2 mTorr, these grains are intimately bound to their neighbors. In contrast, in the film deposited at 9 mTorr, the grain boundaries are clear, and the surface is rough. The grain boundaries seen in (b) are thought to allow contaminants into the film, which is consistent with the increase in the C + O concentration from 0.3% at 2 mTorr to 13.5% at 9 mTorr, as shown in table 3.1.

The morphology change due to the pressure increase is similar to the effect of the application of a substrate bias, which has been well studied previously.[39] The grains tend to bind as the negative substrate-bias voltage becomes larger. It is known that the atomic peening mechanism leads to a dense structure [as in Fig. 3.2(a)], where the gas atoms reflected from the target with a high momentum pack together the sputtered atoms and increase the density of atoms in each column.[54] This effect is more significant at lower pressure, where the reflected atoms have higher momenta.

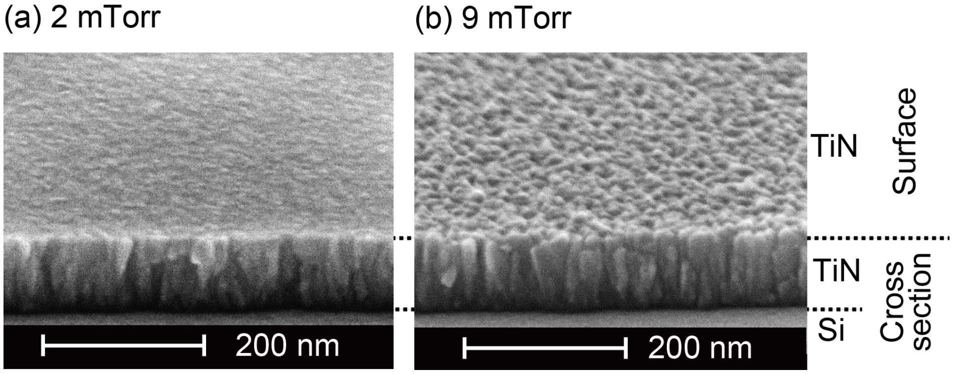

Figure 3.2: (Color online) SEM images of the stoichiometric TiN films deposited at (a) 2 and (b) 9 mTorr. The incident SEM electron-beam direction is tilted by 70° from the film-surface normal.

The higher momentum of the sputtered particles at a lower pressure also can help to make such a dense structure.

The relatively high-atomic-density TiN columns obtained in a low pressure deposition generate a large stress in the film. Figure 3.3(a) shows the deposition pressure dependence of the in-plane stress in 100-nm thick stoichiometric TiN films. The strain values were determined with a wafer bow measurement (FLX-2320, KLA Tencor, Inc.) at the center of the TiN films deposited on 3-inch Si wafers at room temperature. When the deposition pressure is low, the film has a strong in-plane compressive strain. By increasing the deposition pressure, the in-plane strain is reduced and changes to a weak tensile strain. This is a very common feature in films deposited by sputtering and is consistent with the SEM results shown in Fig. 3.2.

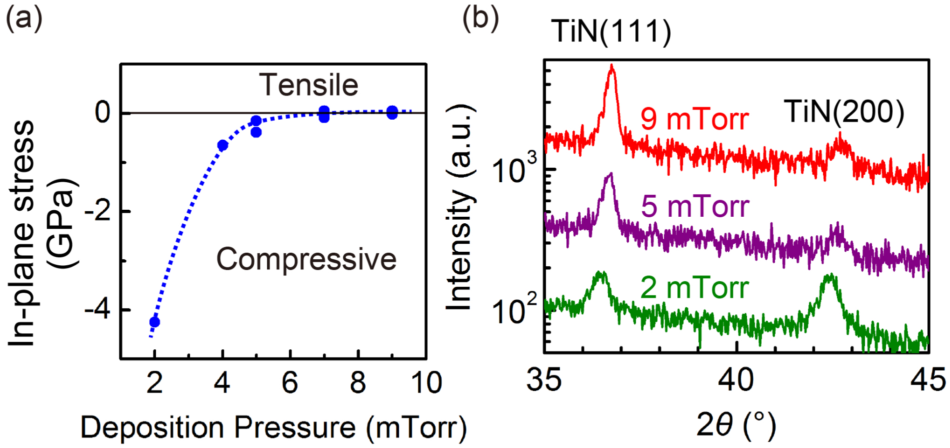

Figure 3.3: (Color online) (a) Stress measured in the stoichiometric TiN films as a function of the deposition pressure. The stress values shown here were measured at the center of 3-inch wafers. (b) The ω-2θ x-ray diffraction scans of 200-nm-thick stoichiometric TiN films deposited at 2, 5, and 9 mTorr (from bottom to top).

Figure 3.3(b) shows x-ray diffraction ω-2θ scans of the 200-nm-thick stoichiometric TiN films deposited at 2, 5, and 9 mTorr (from bottom to top). In all the spectra, we see two peaks at ∼36.5° and ∼42.5° corresponding to the TiN(111) and (200) planes, respectively. The only other peaks detected in our stoichiometric TiN films were from the Si substrate. With increasing pressure, these TiN peaks shift toward larger angles, and the (111) peak becomes sharper. The lattice constants in the surface-normal direction estimated from these peaks are 0.4260 nm at 2 mTorr and 0.4237 nm at 9 mTorr (corresponding to a 0.5% decrease in the lattice constant). Since the intrinsic lattice constant of TiN is 0.424 nm, these values are consistent with the tendency of the stress to change as seen in Fig. 3.3(a).

By increasing the deposition pressure, the dominant crystal orientation changes from (200) to (111). As the mobility of the adatoms is increased by decreasing the deposition pressure, they tend to make closer-packed structures. Thus, the high adatom mobility causes the crystal growth along the (200) orientation, which has the lowest surface free energy.[55]

We carried out x-ray texture measurements on the 200-nm-thick stoichiometric TiN films, which give us a more complete understanding of the crystallinity of these films. Figure 3.4(a) shows the schematic x-ray beam alignment in our measurements. We define ϕ as the in-plane angle between the Si in-plane <110> axis and the x-ray beam plane [the pink plane in Fig. 3.4(a)], whereas ψ expresses the angle between the measurement direction (broken orange line) and the surface normal of the film. Figure 3.4(b) and (c) show the measurement results of the TiN films deposited at 2 mTorr, when θ is fixed at 36.66° corresponding to TiN(111), and at 42.61° corresponding to TiN(200), respectively. We see that the (111) and (200) planes are nearly parallel to the film surface (corresponding to the center yellow zones). The ψ direction of these planes fluctuates slightly (ψ=0-20°). As can be seen in the SEM image of Fig. 3.2(a), the growth directions of the grains are not perfectly aligned in the surface normal direction but have some fluctuation, so these ψ distributions observed in the x-ray texture measurements are probably due to these grains' tilt. In addition, we see that there are randomly oriented (111) and (200) planes (many red areas). Figure 3.4(d)

Table 3.1: Ar and N_2 flow rates used to deposit nearly stoichiometric TiN films, and the concentrations of C and O relative to the sum of the Ti and N content. The C and O concentrations were estimated from SIMS intensities integrated over the film thickness, using RBS data of the TiN film deposited at 9 mTorr as a reference.

Pressure (mTorr)	Flow rate (sccm)		Concentration (%)	
	Ar	N_2	C	O
2	15	3.5	0.2	0.1
4	15	3.5	0.9	0.6
7	15	2.5	3.6	8
9	15	2.25	2.5	11

and (e) show the same measurement results on the TiN film deposited at 9 mTorr. In this case, (111) planes nearly parallel to the film surface become dominant. The (200) planes observed at ψ=40-70° are thought to be the same crystal phase with the (111) plane observed at the center in (d). From these results, we see that the (111) plane is selectively grown in the growth direction in the high pressure condition with a ψ fluctuation up to $\sim$20°.

Figure 3.5(a)-(d) shows the secondary ion mass spectroscopy (SIMS) results from the TiN films deposited at 2, 4, 7, and 9 mTorr. The thicknesses of these films are 200, 100, 100, and 100 nm, respectively. These TiN films were deposited on quarter pieces of 3-inch Si substrates. We etched the film from the surface toward the Si substrate with different etching rates depending on the sample. The Si interface is identified by the increase in the Si signal. Here, all the signals are normalized by the intensity of TiN in the TiN-layer region in each graph. Thus, we can directly compare the relative concentrations between the samples. We note that the low level

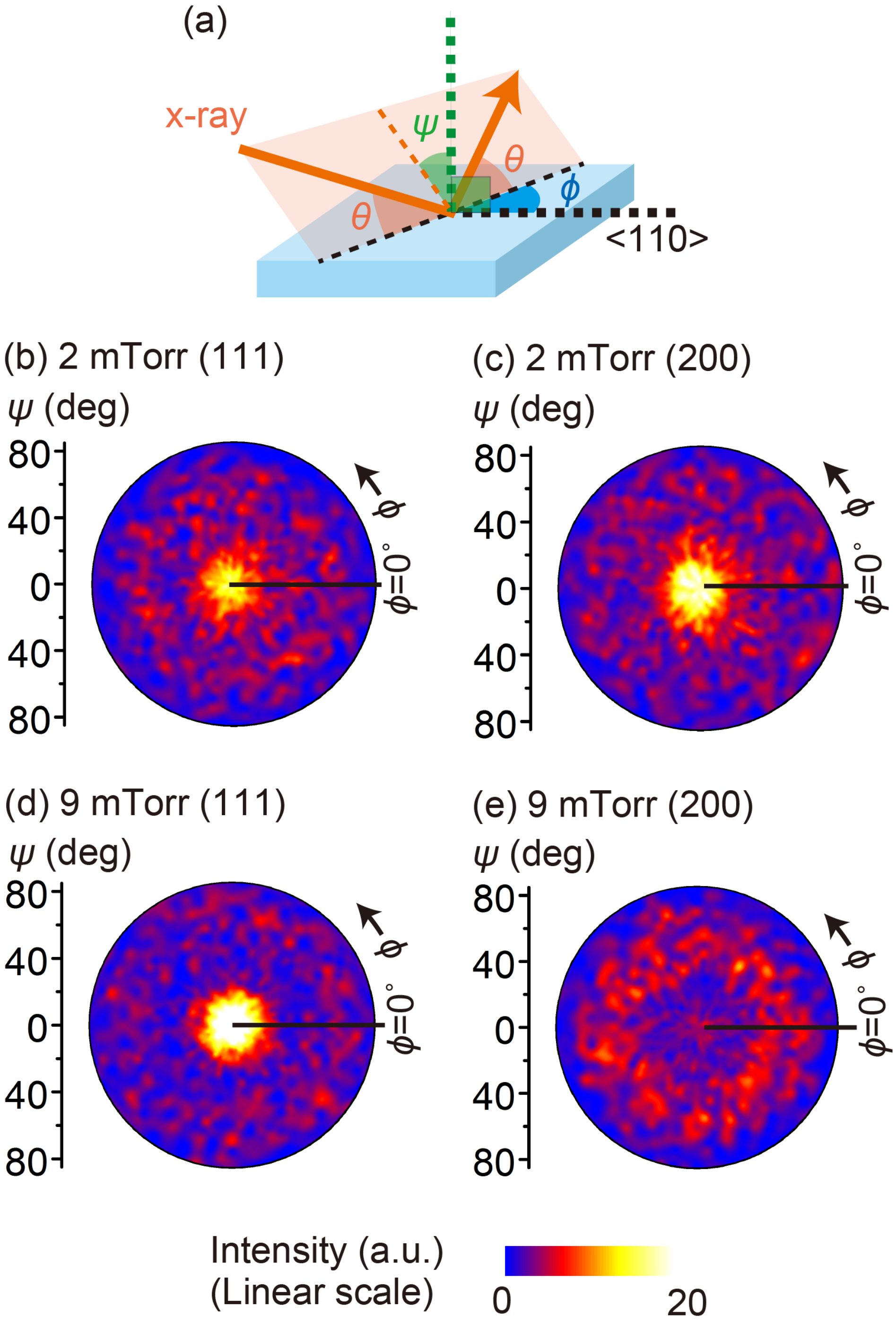

Figure 3.4: (Color) (a) Schematic x-ray beam alignment in our texture measurements. (b), (c) Results of the texture measurements on the stoichiometric TiN film deposited at 2 mTorr when θ is fixed at (b) 36.66° and (c) 42.61°. (d), (e) The same measurement results when the deposition pressure is 9 mTorr.

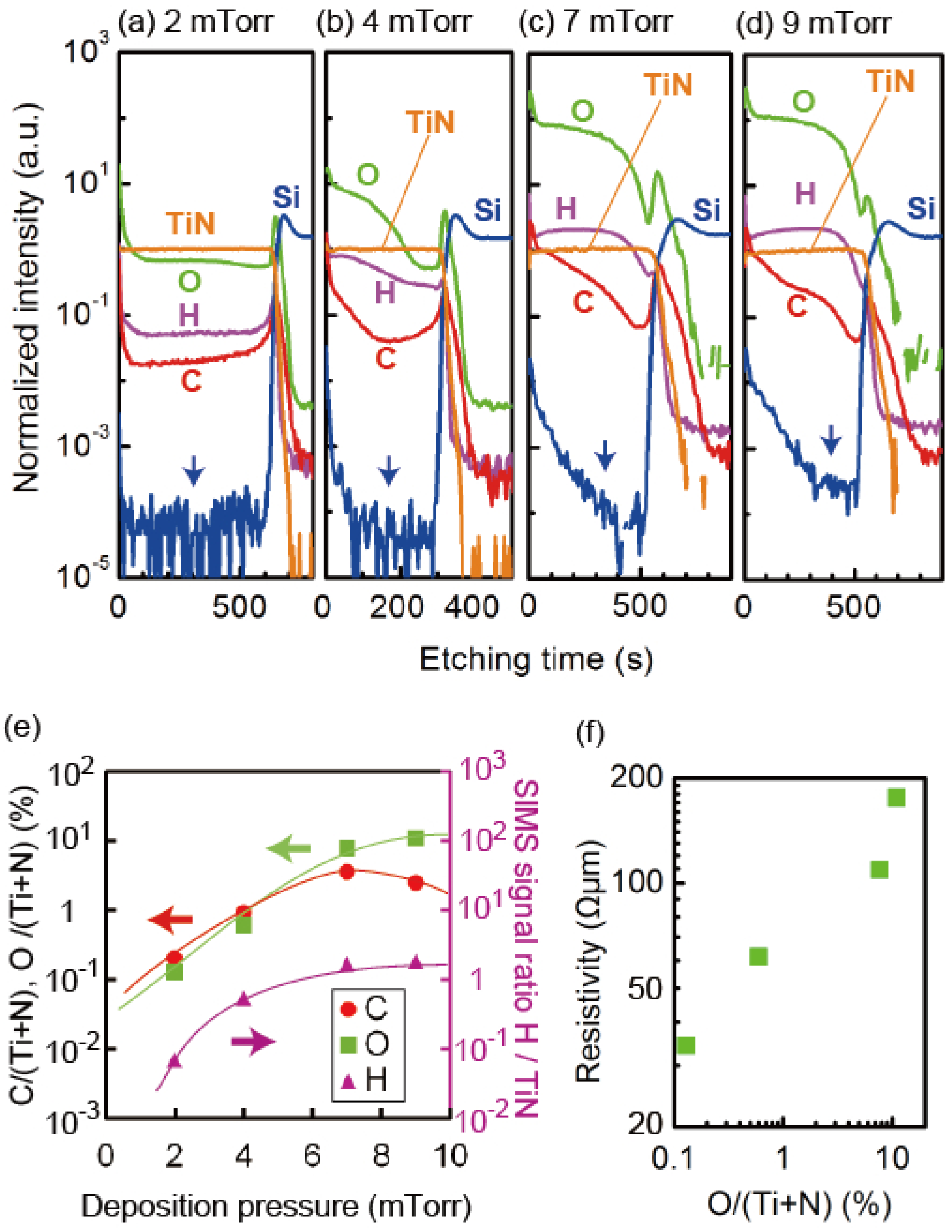

Figure 3.5: (Color) SIMS depth profile of the stoichiometric TiN films deposited at (a) 2 mTorr, (b) 4 mTorr, (c) 7 mTorr, and (d) 9 mTorr as a function of the Ar^+ etching time from the surface toward the Si substrate. We show the SIMS signals of the H, C, O, Si, and TiN. Here, all the signals are normalized by the intensity of TiN in the TiN-layer region. (e) Deposition pressure dependence of the concentrations of H, C and O. Since it is difficult to determine the H content, we plot the integrated SIMS intensity of H over the thickness divided by that of TiN. The actual concentrations of C and O were estimated from the total SIMS signals in (a)-(d) using the RBS data of the TiN film deposited at 9 mTorr as a reference. (f) The dependence of resistivity on O content for the nearly stoichiometric TiN films.

signals of Si in the TiN layer (see the arrows) are not coming from Si, but probably coming from a contaminant that has the same mass number (29) as is used to detect Si, such as COH. The concentrations of H, C, and O strongly increase with increasing deposition pressure. The TiN films incorporate the contaminants when they are exposed to air after deposition.[41] We have observed this directly by witnessing the films change color from the golden color of stoichiometric TiN to the green color of titanium oxynitride as the load lock is being vented.

From our RBS measurements on the 100-nm thick TiN film deposited at 9 mTorr, C and O contents relative to the sum of the Ti and N contents are estimated to be 2.5% and 11%, respectively. Using these values and integrating the SIMS intensities shown in Fig. 3.5(a)-(d), we can estimate the contamination levels of C and O as shown in Table 3.1. The deposition pressure dependence of these concentrations is shown in Fig. 3.5(e). As shown in Fig. 1, the resistivity increases and T_c decreases as the deposition pressure is increased; this change is likely due to rising contaminant levels in the TiN. In Fig. 3.5(f) we show the strong dependence of resistivity on oxygen content, indicating that the regulation of oxygen content is essential to the control of the electronic properties of the film.

As shown in Fig. 3.2, the grain boundaries become more defined as the deposition pressure increases, and the surface area, which can absorb the contaminants, becomes larger as a consequence. It has been reported that x-ray photoemission spectroscopy measurements on sputtered TiN films show a Ti $2p_{3/2}$ peak at 458 eV which corresponds to TiO_2,[41] which suggests that some of the O atoms may enter the TiN crystal and react with Ti atoms. Under high pressure conditions, bonds between Ti and N become weak due to the low kinetic energy of the sputtered particles, which is also thought to be the origin of such a high level of contaminants in the TiN films deposited at high pressure.

3.5 In-plane distribution

As shown above, the TiN film properties directly depend on the kinetic energy of the sputtered particles, which can be controlled by deposition pressure. In magnetron sputtering, the in-plane energy distribution of the sputtered particles is inevitable because there is an in-plane inhomogeneity of the plasma intensity caused by the spatial variation of the magnetic field from the magnetron. Figure 3.6(a) shows the cross-sectional SEM images of a stoichiometric TiN film deposited on a 3-inch Si(001) wafer at 7 mTorr. We show the images taken at 6-35 mm from the center of the wafer. There is a similar tendency seen in the pressure dependence; the grain boundary becomes clearer from the center to the edge. In Fig. 6(b), we show the measured sheet resistance R_{sheet} (blue circles) and the film thickness (red triangles) as a function of the distance from the center of the wafer. We see that the film thickness is reduced by 5% from 890 to 850 nm, whereas, R_{sheet} increases by 70% from 1.5 to 2.5

Ω. This large increase in R_{sheet} cannot be explained by the 5% thickness reduction alone.

Figure 3.7 (a)-(d) shows the SIMS depth profiles of TiN, H, C, and O on the stoichiometric TiN film deposited at 7 mTorr. The solid curves are the SIMS intensities at the center, and the dotted curves are the ones at the edge of the 3-inch wafer. Here, we show the raw data. We see that the TiN contents are the same between at the center and at the edge. However, all the contaminant levels are higher at the edge than those at the center. This suggests that the in-plane energy distribution of the sputtered particles causes the large distribution of the resistance as well as the contamination.

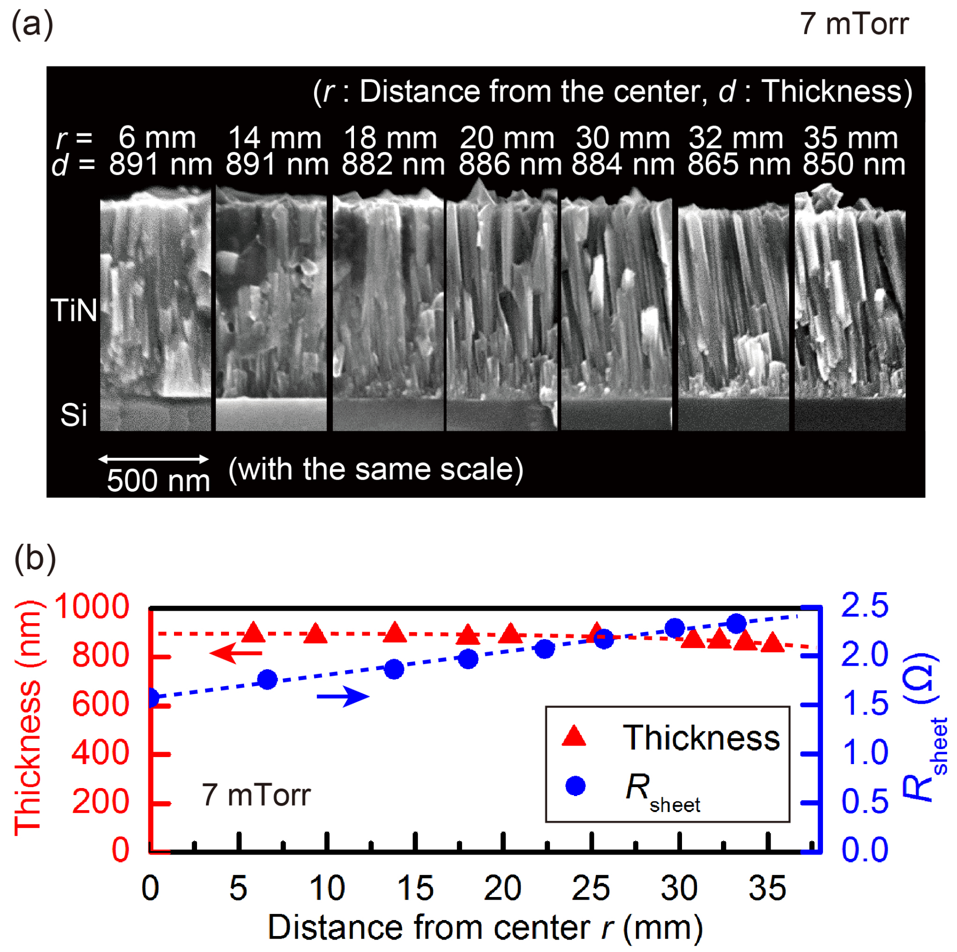

Figure 3.6: (Color online) (a) Cross-sectional SEM images of the stoichiometric TiN film deposited at 7 mTorr on a 3-inch Si(001) wafer. Here, we show the images taken at positions from 6 to 35 mm measured from the center of the wafer. (b) R_{sheet} (red triangles) and film thickness (blue circles) as a function of the distance from the center of the wafer.

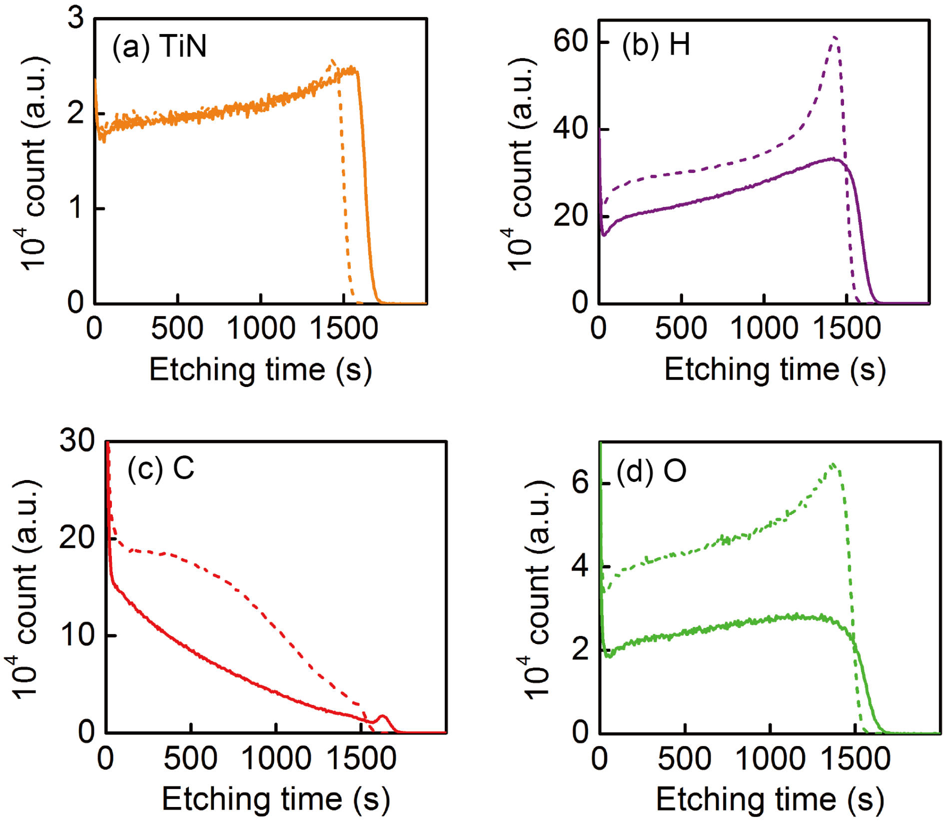

Figure 3.7: (Color online) SIMS depth profiles of (a) TiN, (b) H, (c) C, and (d) O obtained in the stoichiometric TiN film deposited at 7 mTorr. The solid curves are those at the center, and the dotted curves are the ones at the edge of the 3-inch wafer.

3.6 Target - Substrate (T-S) distance dependence

The energy of the sputtered particles just before reaching the film surface also depends on the T-S distance. The sputtered particles experience more collisions for larger T-S distances. Here, we studied the effect of the T-S distance on film quality. The orange (triangle) and blue (inverse triangle) points in Fig. 3.8 show the resistivities of the TiN films as a function of the N_2 flow rate when the T-S distance was 266 mm and the deposition pressure was 7 and 4 mTorr, respectively. As a reference, we show the films deposited at 4 mTorr with a T-S distance of 88 mm (the same T-S distance as was used for all depositions of the TiN films shown in the previous sections). The resistivity becomes two orders of magnitude higher as the T-S distance is changed from 88 to 266 mm. The films deposited with a large T-S distance (288 mm) have a green color, which is the typical color of titanium oxynitride (TiNO). By carrying out RBS analysis on the film deposited at 7 mTorr with a N_2 flow rate of 3 sccm and a T-S distance of 266 mm, the carbon and oxygen contents are estimated to be 5% and 27%, respectively. We found that the color of these films was gold just after the deposition when they are still in the vacuum chamber. However, while venting the load lock with N_2 gas (purity: 99.999%) with TiN samples inside, the film color was observed to change from gold to green. This shows that the grain boundary surfaces of the TiN films are highly reactive since H, C, and O were gettered from the nearly pure N_2. This result indicates that TiN films deposited with

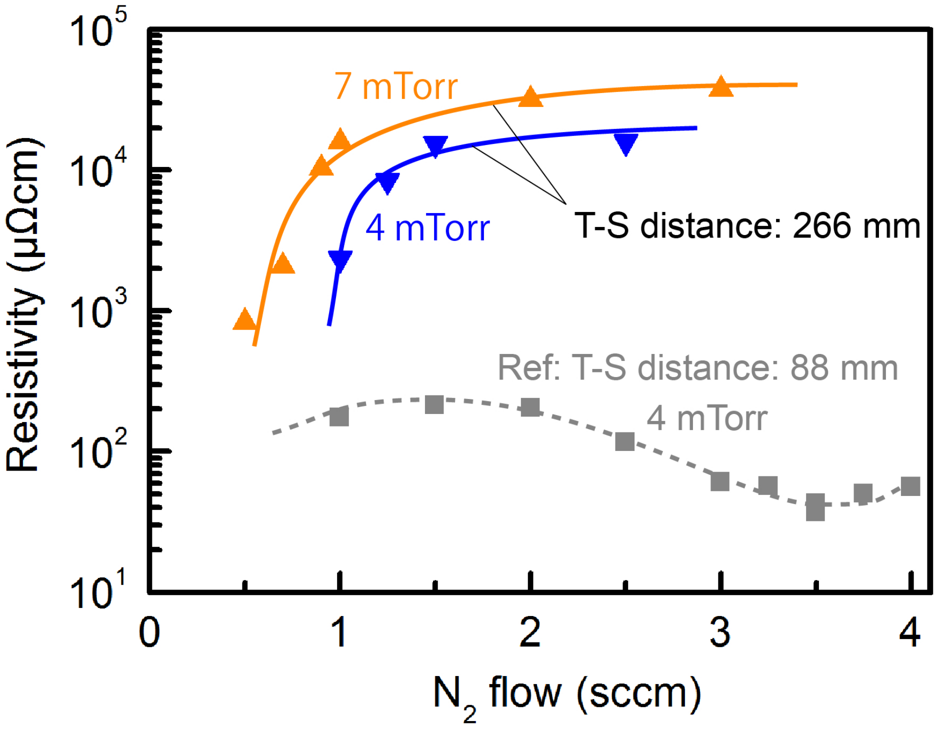

Figure 3.8: (Color online) The orange (triangle) and blue (inverse triangle) points are the resistivities of the TiN films as a function of the N_2 flow rate when the T-S distance is 266 mm and the deposition pressure is 7 and 4 mTorr, respectively. As a reference, we show data for films deposited at 4 mTorr with the T-S distance at 88 mm (gray rectangles), which is the same T-S distance used for all the depositions of the TiN films shown in sections 3.3 through 3.5. The solid and the broken curves are guides for eyes.

low sputtered-energy particles absorb a high amount of these contaminants, and the contaminant levels strongly depend on the sputtered particle energy. Therefore, the T-S distance is important for the production of high-quality TiN films.[56]

3.7 Properties of the scpw resonators

The application of superconducting films to circuits that detect photons and process quantum information motivates our investigation of the relationships between deposition conditions and the properties of the obtained material. Coupling this knowledge with an understanding of the impact that these materials properties have on device performance enables the realization of thin films optimized for quantum circuits. Whereas in the previous sections we discussed the response of TiN thin films to the reactive sputtering parameters used in their production, here we inspect the influence of specific TiN film features on the performance characteristics of devices into which the films are made. In order to evaluate these effects, we have deposited a series of nearly stoichiometric thin films at several pressures (2,4,5, and 7 mTorr) using the procedure outlined in the preceding sections with a T-S distance of 88 mm. Next, we patterned these films into SCPW microwave resonators and compared the performance of these devices to the material properties of either an unprocessed section of the same sample or of a companion wafer deposited under nominally identical conditions. The resonators in our experiment take the form of a quarter wavelength segment of coplanar waveguide terminated at opposite ends by an electrical open circuit and short circuit to the ground plane.

Among the virtues of the SCPW resonator is the simplicity of its fabrication. The SCPW resonator thus provides a context for our study of material vs device performance that is protected against the conflation of fundamental material data and complications arising from involved cleanroom proceedings. In this experiment, the substrate preparation and deposition described previously were followed by a single optical lithography and etching sequence. The nominally 100 nm TiN films were etched in an inductively-coupled plasma etcher with Cl_2 as the reactive species, under conditions yielding an etch rate of approximately 5.5 nm/sec. This primary etch was followed with a secondary, 5 sec SF_6 etch, as this has been shown to reduce loss [57]. This reliably produced a SCPW structure with a silicon substrate trench depth of 56 ± 11 nm. Once etched, the wafers were diced to yield chips measuring 6.25 x 6.25 mm square. Dies drawn from the center regions of our wafers were packaged in an Al sample box with an approximate linear wirebond density of 3/mm from the box to the device ground plane, in preparation for measurement.

During measurement, the sample box was mounted on the cold plate of an adiabatic demagnetization refrigerator with a base temperature of $\sim$ 70mK. This cold plate is shielded in stages from infrared radiation and external magnetic fields.[58]The output of the test chip was connected to a high-electron-mobility transistor amplifier at 4K, followed by a room temperature amplifier chain. A vector network analyzer (Agilent 5230A or 5242A) was used for excitation and detection. We characterized the SCPW by measuring the transmission scattering parameter S_{21} of a microwave transmission line capacitively coupled to a resonator. Details of the measurement and analysis are supplied by Megrant *et al.* [20]

Because energy relaxation events form an important error class in quantum information processing, this study focused on maximizing the low power Q_i, which is generally agreed to be limited by coupling to TLSs in the low energy excitation regime that is relevant to quantum computing and accessed in the limit where the number of photons in the resonator is small. Figure 3.9 (a) reports the dependence of Q_i on the microwave drive power for devices made from the nearly stoichiometric films deposited at 2,4,5, and 7 mTorr with N_2 flow rates of 3.5, 3.5, 3.5, and 2.5 sccm, which had compressive film strain values of 3800, 800, 1500, and 150 MPa, respectively. The 5mTorr sample was deposited under slightly nitrogen-rich conditions and we believe that this explains the nonmonotonicity of film strain vs deposition pressure for these samples. Figure 3.9 (b) shows the measured quality factors, at resonator excitation energies approximately equal to that of a single photon at the resonance frequency, versus the strain of the film from which they were produced. For Fig. 9 (a) and (b) we have selected the best performing device from each sample to establish an upper bound on device performance for a given set of material parameters, independent of such systematic issues as cleanroom process variability and time dependent external magnetic fields. We note that Q_i is enhanced as the film strain decreases and the oxygen content increases. In particular, the lowest strain film produced a resonator with a measured low power $Q_i = 3.8 \times 10^6$, the highest reported value to date; however, a subsequent reproduction attempt with a nominally identical film was unsuccessful. Aside from that, we find that a respectable low power $Q_i > 1 \times 10^6$ can be reliably achieved with low strain TiN SCPW resonators.

Since surface oxides of superconducting electrodes and their substrates are supposed to harbor the TLS populations[59] responsible for limiting the low power quality factors of SCPWs, the result that increased oxygen concentration in our compound superconducting films is associated with an increase in quality factor was not expected. More surprising, perhaps, is the absolute magnitude of the oxygen concentration; in the best performing films the ratio of O to TiN was measured to be 8%. We interpret this result to suggest that the presence of oxygen is not, in and of itself, deleterious to the resonator quality factor. Rather, oxygen incorporation by the TiN crystal may be an innocuous byproduct of the low strain condition which we suspect is itself fundamentally responsible for the quality factor increase in our experiment.

Although significant oxygen impurity concentrations in our TiN films do not directly translate to increased loss in our microwave resonators, the presence of oxygen in the TiN crystal is not inconsequential. As seen in Fig. 5(f), the normal state resistivity of our films depends strongly on the oxygen content. From a SCPW resonator perspective, the salient consequence of increased resistance is a resonant frequency reduction via kinetic inductance augmentation. This is a large effect in TiN, where

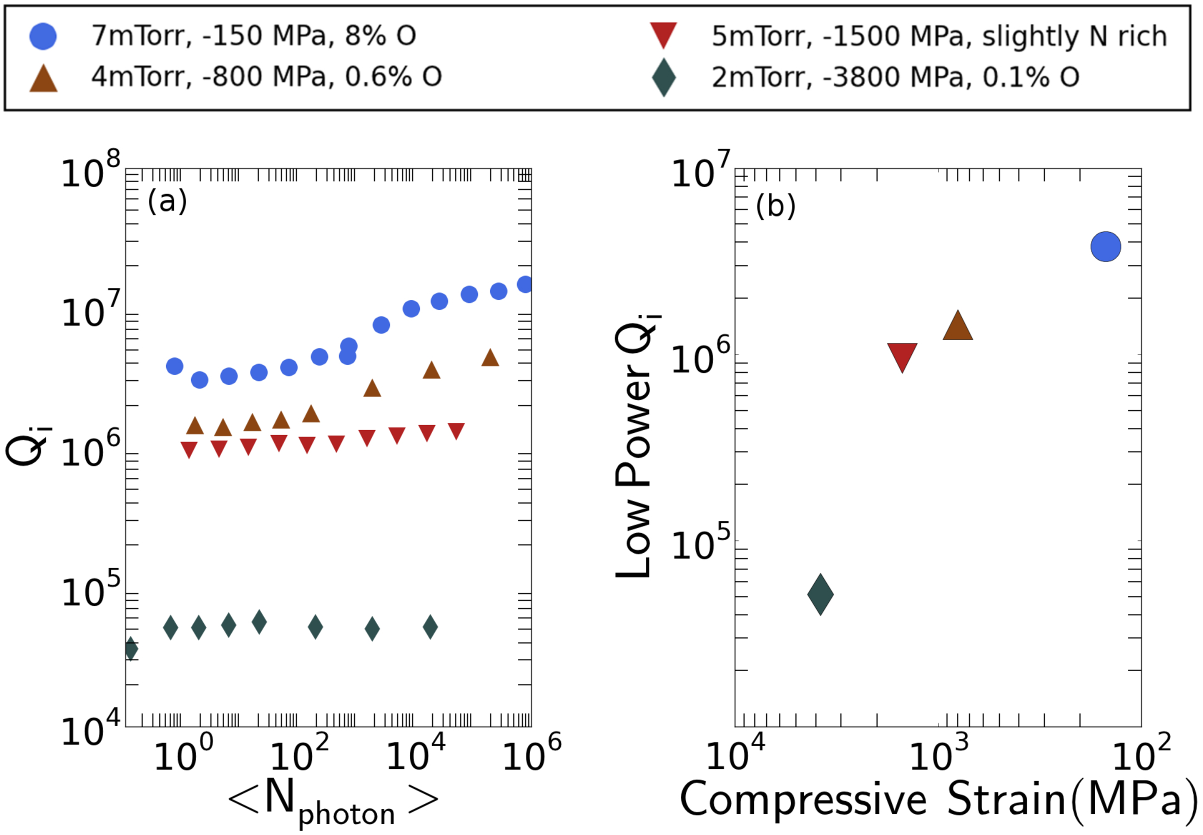

Figure 3.9: (Color online) (a) The power dependence of the SCPW resonator Q_i for the nearly stoichiometric films deposited at 2,4,5, and 7 mTorr and respective strain values -3800, -800, -1500, and -150 M Pa, expressed in terms of the expectation value of the resonator's photonic occupation number. (b) The strain dependence of the low power Q_i measured near $\langle N_{photon} \rangle = 1$.

the kinetic inductance is often larger than the geometric inductance for common device geometries. Applying these facts to the uniformity data in Fig. 3.6(b) presents an engineering dilemma to those who would make quantum integrated circuits from reactively sputtered TiN: in this material system, oxygen may not function as an instrument of excess loss, but the uncontrolled manner by which it installs itself in the crystal, and the corresponding lack of uniformity, renders engineering large-scale circuits on reactively sputtered TiN difficult at this time.

3.8 Summary

We have shown a detailed picture of the properties of TiN films deposited at room temperature by varying the deposition pressure and the N_2 flow rate. When fixing the deposition pressure, the resistivity minimum corresponds to the stoichiometric point (x=0.5). By increasing the deposition pressure, while keeping x=0.5, the resistivity rises and T_c decreases. The strong in-plane compressive stress changes to weak tensile stress as the deposition pressure increases. The dominant crystal orientation changes from (200) to (111). The grain boundaries become clearer, and the contamination levels, including H, C, and O, significantly increase. The grain boundaries play a crucial role in the absorption of the contaminants. This morphology change is thought to be induced by the energy change of the sputtered particles due to the change of the deposition pressure.

The in-plane particle energy distribution caused by the in-plane inhomogeneity of the plasma leads to a large radial resistivity change (70 %) across a TiN film deposited at 7 mTorr on a 3-inch wafer. From the center to the edge of this sample, the grain boundaries become clearer, which is very similar to the effect of deposition pressure increase. We have found that larger amounts of the contaminants H, C, and O exist at the edge of the wafer than at the center. By increasing the T-S distance from 88 mm to 266 mm, the film color was changed from gold to green, and we detected a higher amount of H, C, and O in the film deposited with the T-S distance at 266 mm than at 88 mm. The energy of the sputtered particles, which decreases with distance from the substrate center and with increasing the T-S distance, is also responsible for these phenomena.

Following the method developed in section III of this paper, we deposited nearly stoichiometric films at 2,4,5, and 7 mTorr and found that increasing the deposition pressure decreased the film strain and increased the oxygen content. These changes were associated with an increase in the Q_i factor of SCPW resonators made from these films. However, the film resistivity is a strong function of oxygen content and was found to vary considerably with distance from the center of the substrate. The variation in resistivity, which translates to a surface inductance variation in the superconductor, makes it difficult to design and produce large circuits without addressing this issue first. However, the resonator performance achieved with TiN implies that this material is immediately useful for smaller circuits and justifies efforts to engineer more uniform deposition methods for larger devices.

Chapter 4

Dielectric surface loss in superconducting resonators with flux-trapping holes[1]

Superconducting coplanar waveguide (SCPW) resonators are extensively used in astronomy[60, 61] and quantum information [62–64]. An important frontier in SCPW resonator development is increasing the intrinsic quality factor $Q_i = 1/\text{loss}$. This is an especially important proxy for qubit performance, since the resonator Q_i is strongly correlated with the qubit relaxation time T_1 because qubits and resonators are subject to many of the same dissipation mechanisms.[65–72] Quantum computers require low

---

[1] This chapter was published as: "Dielectric surface loss in superconducting resonators with flux-trapping holes", B. Chiaro, et al. SUST **29**, 10 (2016)

operating temperatures $\lesssim 100\,\mathrm{mK}$, single-photon excitation energies, low magnetic fields $\lesssim 5\mu\mathrm{T}$, and high coherence $Q_i \gtrsim 10^6$. In this quantum computing regime, dominant loss mechanisms are two-level state (TLS) defects in amorphous dielectrics located at surfaces and loss from trapped flux in magnetic vortices.

We examine the tradeoff between increased TLS loss and reduced magnetic vortex loss that occurs when the ground plane of SCPW resonators is patterned with an array of holes. Fractal resonators also reduce magnetic losses, but are typically optimized for use in high magnetic fields and have not demonstrated quality factors as high as coplanar designs in small field environments.[73] Although hole arrays have long been known to eliminate dissipation from trapped flux, [74–76] these structures have not been studied in the quantum computing regime for the possibility of increasing TLS loss. Our data shows that dielectric TLS loss from flux-trapping holes is an important physical limitation if designed incorrectly.

When a thin-film superconductor is cooled through its transition temperature T_c in a magnetic field B_{cool}, it is energetically favorable for magnetic flux to be trapped as vortices at some defect[77]. The typical spacing between vortices or an edge of the superconducting film to a vortex is $\left(\Phi_0/B_{\mathrm{cool}}\right)^{1/2}$. As the superconducting order parameter has to vanish[78], this normal core produces dissipation in response to currents flowing past the core[67]. With a hole in the film, vortices form without a normal core and produce no dissipation. We note that suitably positioned normal-core vortices may be beneficial as quasiparticle traps[68, 69]. For this application, hole arrays should be positioned properly to engineer the number and position of the normal-core vortices.

Because the holes have sharp edges and expose the substrate, they introduce new dissipation sites from surface TLS defects. As modern high-Q resonators are sensitive to nanometer thick amorphous dielectrics at surfaces[79], these additional edges can increase loss if the holes are placed near the resonator where the electric fields are the largest. Consequently, we must determine how closely holes can be safely placed from the resonator.

We characterize this loss with quarter-wavelength SCPW resonators that are capacitively coupled to a feedline, with frequency multiplexing to measure 10 resonators per chip. An optical image of a device wirebonded in a mount is shown in Fig. 4.1(a). The resonators have fundamental frequencies between 4.6 GHz and 5.5 GHz and center trace and gap dimensions of $15\,\mu$m and $10\,\mu$m. Our circuit contains both resonators with and without ground-plane holes for direct comparison. Our arrays are made from square holes of side length $2\,\mu$m and an edge to edge separation d of $2\,\mu$m, $6\,\mu$m, or $10\,\mu$m. The distance d is also the distance between the edge of the resonator gap and the nearest hole. An example is shown in Fig. 4.1(b). The equivalent circuit diagram for this device near resonance is shown in Fig. 4.1(c) and was analysed in detail in Ref. [80].

Our resonator circuits were fabricated from 100 nm aluminium thin films grown on c-plane sapphire substrates. The first type is made in a conventional electron beam deposition system with base pressure of 3×10^{-8} Torr. Films from this tool yield resonators with $Q_i \simeq 8 \times 10^5$ near a measurement photon number $N_{\mathrm{photon}} = 1$ and are thus representative of resonators made with standard deposition techniques. The second type was prepared in a molecular beam epitaxy (MBE) system with a base pressure of 1×10^{-11} Torr. With an in-situ O_2 plasma cleaning of the substrate at 650 °C [80], we found lower resonator loss $Q_i \simeq 1.5 \times 10^6$ for $N_{\mathrm{photon}} = 1$. The high quality factors make the MBE grown resonators sensitive probes of subtle decoherence mechanisms that may be induced by the holes. We report measurements from two circuits from each film for a total of four circuits. The resonators and holes were etched simultaneously in an inductively coupled plasma. The etch was performed at 0.7 Pa using BCl_3 and Cl_2 flow rates of 20 and 40 SCCM and 70 W bias power.

For measurement, individual devices were wirebonded in Al sample mounts and anchored to the cold stage of an adiabatic demagnetization refrigerator (ADR). A schematic of our apparatus is shown in Fig. 4.1(d). The 40 mK ADR base temperature is well below the transition temperature $T_c \simeq 1.1$ K of Al, so the thermal quasiparticle density is negligible. Additionally, our cryostat includes extensive infrared (IR) radiation shielding composed of in-line coaxial IR filters and a light-tight sample compartment that reduces the non-equilibrium quasiparticle population be-

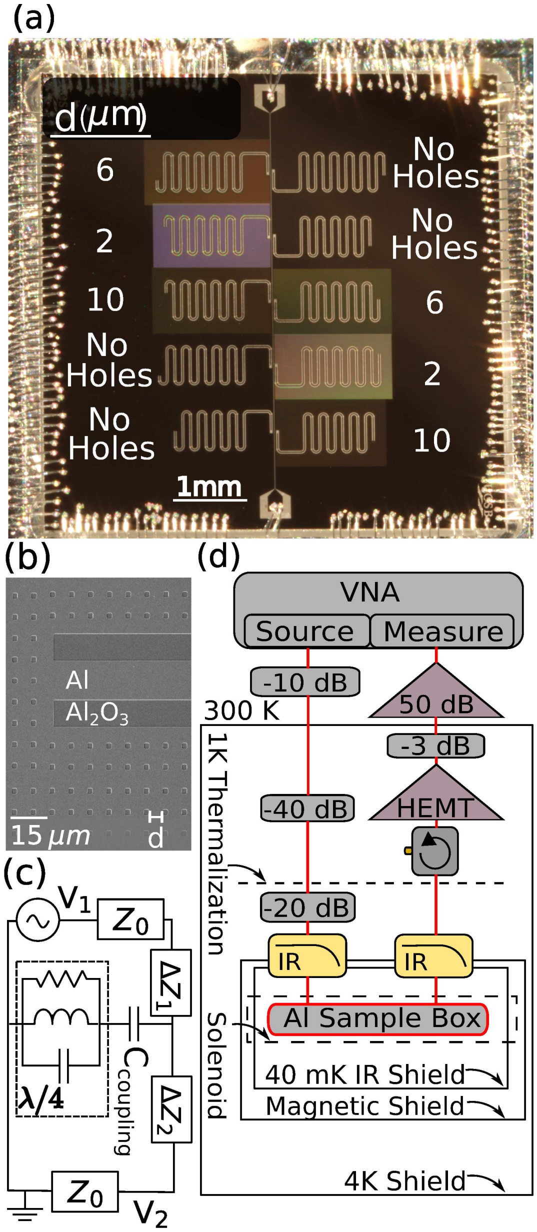

Figure 4.1: (color) Device and apparatus. (a) Optical micrograph of a chip wire-bonded inside sample mount, showing hole edge to edge separation d. (b) Scanning electron microscope (SEM) image showing a $\lambda/4$ resonator with a ground-plane hole array, displayed near the antinode of current. (c) The equivalent circuit for a $\lambda/4$ resonator capacitively near resonance[80], coupled to a transmission line. Included is the effect of small in-line impedance asymmetries characterized by ΔZ_1 and ΔZ_2. (d) Apparatus diagram and wiring schematic with signal path in red.

low our measurement sensitivity [81]. A circulator on the output line of the chip reduces noise from the input of the high electron mobility transistor (HEMT) amplifier. A solenoid encircles the sample compartment allowing us to apply a magnetic field perpendicular to the film, with 50 nT resolution to measure the magnetic field dependence of our resonator Q_i. We surround the mount with a magnetic shield and remove all magnetic components. We test each component that we use inside the sample compartment for magnetism and use non-magnetic SMA connectors (EZ Form Cable Corp. model #705626-301), cables (EZ Form Cable Corp. model #301844), brass screws, and custom experimental hardware. This reduces the ambient magnetic field at the device to $\lesssim 1.5\,\mu$T.

The loss is determined by measuring the resonator intrinsic quality factor Q_i using transmission spectroscopy[80]. In the initial measurement phase, we measure Q_i versus applied magnetic field at high power for better signal to noise ratio, since vortex loss has weak power dependence[75]. To vary B_{cool}, we raise the device temperature above T_c, set the applied magnetic field $\mathrm{B}^{\mathrm{cool}}_{\mathrm{applied}}$, and cool the sample back through its T_c in this field thereby trapping magnetic vortices. Once the device has returned to its base temperature we extract the resonator Q_i from S_{21} measurements with a vector network analyzer (VNA).

Figure 4.2 (a) shows the magnetic field dependence of Q_i for resonators with and without ground plane holes from the MBE device. For resonators without a pat-

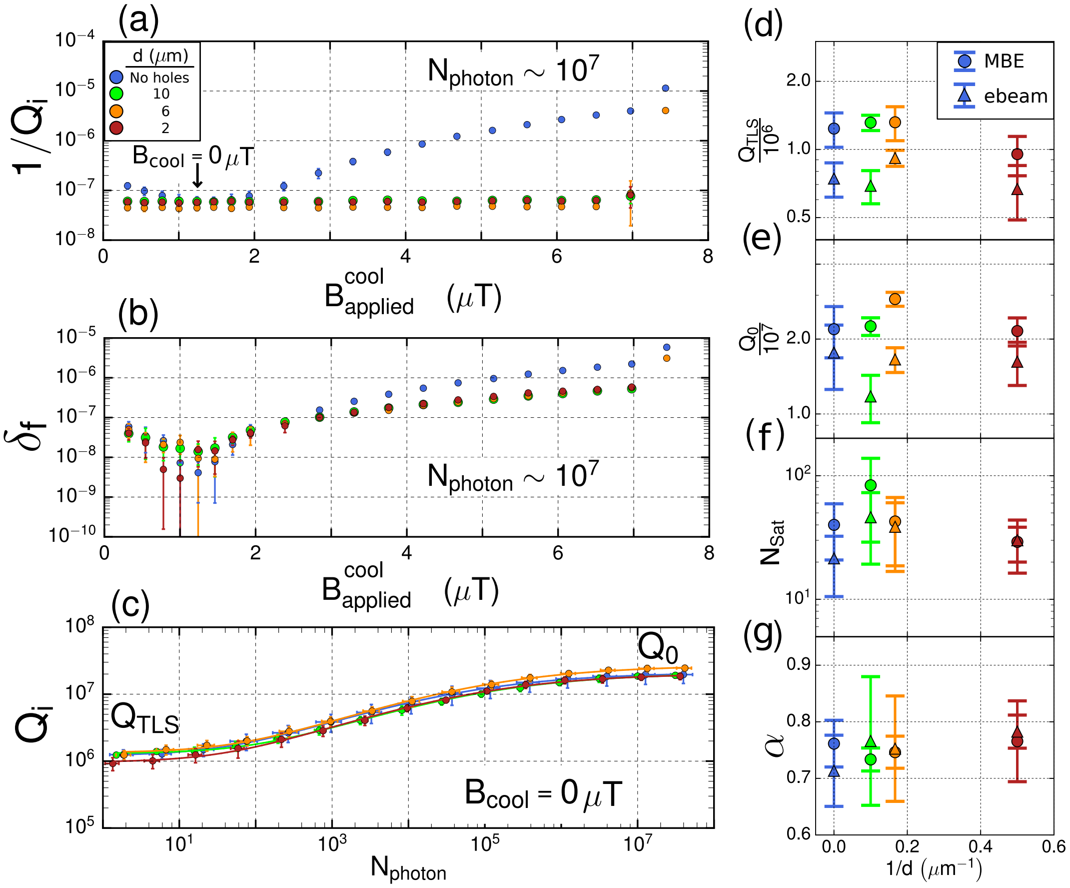

Figure 4.2: (Color) Measurement results (a) and (b) Loss $1/Q_i$ and resonator fractional frequency shift δ_{f} versus applied magnetic field when cooled through T_c $\mathrm{B}^{\mathrm{cool}}_{\mathrm{applied}}$, taken at high power $N_{\mathrm{photon}} \sim 10^7$. Data is for the MBE-grown film and hole patterns of varying density. The resonators with no holes have the greatest sensitivity to magnetic fields, so the minimum of loss identifies the true zero giving the cryostat offset field. (c) The dependence of Q_i on measurement drive power for the MBE sample, fit to a standard TLS dissipation model from Eqn. 4.1. (d) - (g) Extracted TLS model parameters from power dependence measurements as shown in (c) for the MBE and e-beam samples, showing loss attributed to unsaturated TLS (low power) and due to power independent mechanisms (high power) vs the edge to edge hole spacing d. In all plots the data shows mean value for resonators of a common hole density, with error bars indicating 1 standard deviation.

terned ground plane there is a well defined maximum of Q_i that identifies the applied field that zeros the total magnetic field.[82] The offset between $\mathrm{B}_{\mathrm{applied}}^{\mathrm{cool}}$ and B_{cool} is indicated by the arrow. We observe a gradual but significant increase in loss away from this field that is attributed to a greater density of magnetic vortices trapped in the ground plane. As expected, for resonators with holes we find that Q_i is nearly independent of applied magnetic field until the critical field for vortex formation in the center trace has been exceeded. Figure 4.2 (b) shows the fractional frequency shift $\delta_{\mathrm{f}} = (f_0(\mathrm{B}_{\mathrm{applied}}^{\mathrm{cool}} = 0) - f_0(\mathrm{B}_{\mathrm{applied}}^{\mathrm{cool}}))/f_0(\mathrm{B}_{\mathrm{applied}}^{\mathrm{cool}} = 0)$ we observe that resonators with patterned ground planes are less susceptible to field induced frequency shifts.

For MBE grown resonators with hole patterns we consider data in the field range of $\mathrm{B}_{\mathrm{applied}}^{\mathrm{cool}} = 1.4 - 6.4\,\mu\mathrm{T}$. Fields in this range are less than the critical field for vortex formation in the center trace of the resonator and allows us to estimate the residual magnetic loss in the absence of local magnetic vortices. By assuming an excess loss model that is linear in $\mathrm{B}_{\mathrm{applied}}^{\mathrm{cool}}$, we estimate the residual magnetic loss to be $8.6 \pm 1.3 \times 10^{-10}\,/\mu\mathrm{T}$. We show the data supporting this estimate in the supplement.[82] Although additional experiments are required to determine the origin and proper functional dependence of this excess loss, we suggest likely models are coupling to vortices in remote areas of the device not protected by the hole overlays or quasiparticles generated by the local suppression of T_c due to the magnetic field.

For typical shielded devices, this estimate is several orders of magnitude below the loss of the best SCPW resonators.[80, 83, 84]

After measuring the magnetic field dependence of the high power Q_i we quantify the surface loss from TLS defects by measuring the power dependence of the resonator Q_i. We use the value of $\mathrm{B}_{\mathrm{applied}}^{\mathrm{cool}}$ that maximizes Q_i at high power, so that $B_{\mathrm{cool}} = 0\,\mu\mathrm{T}$ as described previously. The power dependence data for the MBE device is shown in Fig. 4.2(c), where the lines are fits to a standard TLS loss model [85]

$$\frac{1}{Q_i} = \frac{1}{Q_{\mathrm{TLS}}} \frac{1}{\sqrt{1 + \left(\frac{N_{\mathrm{photon}}}{N_{\mathrm{sat}}}\right)^{\alpha}}} + \frac{1}{Q_0} \tag{4.1}$$

This model decomposes the total internal loss of the resonator $1/Q_i$ into a power independent loss term $1/Q_0$ that includes such loss modes from quasiparticles and radiation, and a power dependent term of magnitude $1/Q_{\mathrm{TLS}}$ that comes from TLS defects. Here N_{photon} is the excitation number of photons in the resonator and N_{sat} describes the saturation field of the TLS bath. The parameter α is related to the electric field distribution of the resonator, and may be influenced by interactions between TLS defects within the bath.[86, 87]

Figure 4.2(d) and (e) show the quality factors for the low power (Q_{TLS}) and high power (Q_0) regimes, extracted from the fits in (c). The data points represent resonators from two circuits from each film. In (d), we see that the densest hole pattern increases TLS loss by roughly 25% relative to resonators without holes for both the MBE and ebeam grown resonators. Dielectric TLS loss is often decomposed as $1/Q_{\mathrm{TLS}} = \mathit{\Sigma}_i \, p_i \tan \delta_i$ where $\tan \delta_i$ is the loss tangent of dielectric volume i and the participation ratio p_i is the fraction of the electric energy of the resonator excitation that is stored within that volume.[65, 72, 88] We presume that the increase in TLS loss is not due to an increase in the dielectric loss tangent, but rather due to an increase in the participation ratio resulting from a redistribution of the electric field.

To quantify the excess loss due to the dense hole pattern we perform linear regression analysis controlling for the difference between the MBE and ebeam films.[82] This analysis includes the results from 23 resonators, 11 measured on two circuits from the MBE film and 12 measured on two circuits from the ebeam film. We find that the TLS loss $1/Q_{\mathrm{TLS}}$ directly attributable to the dense hole pattern is $2.5 \pm 1.3 \times 10^{-7}$, where the uncertainty represents the standard error. The p-value for this regression coefficient is 0.07.

When using the resonators for quantum devices at low magnetic fields, this increase in loss is undesirable. The hole spacing should thus be carefully chosen, first to be close enough to provide protection from external fields of magnitude $\sim \mathit{\Phi}_0/d^2$, where d is the edge to edge spacing between holes[77]. However, the spacing from the resonator to the first row of holes should be greater than about $6\,\mu$m, a value that did not exhibit measurable excess TLS loss. In (e) we observe that the Q_0 of resonators with the densest hole pattern is nearly the same as that without any hole overlay. This indicates that power independent loss mechanisms were not affected by the hole patterns.

We have characterized dissipation from arrays of flux-trapping holes in SCPW resonators. We find that excess dielectric loss can be made vanishingly small by increasing the distance between the resonator edge and the array. In our experiment, a $6\,\mu$m separation was enough to remove excess dielectric loss; power-independent loss mechanisms were not affected by the arrays. We also estimate the residual magnetic loss in resonators with ground plane holes to be $\sim 10^{-9}\,/\mu\mathrm{T}$, showing that SCPW resonators can be made insensitive to small magnetic fields without magnifying other loss mechanisms.

Chapter 5

Growth and preservation of entanglement in a many-body localized system, [1]

In non-interacting systems disorder leads to Anderson localization, where particle diffusion and entanglement propagation are absent. Interactions between the constituent particles modify this picture, leading to a many-body localized (MBL) phase. A key challenge is to measure interaction induced dynamics of entanglement between the localized sites in this phase. By studying interacting photons in an array of superconducting qubits, we observe ergodicity breaking and directly measure the

---

[1] This chapter is currently under consideration for publication as: "Growth and preservation of entanglement in a many-body localized system", B. Chiaro, et al.

effective non-local interactions. We probe the entanglement signatures of MBL in 1D and 2D and observe the slow growth of entanglement entropy. Finally, we characterize the potential of the MBL phase to be used as a quantum memory by demonstrating the slow decay of entanglement of a distant bell pair. Our work elucidates the fundamental mechanisms of entanglement formation, propagation, and preservation in the MBL phase of matter.

5.1 Introduction

Disorder-induced localization is a ubiquitous phenomenon that occurs in both classical and quantum systems. In 1958 Anderson showed that in non-interacting systems disorder can change the structure of electronic wave-functions from being extended to exponentially localized [89]. This localized phase has been observed for systems of non-interacting phonons, photons, and matter-waves [90–94]. The conventional wisdom had long been that systems of interacting particles do not localize and ultimately reach thermal equilibrium regardless of the disorder magnitude. However, recent work suggests that localization may persist even with the introduction of interactions between particles, thus establishing the concept of many-body localization as a robust, non-ergodic phase of matter at finite temperature [95–97].

Various experimental studies show that some characteristics of the MBL phase resemble a conventional non-interacting Anderson phase in which relaxation is ab-

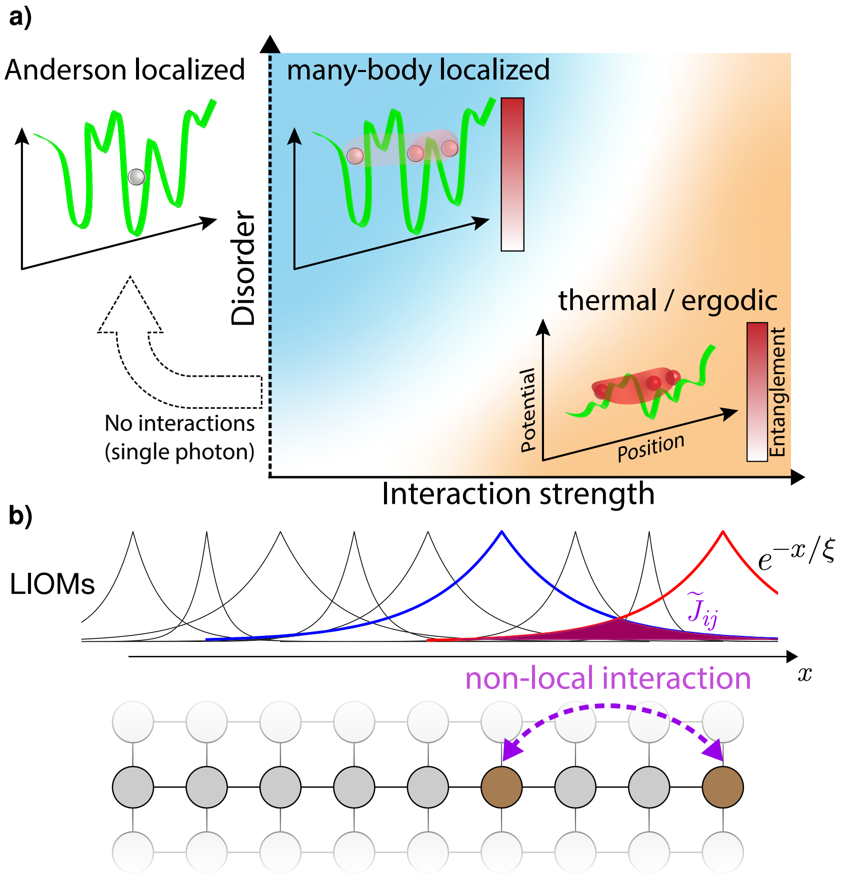

Figure 5.1: Many-body localization with superconducting qubits. (a) In 1D, Anderson localization occurs for arbitrarily weak disorder potentials. Interactions between the particles facilitate delocalization and entanglement propagation. When disorder is large, the MBL phase is realized and the particles remain localized but entanglement spreads. As the interactions are increased, the system transitions to a thermalized phase with fully delocalized and entangled particles. **(b)** The localized orbitals (local integrals of motion, LIOM) decay exponentially in space with a broad distribution of localization lengths ξ and couplings $\widetilde{J}_{ij}$ between them. The shaded region indicates effective non-local interactions between two LIOMs.

sent [98–104]; both Anderson localized and MBL phases do not thermalize. Theoretical studies suggest that the MBL phase has significantly different dynamical properties [97, 105–116]. In particular, resulting from the non-local interaction between particles it is anticipated that locally observed dephasing arises during the coherent closed-system dynamics (Fig. 5.1). It has been predicted that this dephasing leads to the slow growth of entanglement entropy in the MBL phase. The direct study of this physics is experimentally challenging as it is best accomplished with phase sensitive algorithms and measurement. Superconducting qubit systems allow a comprehensive study of interaction effects in the MBL phase, since they offer capabilities to perform versatile wave function initialization, Hamiltonian generation, and measurements in different bases.

Using an array of superconducting qubits, we realize a bosonic lattice and study the dynamics of photon excitations as a function of disorder. The Hamiltonian of the chain is described by the Bose-Hubbard model

$$H_{BH} = \underbrace{\sum_{i}^{n_Q} h_i a_i^\dagger a_i}_{\text{on-site detuning}} + \underbrace{\frac{U}{2}\sum_{i}^{n_Q} a_i^\dagger a_i (a_i^\dagger a_i - 1)}_{\text{Hubbard interaction}} + \underbrace{J \sum_{\langle i,j \rangle} \left(a_i^\dagger a_j + a_i a_j^\dagger \right)}_{\text{NN coupling / hopping}} \tag{5.1}$$

where $a^\dagger$ (a) denotes the bosonic creation (annihilation) operator, $h_i \in [-w, w]$ is the random on-site detuning drawn from a uniform distribution of width $2w$, J is the hopping rate between nearest neighbour lattice sites, U is the on-site Hubbard interaction, and n_Q is the number of qubits [117]. The qubit frequency, the nearest neighbor coupling, and nonlinearity set h_i, J, and U, respectively. We are able to tune the h_i and J independently at a fixed nonlinearity $U = 160$ MHz.

The localized regime of Eqn. (1) is obtained when the frequency detunings h_i are large compared to J. In this regime, the eigenstates of the Hamiltonian are product states of localized orbitals, referred to as local integrals of motion (LIOM), which are nearly qubit states but have a spatial extent that decays exponentially across the neighboring qubits (Fig. 5.1(b)). In the localized regime, Eqn. (1) can be brought into a diagonal form by a set of local unitary transformations [108, 109]. In this basis there is no hopping and the Hamiltonian can be written in terms of on-site detunings and non-local interactions,

$$\tilde{H}_\tau = \underbrace{\sum_i \widetilde{h}_i \tau_i^z}_{\text{on-site detuning}} + \underbrace{\sum_{i,j} \widetilde{J}_{ij} \tau_i^z \tau_j^z + \sum_{ijk} \widetilde{J}_{ijk} \tau_i^z \tau_j^z \tau_k^z + \ldots}_{\text{non-local interaction}} . \tag{5.2}$$

The τ_j^z operators commute with $\tilde{H}_\tau$ and are hence conserved; the system is localized. However, the non-local interactions $\widetilde{J}$, which follow a broad log-normal distribution, generate entanglement throughout the localized system [118].

5.2 Breakdown of ergodicity

Evidence for the breakdown of ergodic dynamics can be obtained by measuring the mobility of excitations in a 1x9 qubit array. In Fig. 5.2, we initialize the system with a number of photon excitations n_{ph} by preparing 1, 2, or 3 qubits in the single

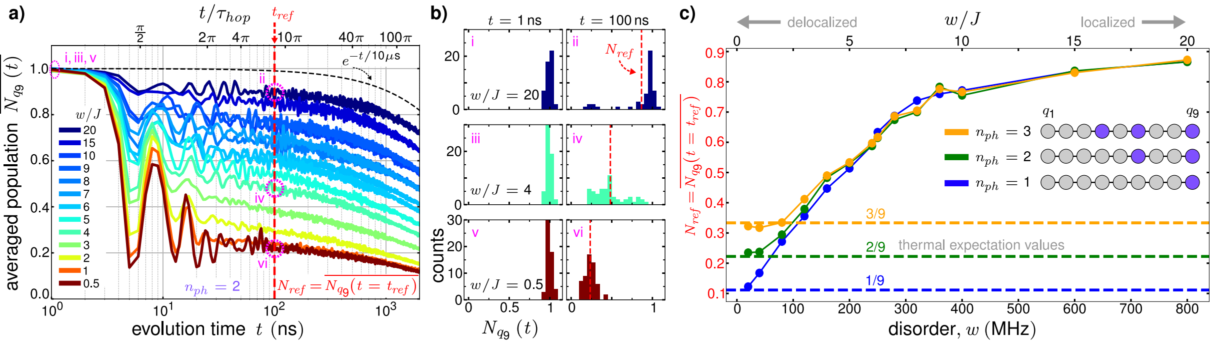

Figure 5.2: Ergodicity breakdown. **(a)** Disorder averaged on-site population vs. time for $n_{ph} = 2$. In a chain of 9 qubits, two qubits were excited ('q6', 'q9'). The on-site population of 'q9' was measured with resolution of $|0\rangle$, $|1\rangle$, $|2\rangle$ for various magnitudes of disorder w/J, with $J = 40\,\text{MHz}$. The overline indicates average over disorder realizations, and each data point is the average of 50 realizations. The parameter $\tau_{hop} = (2\pi J)^{-1}$ has been introduced to connect the laboratory time t with the hopping energy. N_{ref} is defined to be the average on-site population across instances of disorder at the reference time $t_{ref} = 100\,\text{ns}$, after initial transients have been damped. The dashed black line indicates expected photon loss for a single qubit measured in isolation. **(b)** Histograms of $N_{q9}\ (t)$ at the times and disorders indicated in **(a)** by numerals i - vi. **(c)** N_{ref} vs. disorder for $n_{ph} = 1, 2, 3$. Inset shows which qubits were excited at $t = 0$ ns.

excitation Fock state. We measure the population on one of the initially excited qubits as the system evolves under Hamiltonian (1).

The disorder averaged population at q_9 (the observation site) $\overline{N_{q9}\ (t)}$ for $n_{ph} = 2$ is shown in panel (a). We choose a reference time t_{ref}, in which $\overline{N_{q9}\ (t)}$ approaches an asymptotic value after initial transients have been damped, before the dynamics of our system are dominated by relaxation to the environment at large time scales (dashed black line), or delocalization within our closed system driven by extrinsic dephasing [117, 119–123]. The distribution of $N_{q9}\ (t)$ for selected disorder magnitudes at $t = 1\,\text{ns}$ and $t = t_{ref}$ are shown in panel (b). At $t = 1\,\text{ns}$ the excitations have not propagated, and there is a tight distribution close to the initial values, regardless of the value of disorder. At $t = t_{ref}$ the distribution is narrow for low disorder and becomes wider with tails at larger disorders. This can be understood because at high disorder, level resonances are increasingly rare which inhibits mobility. The tail of the distribution results from these rare cases. At low disorder, excitations can propagate freely between qubits and the behavior of each disorder instance is typical, giving rise to narrow distributions.

Fig. 5.2(c) shows the disorder averaged population after $t_{ref} = 100\,\mathrm{ns}$ of evolution as a function of the disorder strength. At low disorder, in the diffusive regime, we expect the dynamics to satisfy the ergodic hypothesis that each of the two photon states is equally likely to be observed. Here, a uniform averaging over the available phase space implies that the expected occupancy of a given qubit should be n_{ph}/n_Q. For multiple photon excitations our observations are consistent with ergodic dynamics at weak disorder; however, as we increase the disorder strength, significant deviations from the thermal value are observed, which indicates that our system becomes many-body localized. We note that with more photons in the system, the population converges to its thermal expectation value at higher disorders. This is expected because the increased interactions assist with the thermalization process and drive delocalization. In the case of a single excitation our system is non-interacting and hence localized for all disorder magnitudes. The apparent approach of the population to the thermal value at extremely weak disorder indicates the regime where the single-particle localization length exceeds our system size. The ergodicity breaking shown here is general and the results for the 2D system can be found in the supplement [117].

5.3 Interferometric methods

Nonlocal interactions between the LIOMs can be unambiguously established by adopting interferometric methods inspired by NMR protocols [110]. Fig. 5.3(a) illustrates a conventional spin-echo (SE) sequence and its extension double electron-electron resonance echo (DEER) which we use to provide a differential measurement of phase accumulation with and without a remote perturbation. The construction and effects of these pulse sequences can be understood from Eqn. (2). Deep in the MBL phase, the LIOMs are nearly localized on individual qubits. The SE π-pulse between free precession intervals essentially negates the local frequency detuning, reversing the evolution and hence phase accumulation. The role of the additional $\pi/2$-pulse in the DEER sequence is to make the SE refocusing incomplete, directly probing the strength of the non-local interaction. The measurement of on-site population, depicted in panel (b), shows that the remote $\pi/2$-pulse in the DEER sequence does not appreciably alter the population on the observation site, assuring that the system is in the localized regime. Therefore, comparing SE and DEER, the contrast observed in the single qubit purity (panel (c)), is a pure interference effect that directly measures the non-local interaction between distant localized sites. In addition, the difference between SE and DEER decreases as the distance between the SE site and remote disturbance site is increased. This can be understood from the decaying nature of the interactions between the LIOMs with distance. The interferometric protocol is thus demonstrating the foundational interaction effects of MBL states.

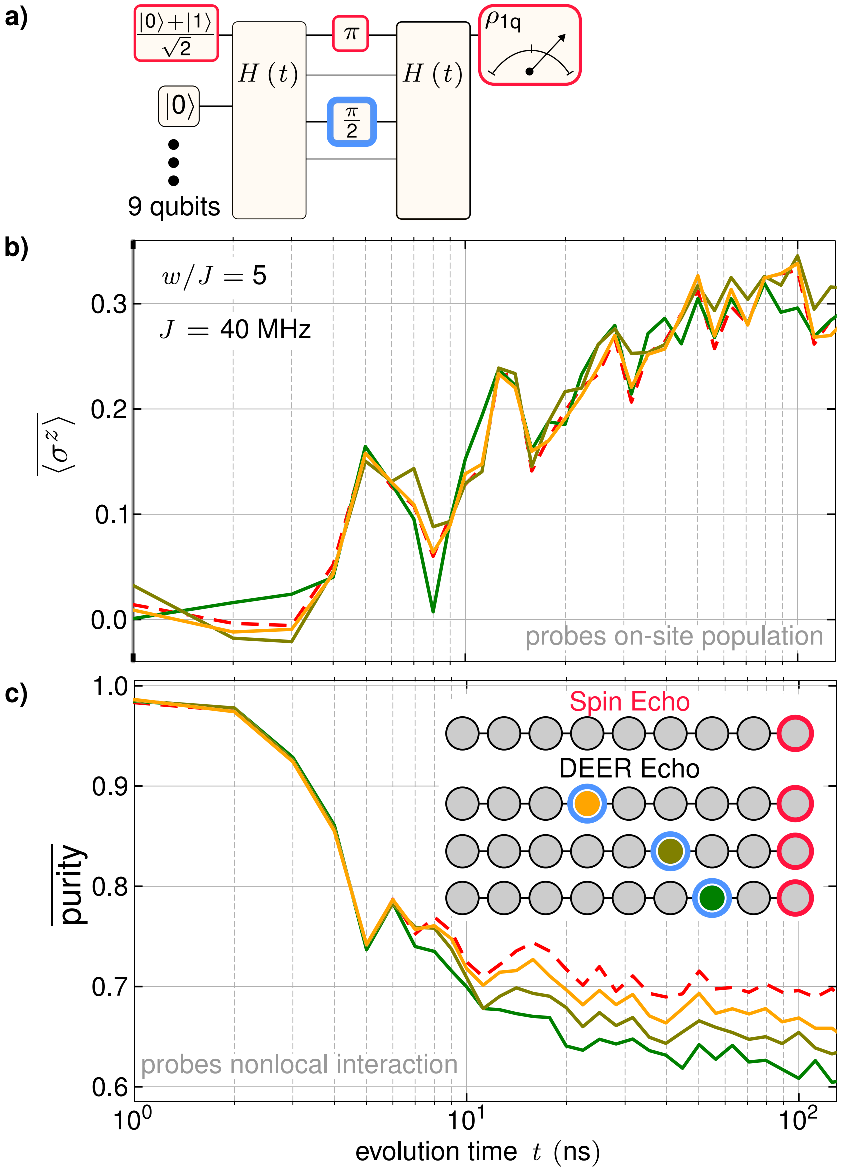

Figure 5.3: Interferometric signatures of remote entanglement. **(a)** SE and DEER pulse sequences. DEER differs from SE by the addition of a remote $\pi/2$-pulse simultaneous with the SE π-pulse between the free precession intervals. **(b)** $\overline{\langle \sigma^z \rangle} = \overline{\left\langle 1-2a^\dagger a \right\rangle}$, and **(c)** purity of the single qubit for SE (red dashed) and DEER (solid) experiments. The remote DEER pulse induces dephasing, decreasing the purity. The contrast between SE and DEER probes the non-local interaction $\widetilde{J}_{ij}$ between the SE lattice site and the DEER site.

5.4 Entanglement entropy

A hallmark of the MBL phase is the slow growth of entanglement, contrasting with Anderson localization where the entanglement is constant. To study the development of entanglement entropy, we designate two qubits as a subsystem and the rest of the chain as the environment (Fig. 5.4(a)), and directly measure the evolution of the reduced density matrix of the subsystem. The subsystem qubits are initialized into superposition states. Fig. 5.4(b) shows that $\overline{\langle\sigma^z\rangle}$ initially rises because population from the subsystem qubits is transferred to the environment which has a smaller photon density. After this initial rise, $\overline{\langle\sigma^z\rangle}$ takes a stationary value which decreases with decreasing coupling strength, establishing the localization of our system.

We use the von Neumann entanglement entropy

$$S_{\mathrm{vN}} = -\mathrm{Tr}\rho_{2\mathrm{q}}\log\rho_{2\mathrm{q}} \tag{5.3}$$

to quantify the entanglement between the subsystem and the environment (panel (c)). The initial increase in $\overline{S_{\mathrm{vN}}}$ occurring simultaneously with the increase in $\overline{\langle\sigma^z\rangle}$ is understood as the result of the subsystem exchanging population with the environment. Thereafter, while the system is demonstrably localized, we observe logarithmic growth of von Neumann entropy. We can understand the slow growth in terms of the LIOM framework: The non-local and exponentially decaying interactions between the LIOMs give rise to dephasing between the qubits and follow a broad log-normal distribution [118]. As a consequence, the entanglement of individual runs is strongly fluctuating on different time scales leading to a logarithmic growth of the entanglement of the subsystem. We note that preparing subsystem qubits in an x-polarized state is key for the success of this measurement as it enhances the measurement visibility by being highly phase sensitive. The von Neumann entropy quantifies entanglement with all external degrees of freedom and is not able to disambiguate entanglement with the environmental qubits due to unitary dynamics from open systems effects. As such, our observed entropy is an upper bound on the entanglement generated within our qubit array. The $J = 0$ curve (black) provides an estimate of the amount of entropy that is due to open system effects. Next, we introduce entanglement measures that are more robust against open systems effects and lower bound the entanglement between parts of the system.

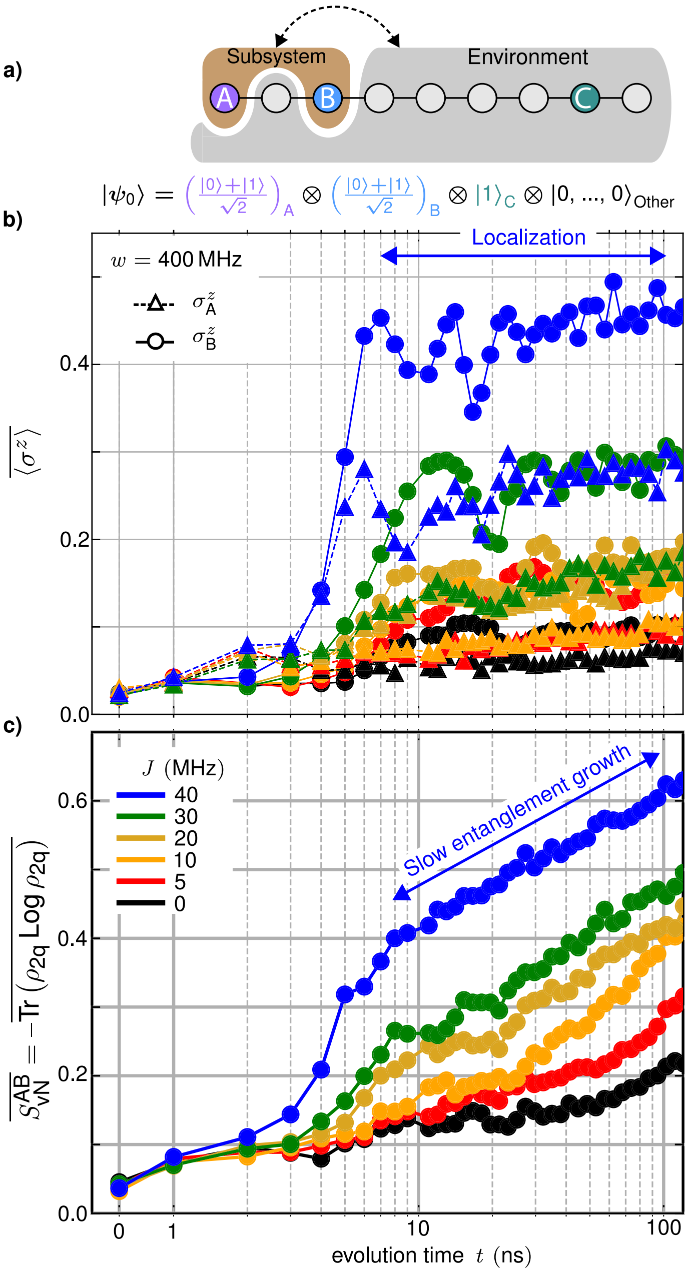

Figure 5.4: Localization and slow growth of entanglement (a) Partitioning of our 9-qubit chain into a subsystem and environment. The subsystem qubits (A and B) are initialized into superposition states, and the system is loaded with an additional excitation (site C) to enhance many-body interactions. We tomographically reconstruct the density matrix of the subsystem. **(b)** $\overline{\langle\sigma^z\rangle}$ for subsystem qubits. **(c)** von Neumann entanglement entropy of the two qubit subsystem for several coupling strengths.

5.5 Growth and preservation of entanglement

We investigate the formation and preservation of entanglement between two qubits A and B that are embedded in a MBL environment as illustrated in Fig. 5.5(a). The entanglement of formation (EOF) quantifies the amount of entanglement directly between qubits A and B that would be required to produce the observed two-qubit mixed state density matrix [124]. This entanglement can be viewed as the elemental building block of the S_{vN} in Fig. 5.4. We emphasize that because we are affirmatively detecting a quantum correlation between sites of the subsystem, the observed EOF cannot be attributed to open system effects which would tend to suppress the correlation. The EOF is therefore a more conservative entanglement measure than S_{vN} and a valuable tool for characterizing realistic experimental systems, which are semi-open.

In (a) to (c), we initialize the subsystem in a product state of single qubit superpositions and observe the development of entanglement between the subsystem qubits. Regardless of geometry of the qubit array, entanglement grows gradually between the localized, spatially separated sites over several hopping times. Intuitively, the entanglement grows faster and achieves a higher maximum value when the subsystem qubits are closer to each other. This can be understood by considering two isolated qubits, which exhibit a cosine shaped growth and collapse of their mutual entanglement at a frequency that is set by the effective interactions $\widetilde{J}_{ij}$, explaining the shift of the first maximum toward much larger times as the distance is increased. Due to the presence of the other qubits in our system, the entanglement deviates from the cosine shape after the first maximum [107]. At long times open systems effects become important. The EOF results are in contrast to the von Neumann entropy, which continuously increases because it includes entanglement with all degrees of freedom external to the subsystem.

As the system geometry is transformed from 1D into a ladder and finally 2D (panels (a) to (c)) there is an overall trend of suppressed EOF. This can be understood by considering the mobility in combination with the monogamy of entanglement principle [125]. Compared with 1D, in 2D each qubit has additional neighbors, which changes the structure of the LIOMs and provides more transport channels, enhancing the spread of entanglement. The monogamic principle states that there is a maximum degree to which two qubits may be correlated, and that entangling (correlating) either member of this pair with other qubits necessarily decorrelates the first two. Thus in the higher dimensional systems shown here the subsystem qubits entangle with the environmental qubits to a greater extent thereby reducing the degree to which the subsystem qubits can be correlated.

At long times, the interaction between subsystem qubits is out competed by the interaction of the subsystem with the environmental qubits and the open system and the EOF declines. We highlight the capability of EOF, an affirmative correlation measure, to detect correlation between sites with large separation, e.g. (A, B_3) despite being embedded in a large entangled array with open system effects.

The results thus far illustrate how interaction effects propagate entanglement throughout the system. However, because MBL systems are non-thermal and localized, features of their initial state remain imprinted on them. This ability of MBL systems to retain quantum correlations as a computational resource for later retrieval suggests their potential as a quantum memory [108, 126, 127]. To probe this aspect, we prepare a maximally entangeled Bell state between two subsystem qubits in a 3×7 qubit array and monitor the subsystem density matrix as the pair is dephased by a remote photon. We focus on the distillable entanglement (DE), i.e. the entanglement which can be extracted from the mixed density matrix. The upper and lower bounds of the DE are the logarithmic negativity entropy and the coherent information entropy respectively, shown in Fig. 5.5 (d) and (e).

The initial drop of DE, on the single hopping timescale, is attributed to population transfer from the Bell pair into the environmental qubits. Thereafter, interaction with the remote photon induces local dephasing in the subsystem, decorrelating the subsystem qubits according to the monogamy of entanglement principle. With the remote photon at larger distances, the DE remains finite over several hopping times. The entanglement is increasingly disturbed as the remote photon is brought closer to the Bell pair and the coherent information that lower bounds the DE approaches zero at earlier times. This data illustrates the potential of the MBL phase as a quantum memory and highlights excitation density as a critical parameter for this application.

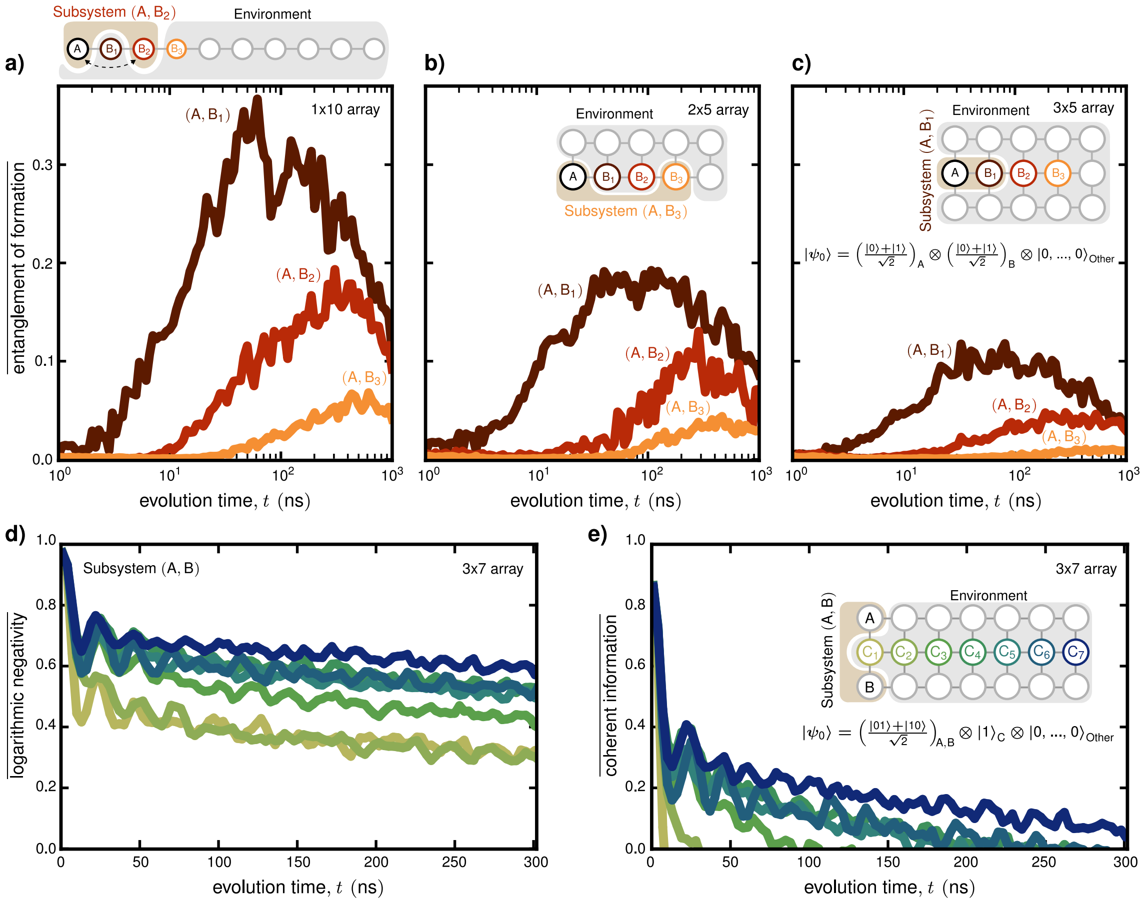

Figure 5.5: Growth and preservation of entanglement between localized sites Entanglement of formation between qubits in various 2-qubit subsystems (A,B$_i$). To observe the development of entanglement between sites A and B the subsystem is initialized in a product of single qubit superposition states and the entanglement of formation of the two qubit density matrix is extracted, for subsystems of **(a)** 1×10, **(b)** 2×5, and **(c)** 3×5 array of qubits with $J = 30\,\mathrm{MHz}$ and $w/J = 10$. In a 2 qubit subsystem (A,B) of a 3 by 7 array of qubits, a Bell pair is created, and the Logarithmic negativity **(d)** and coherent information **(e)** are extracted from measurements of the subsystem density matrix and averaged over 80 realizations of disorder for $J = 30\,\mathrm{MHz}$ with $w/J = 12$. We initialize the environment with an excitation at a position C_i which is varied

Chapter 6

Conclusion and Outlook

Over the past twenty years superconducting qubits have made remarkable progress in the engineering and control of single and few qubit systems. This progress has been facilitated, in no small part, by leveraging concepts originally developed in the atomic physics community. Modern supremacy era quantum processors, are large scale systems of many interacting "atoms" and describing the collective behavior of such an object is the domain of condensed matter physics. A fundamental motivation of this thesis is the suggestion that the quantum computing community will benefit from adopting the mindset, insights, and techniques of condensed matter physics. This thesis represents a conceptual step in that direction with implications in the areas of algorithm development and system level metrology.

In this work we have demonstrated the use of a large scale quantum processor as a programmable quantum simulator and used it to provide a comprehensive survey of the many-body localized phase. The fact that part of this work was performed on the device that was used in the demonstration of quantum supremacy[6] indicates that in the near future we will be using quantum hardware to address open questions in condensed matter physics and quantum dynamics more generally. As such, our work indicates analog quantum simulation as a viable pathway for near-term quantum processors to demonstrate a quantum computational advantage on meaningful questions of scientific interest even before quantum error correction has been achieved.

Considering large scale quantum processors as condensed matter systems is also valuable for system level metrology development. It is equally true for digital, gate-based quantum processors and analog quantum simulators that the underlying dynamics are fundamentally analog. An obvious consequence of this is that the error mechanisms and "dirt physics" of the device can only be understood by considering the underlying analog nature of the device. Consider the fixed coupling Xmon transmon style designs. In this style of device, the interactions between qubits are turned off by large frequency detunings between qubits with fixed couplings. One concern for such an architecture is the parasitic ZZ interaction that results from the "always on" coupling. This parasitic entanglement growth within a disordered interacting lattice results from the same basic physics as the entanglement dynamics of many-body localized phase discussed in chapter 5. Thus tools developed in the condensed matter physics community for the study of many-body localization can be easily translated provide us with system level metrology techniques. Explicitly, the echo protocols of chapter 5 were designed to capture the non-local MBL interactions $\widetilde{J}_{ij}$, but can equivalently characterize the parasitic interactions of a fixed coupling Xmon chain.

The analog quantum simulation work in this thesis has also inspired new technical directions. For example, one shortcoming of our approach to analog control is that we do not presently have the ability to recover the coefficients of the Hamiltonian that was actually applied in our experiments. Our ability to benchmark the control fidelity is limited to a comparison of the eigenvalues predicted by a circuit model with the eigenvalues extracted by many-body Ramsey spectroscopy. The primary issue with this is that when there is a disagreement between the predicted and measured eigenvalues we are not presently which parameter(s) were the source of the error. We have a time domain method for this "Hamiltonian recovery" under development, but at the time of this thesis it remains a future direction. Once complete, this will enhance our ability to capture errors in our assumed device Hamiltonian model, as well as compensate for departures from the desired Hamiltonian during analog simulations.

Another avenue of ongoing research sparked by the investigations in this thesis is the use entanglement measures, especially the entanglement of formation and distillable entanglement, as a means of experimentally determining (or at least bounding) the complexity of algorithms being run on the quantum computer. It has been suggested that development of entanglement based complexity metrics are expected to provide valuable information in the search for algorithms with a quantum advantage.[128]

Appendix A

Supplementary information for "Dielectric surface loss in superconducting resonators with flux-trapping holes"

We show the data and analysis estimating residual magnetic loss in superconducting resonators with flux-trapping hole arrays. We describe the design rules used to embed a meandered resonator in a rectangular array of holes. We show data supporting the claim that the maximum in Q_i is obtained at an applied magnetic field that cancels the ambient field. We report the TLS model parameters for resonators from the MBE and ebeam deposited films from which we estimate the excess loss attributable directly to the densest hole pattern.

A.1 quality factor extraction

In the main text, we infer resonator loss $1/Q_i$ by measuring the system scattering parameters (S-parameters) of superconducting coplanar waveguide (SCPW) resonators capacitively coupled to a feedline. The circuit model for this system has been analysed previously [80] and gives the result

$$\tilde{S}_{21}^{-1} = 1 + \frac{Q_i}{Q_c^*} e^{i\phi} \frac{1}{1 + i2Q_i \frac{f-f_0}{f_0}} \tag{A.1}$$

Here $\tilde{S}_{21}^{-1}$ is the inverse of transmission data calibrated to enforce $S_{21} = 1$ far off resonance. f_0 and ϕ are the resonant frequency and impedance mismatch angle and Q_c^* is the coupling quality factor scaled by an impedance ratio.

We extract the internal quality factor Q_i and its statistical uncertainty σ_{Q_i} by fitting measurements of our device to this model. Figure A.1 shows example data from the MBE sample for which the $Q_i = 1.86 \times 10^7 \pm 2.58 \times 10^5$. This is representative of the data points shown in Fig A.2.

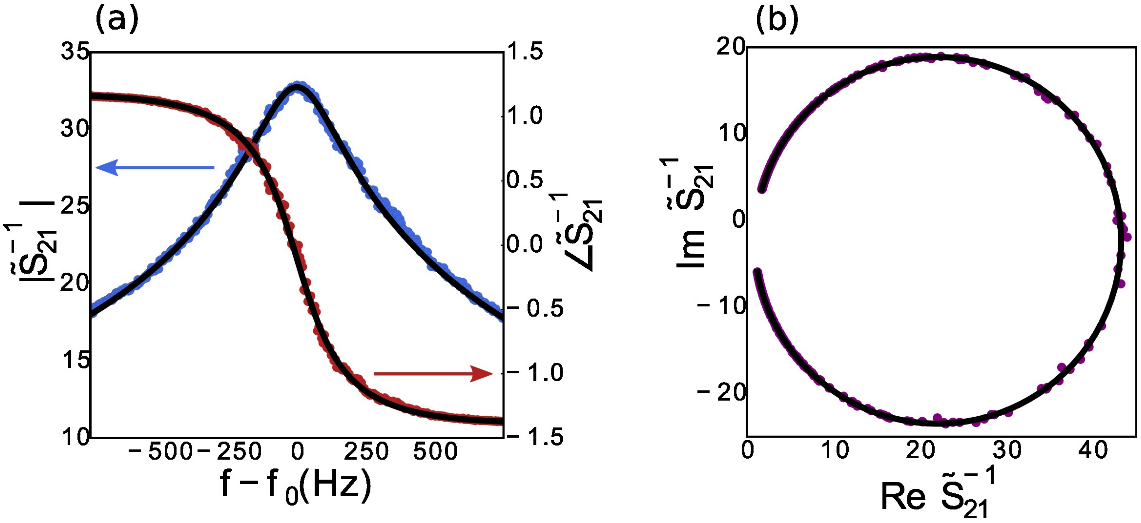

Figure A.1: (Color online) The transmission spectroscopy data for the extraction of Q_i shown as (a) magnitude and phase and (b) in the complex plane.

A.2 Residual magnetic loss

Fig. A.2 breaks out the data in Fig. 2a of the main text for resonators with ground plane holes from the MBE sample in the region from $\mathrm{B}^{\mathrm{cool}}_{\mathrm{applied}} = 1.4\,\mu T$ to $6.4\,\mu T$. This is below the critical field for vortex formation in both the center trace of the resonator and in the ground plane near the resonator where there are ground plane holes. Thus, we do not expect magnetic loss in this region. In Fig. A.2 we apply a linear loss model $1/Q_i = m \times \mathrm{B}^{\mathrm{cool}}_{\mathrm{applied}} + b$ to the data and obtain the parameters m and b with a weighted least squares fit. We use weighting factors $1/\sigma^2_{(1/Q_i)}$, where $\sigma_{(1/Q_i)} = \left(-1/Q_i^2\right)\sigma_{Q_i}$ in terms of parameters extracted directly from device data. We obtain our estimate of residual magnetic loss from the parameter m in these fits. This estimate is $m = 8.6 \times 10^{-10} \pm 1.3 \times 10^{-10}\ /\mu T$, where the uncertainty represents the standard error.

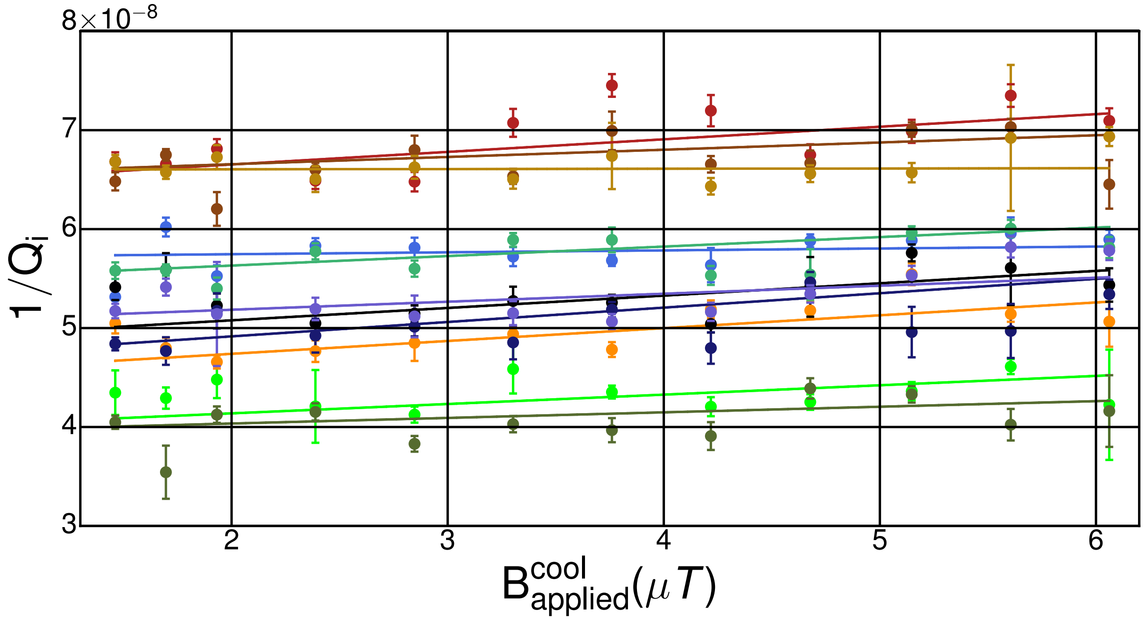

Figure A.2: (Color) The small magnetic field dependence of internal loss for 11 resonators with ground plane hole arrays. Data points of a common color correspond with a single resonator.

A.3 Hole pattern design rules

In the main text, we describe the hole pattern as having a constant distance between the edges of adjacent holes and between the resonator edge and the nearest hole. However, the curved portion of our meandered resonator geometry does not allow us to easily satisfy both of these constraints simultaneously. We expect that excess dielectric loss from hole patterns will be primarily determined by the resonator edge to hole edge distance and dominated by the row of holes nearest the resonator edge. The compromise that we have adopted is to have two rows of holes follow the contour of the resonator with a constant spacing between adjacent holes and the resonator edge. This composite structure is then embedded in a rectangular array of regularly spaced holes. An example is shown in fig. A.3. This allows us to maintain a constant resonator to hole edge distance for the entire length of the resonator.

In the main text, we claim that the maximum in Q_i is obtained at an applied magnetic field that cancels the ambient field. If the Q_i maximum were due to vortex mediated quasiparticle recombination[69] rather than field cancellation then we would expect to observe a second maximum at a symmetric, negative magnetic field. Fig A.4 shows the field dependence of Q_i at both positive and negative fields for four resonators without flux-trapping holes on one circuit from the ebeam deposited film. The absence of a second maximum at negative fields shows that vortex mediated quasiparticle recombination does not play an important role in determining Q_i in

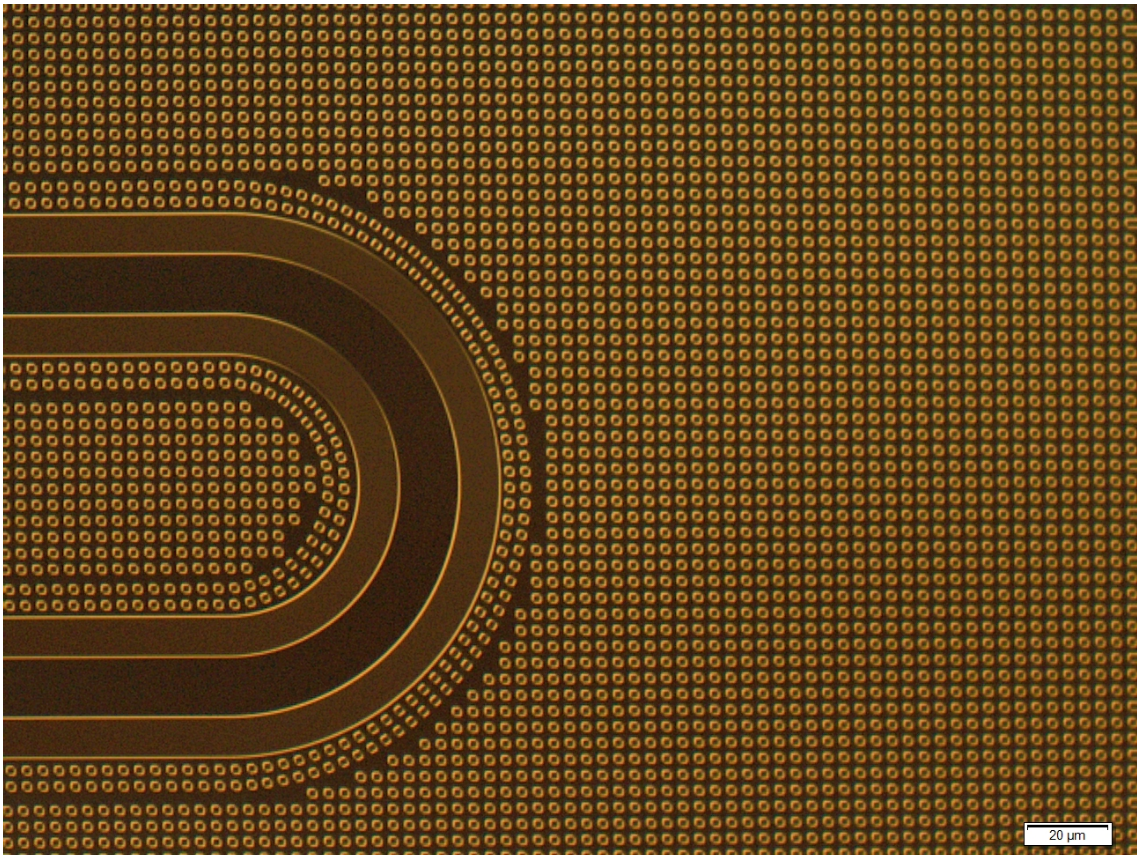

Figure A.3: The meandered section of a $\lambda/4$ resonator with a flux trapping holes showing two rows holes following the contour of the meander and the rectangular array of holes in which the resonator is embedded.

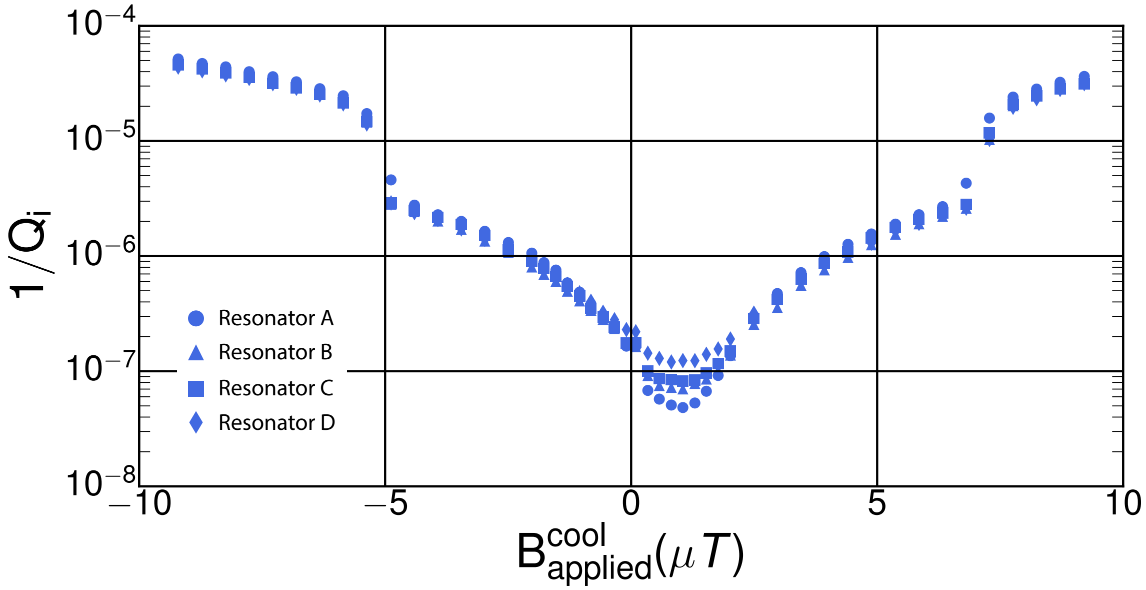

Figure A.4: The full field dependence of Q_i for four resonators without flux-trapping holes from the ebeam deposited film (Resonator A, B, C, and D). The single loss minimum is observed when the total magnetic field is zero.

our system. This is expected because our cryostat features extensive shielding and filtering to reduce the number of nonequilibrium quasiparticles and we operate the resonators well below T_c so that the number of thermal quasiparticles is also small.

A.4 Dielectric loss estimate

In the main text, we claim that the TLS loss due to the densest hole pattern is $2.5 \pm 1.3 \times 10^{-7}$. This claim is derived from measurements of 23 resonators summarized in table A.1. We use the R statistics package[129] to apply a linear regression to this data set, accounting for both the deposition technique and the hole pattern. No

Table A.1: Deposition condition, hole density, and TLS model parameters extracted from the power dependence at $B_{\text{applied}}^{\text{cool}} = 0$

Deposition	1/d (μm^{-1})	$1/Q_{\text{tls}}$	$1/Q_0$	N_{sat}	α
MBE	0	7.3e-07	3.55e-08	21.8	0.81
MBE	0	6.59e-07	4.92e-08	35.4	0.73
MBE	0	1.19e-06	5e-08	10.7	0.71
MBE	0	7.44e-07	5.82e-08	71.3	0.73
MBE	0	7.3e-07	3.32e-08	54.1	0.82
MBE	0	8.73e-07	4.44e-08	34.1	0.79
MBE	0	9.4e-07	6.64e-08	52.7	0.75
MBE	0.5	8.9e-07	4.01e-08	24.6	0.71
MBE	0.5	9.26e-07	5.29e-08	16.4	0.68
MBE	0.5	1.03e-06	4.23e-08	39.1	0.81
MBE	0.5	1.56e-06	5.35e-08	36.4	0.86
ebeam	0	1.1e-06	3.77e-08	20.1	0.75
ebeam	0	1.26e-06	5.61e-08	9.7	0.69
ebeam	0	1.2e-06	7.21e-08	34.8	0.74
ebeam	0	1.63e-06	8.55e-08	37.3	0.80
ebeam	0	1.88e-06	4.18e-08	8.0	0.78
ebeam	0	1.23e-06	5.24e-08	10.6	0.64
ebeam	0	1.63e-06	5.92e-08	20.5	0.70
ebeam	0	1.18e-06	8.75e-08	30.5	0.61
ebeam	0.5	1.06e-06	5.25e-08	50.8	0.82
ebeam	0.5	1.54e-06	7.52e-08	30.8	0.80
ebeam	0.5	1.55e-06	5.06e-08	25.8	0.74
ebeam	0.5	2.3e-06	7.83e-08	12.6	0.77

interaction term was included in this model because the interaction between hole pattern and deposition technique was found to be statistically insignificant. This analysis yields an estimate for TLS loss due to the dense hole pattern, the standard error of that estimated value, and a p-value indicating the statistical significance of this finding. Those values were respectively 2.5×10^{-7}, 1.3×10^{-7}, and 0.07.

Appendix B

Analog Control

Using a quantum computer to simulate quantum dynamics requires the ability to generate Hamiltonians with programmable coefficients. This requires us to develop a mapping between control voltages set by the experimentalist and the resultant Hamiltonian parameters. We refer to this mapping as a control model. We arrive at a control model with a two step calibration process described in this appendix. In the first stage of the control model calibration, we use a series of single and two qubit measurements to infer the parameters of the circuit model describing the device. The details of the effective circuit model for this tunably coupled device were first worked out in [26]. In the second stage of the control model calibration, we use the many-body Ramsey technique to benchmark the collective dynamics of the circuit, with all qubits coupled and near resonance with one another. Next, we numerically optimize the control model parameters using the difference between the benchmarking data and control model predictions as a cost function. This is the calibration procedure that was used to make the many-body localization measurements of chapter 5.

B.1 Spectroscopy

In the first stage of calibration we use conventional probe tone spectroscopy to measure the $|0\rangle \to |1\rangle$ and $|1\rangle \to |2\rangle$ transition frequencies for each qubit. These measurements are made with all other qubits biased far off resonance.

In order to make these measurements, we apply a bias voltage to the qubit's flux bias control and apply a variable frequency probe tone to the qubit's microwave control. Then we read out the qubit's $|1\rangle$ population. We identify the qubit's transition frequency as the probe frequency that gives maximum population transfer to the excited state. This procedure is repeated as a function of qubit bias. We similarly measure the $|1\rangle \to |2\rangle$ transition frequency, which captures the nonlinearity of the device and ultimately controls the "Hubbard U" interaction term of our Bose-Hubbard Hamiltonian. The resulting curves are fit parametrically to give circuit element values for our physical device model. This is shown in Fig. B.1(a).

It is important to note that the effective inductance qubit is sensitive to the inductance of the coupler. This enables us to infer the circuit parameters of the coupler by measuring the qubit frequency as a function of coupler bias. Example data from this procedure is shown in Fig. B.1(b).

The direct qubit - qubit interaction strength cannot be characterized from single qubit measurements alone. In order to measure the direct interaction, we use a two qubit swapping experiment as shown in Fig. B.1(c). The hopping strength is inferred from the on resonance hopping rate.

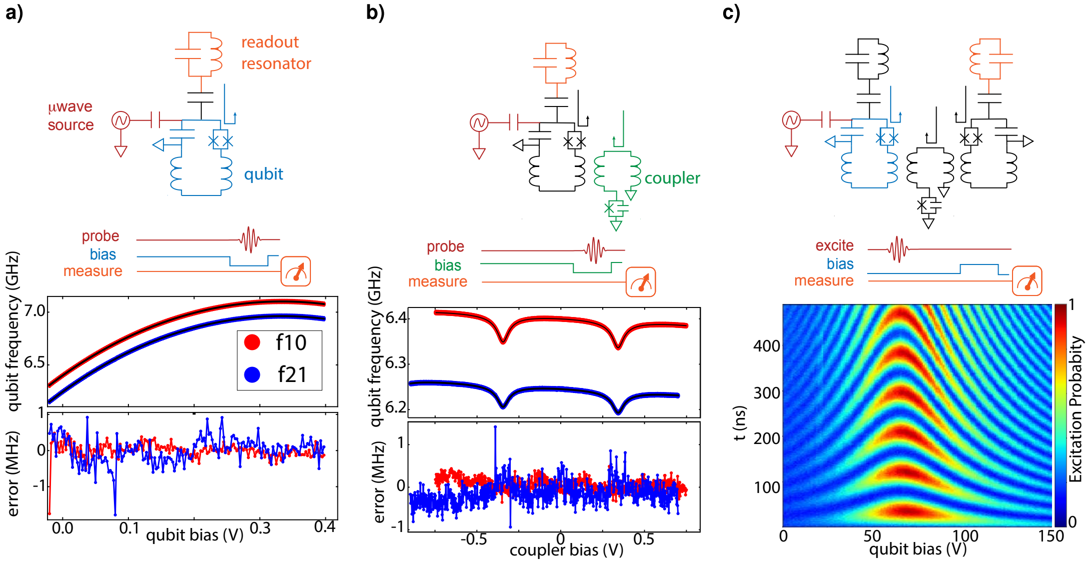

Figure B.1: a) Qubit spectroscopy measurement circuit diagram, pulse sequence, and example data. The error plot in the example data corresponds to the difference between the data points and prediction from the parameterized control model. b) Coupler spectroscopy measurement circuit diagram, pulse sequence and example data. c) Direct interaction "Chevron" measurement. The Hamiltonian hopping coefficient is obtained from the on resonance hopping rate.

In the tables below we report our measured circuit model parameters. We find circuit model parameters in good agreement with previous characterizations of this device.[26]

Table B.1: Measured qubit parameters

Qubit	C (fF)	Lj_0 (nH)	Lg_{total} (nH)	V_{offset} (A.U.)	V/Φ_0 (A.U.)	g_{readout} (MHz)
q_1	87.0	6.28	1.00	0.037	0.756	95.5
q_2	84.2	6.20	1.07	0.076	0.762	90.6
q_3	84.4	6.27	1.02	0.073	0.764	92.1
q_4	82.8	6.52	1.11	0.057	0.762	76.0
q_5	85.0	6.14	0.97	0.095	0.763	93.3
q_6	88.3	6.13	0.82	0.057	0.760	105.1
q_7	80.7	6.58	1.25	0.054	0.747	76.4
q_8	85.4	6.27	0.96	0.064	0.762	99.2
q_9	85.6	6.38	0.95	0.044	0.785	97.0

Table B.2: Measured coupler parameters

Coupler	M_{left} (pH)	M_{right} (pH)	β_{max}	f_0 (GHz)	V_{offset} (A.U.)	V/Φ_0 (A.U.)
$c_{1,2}$	45.0	42.3	0.675	15.1	0.694	0.965
$c_{2,3}$	45.4	41.6	0.678	14.9	0.683	0.964
$c_{3,4}$	45.1	42.8	0.684	15.0	0.682	0.956
$c_{4,5}$	46.1	41.3	0.681	14.9	0.685	0.961
$c_{5,6}$	42.9	37.5	0.669	14.4	0.682	0.963
$c_{6,7}$	41.2	42.0	0.676	14.5	0.672	0.952
$c_{7,8}$	47.0	40.9	0.691	14.9	0.676	0.963
$c_{8,9}$	44.6	38.6	0.680	15.0	0.686	0.958

B.2 Many-body Ramsey spectroscopy

Many-body Ramsey spectroscopy is the primary benchmarking technique for our multi-qubit, time-independent Hamiltonians [103]. This technique allows us to extract the eigenvalues of a time independent Hamiltonian. We can then compare the extracted eigenvalues with those predicted from our control model to establish a measure of fidelity. In this appendix we give a detailed discussion of many-body Ramsey spectroscopy and its use in validating and optimizing our control model.

For a wavefunction $|\psi\rangle$ evolving under a time independent Hamiltonian H we can write down the time dependence of $|\psi\rangle$ by expanding it in the energy eigenbasis.

$$|\psi(t)\rangle = e^{-iHt}|\psi_0\rangle = \sum_{\alpha} C_{\alpha} e^{-iE_{\alpha}t}|\phi_{\alpha}\rangle \tag{B.1}$$

The coefficients C_{α} are given by the overlap of the initial state with the eigenstates of H.

$$C_{\alpha} = \langle\phi_{\alpha}|\psi_0\rangle \tag{B.2}$$

Looking at Eq. B.1, it is clear that if we could simply Fourier transform the wavefunction, the task ef extracting the eigenvalues of H would be complete. Unfortunately, $|\psi\rangle$ is not an observable and our ability to interogate $|\psi\rangle$ is limited to measuring the expectation values of Hermitian operators. Such an observable $\hat{O}$ can be expanded in the energy basis as

$$\hat{O} = \sum_{\alpha,\alpha'} O_{\alpha,\alpha'}|\phi_{\alpha'}\rangle\langle\phi_{\alpha}| \tag{B.3}$$

The time dependent expectation value of this operator is

$$O(t) \equiv \langle \hat{O}(t) \rangle = \langle \psi(t) | \hat{O} | \psi(t) \rangle =$$

$$\left(\sum_{\beta} C_{\beta}^{*} e^{iE_{\beta} t} \left| \phi_{\beta} \right\rangle \right) \left(\sum_{\alpha,\alpha'} O_{\alpha,\alpha'} \left| \phi_{\alpha'} \right\rangle \left\langle \phi_{\alpha} \right| \right) \left(\sum_{\beta'} C_{\beta'} e^{-iE_{\beta'} t} \left| \phi_{\beta'} \right\rangle \right) =$$

$$\sum_{\alpha,\alpha',\beta,\beta'} \left\langle \phi_{\beta'} | \phi_{\alpha'} \right\rangle \left\langle \phi_{\beta} | \phi_{\alpha} \right\rangle C_{\beta'}^{*} C_{\beta} O_{\alpha,\alpha'} e^{i(E_{\beta'} - E_{\beta})t} =$$

$$\sum_{\alpha,\alpha'} C_{\alpha'}^{*} C_{\alpha} O_{\alpha,\alpha'} e^{-i(E_{\alpha'} - E_{\alpha})t}$$

The time dependence of $O(t)$ exposes our central challenge. For a generic initial state and a generic $\hat{O}$ the time series $O(t)$ does not isolate the eigenvalues of H. Instead, the Fourier transform of $O(t)$ reports all *energy differences* in the spectrum. In order to isolate the eigenvalues, we must engineer the initial state and measurement observables such that we keep only terms with $E_{\alpha'} = 0$.

From an engineering perspective, the above equation is still somewhat opaque because it describes the time dependence of an observable only in terms of the eigenbasis of H. Typically, however, we use the Fock basis for initialization and measurement. Thus, although the Hamiltonian evolution of the multi-qubit system is most naturally described in terms of the the eigenstates of H, the initial state and measurement observable that we wish to engineer are best described in terms of a product of single qubit states. Schematically, we can diagram our algorithm as follows:

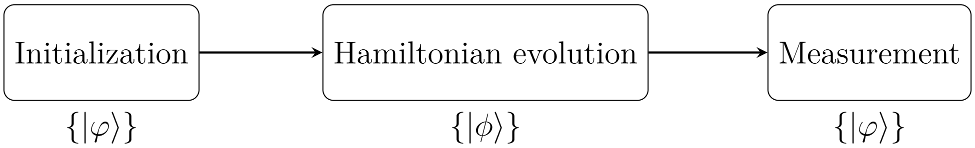

where φ and ϕ represent the Fock basis and Hamiltonian eigenbasis.

It is useful to work this out explicitly for the many-body Ramsey algorithm, demonstrating the extraction of Hamiltonian eigenvalues from the single photon manifold of a small three qubit system.

The relevant Fock basis states are:

$$\{|\varphi\}\rangle = |000\rangle\,, |001\rangle\,, |010\rangle\,, |100\rangle \tag{B.4}$$

Initializing to a superposition state by doing a Y/2 rotation on a single qubit we have:

$$|\psi_0\rangle = \frac{1}{\sqrt{2}}\big(|000\rangle + |001\rangle\big) = \frac{1}{\sqrt{2}}\big(|\varphi_0\rangle + |\varphi_1\rangle\big)$$

Let C be the matrix that changes basis from the Fock basis to the eigenbasis of H.

$$|\psi_0\rangle_\phi = \frac{1}{\sqrt{2}}\begin{bmatrix} 1 & 0 & 0 & 0 \\ 0 & c_{11} & c_{12} & c_{13} \\ 0 & c_{21} & c_{22} & c_{23} \\ 0 & c_{31} & c_{32} & c_{33} \end{bmatrix}_{\varphi\to\phi} \begin{bmatrix} 1 \\ 1 \\ 0 \\ 0 \end{bmatrix}_\varphi = \frac{1}{\sqrt{2}}\begin{bmatrix} 1 \\ c_{11} \\ c_{21} \\ c_{31} \end{bmatrix}_\phi \tag{B.5}$$

Where the subscripts indicate which basis we are working in. The time dependence of $|\psi\rangle$ is

$$|\psi(t)\rangle_\phi = \begin{bmatrix} 1 \\ c_{11}\,e^{-iE_1 t} \\ c_{21}\,e^{-iE_2 t} \\ c_{31}\,e^{-iE_3 t} \end{bmatrix}_\phi \tag{B.6}$$

We can apply the inverse transformation C^{-1} to recover the time dependence of $|\psi\rangle$ in the Fock (measurement) basis.

$$|\psi(t)\rangle_{\varphi} = C^{-1}\,|\psi(t)\rangle = \frac{1}{\sqrt{2}}\begin{bmatrix}1 & 0 & 0 & 0\\ 0 & c^{-1}_{11} & c^{-1}_{12} & c^{-1}_{13}\\ 0 & c^{-1}_{21} & c^{-1}_{22} & c^{-1}_{23}\\ 0 & c^{-1}_{31} & c^{-1}_{32} & c^{-1}_{33}\end{bmatrix}_{\phi\to\varphi}\begin{bmatrix}1\\ c_{11}\,e^{-iE_1t}\\ c_{21}\,e^{-iE_2t}\\ c_{31}\,e^{-iE_3t}\end{bmatrix}_{\phi}$$

$$= \frac{1}{\sqrt{2}}\begin{bmatrix}1\\ c^{-1}_{11}c_{11}\,e^{-iE_1t} + c^{-1}_{12}c_{21}\,e^{-iE_2t} + c^{-1}_{13}c_{31}\,e^{-iE_3t}\\ c^{-1}_{21}c_{11}\,e^{-iE_1t} + c^{-1}_{22}c_{21}\,e^{-iE_2t} + c^{-1}_{23}c_{31}\,e^{-iE_3t}\\ c^{-1}_{31}c_{11}\,e^{-iE_1t} + c^{-1}_{32}c_{21}\,e^{-iE_2t} + c^{-1}_{33}c_{31}\,e^{-iE_3t}\end{bmatrix}_{\varphi} \equiv \frac{1}{\sqrt{2}}\begin{bmatrix}1\\ \varphi_{001}\\ \varphi_{010}\\ \varphi_{100}\end{bmatrix}_{\varphi}$$

In the zero and one photon manifolds of the 3 qubit system

$$\hat{I}\otimes\hat{I}\otimes\left(\hat{\sigma}^x + i\hat{\sigma}^y\right) = \begin{bmatrix}0 & 2 & 0 & 0\\ 0 & 0 & 0 & 0\\ 0 & 0 & 0 & 0\\ 0 & 0 & 0 & 0\end{bmatrix}, \tag{B.7}$$

and therefore, if we measure $\langle\sigma^x + i\sigma^y\rangle(t)$ on the rightmost site, then we have

$$\begin{bmatrix}1 & \varphi^*_{001} & \varphi^*_{010} & \varphi^*_{100}\end{bmatrix}\begin{bmatrix}0 & 1 & 0 & 0\\ 0 & 0 & 0 & 0\\ 0 & 0 & 0 & 0\\ 0 & 0 & 0 & 0\end{bmatrix}\begin{bmatrix}1\\ \varphi_{001}\\ 0\\ 0\end{bmatrix} = \begin{bmatrix}1 & \varphi^*_{001} & \varphi^*_{010} & \varphi^*_{100}\end{bmatrix}\begin{bmatrix}\varphi_{001}\\ 0\\ 0\\ 0\end{bmatrix} = \varphi_{001}. \tag{B.8}$$

In this case we can recover the eigenvalues of H because the Fourier transform of $\varphi_{001}(t)$ reports tones only at the eigenfrequencies, since $\varphi_{001} = c_{11}^{-1} c_{11} e^{-iE_1 t} + c_{12}^{-1} c_{21} e^{-iE_2 t} + c_{13}^{-1} c_{31} e^{-iE_3 t}$.

This calculation makes the roles of the initial state and measurement observable clear. It is essential that the initial state be a superposition of a reference state, and a state in the manifold that we wish to extract the eigenvalues of. It is critical that the reference state is member of a manifold with trivial internal dynamics, in this case $|\psi\rangle_{ref} = |000\rangle$. This state serves as an interference partner for our generalized Ramsey experiment, and its triviality assures that the spectrum of our interference pattern is exclusively due to the dynamics of the target manifold and not the internal dynamics of the reference manifold.

The choice of $\hat{O} = \hat{a} = \hat{\sigma}^x + i\hat{\sigma}^y$ is also clarified by this calculation. This operator interferes the dynamic manifold with the reference state, isolating the eigenvalues.

If we had instead chosen $\hat{O} = \hat{\sigma}^x$ we would observe both positive and negative eigenvalues since

$$\begin{bmatrix} 1 & \varphi_{001}^* & \varphi_{010}^* & \varphi_{100}^* \end{bmatrix} \begin{bmatrix} 0 & 1 & 0 & 0 \\ 1 & 0 & 0 & 0 \\ 0 & 0 & 0 & 0 \\ 0 & 0 & 0 & 0 \end{bmatrix} \begin{bmatrix} 1 \\ \varphi_{001} \\ \varphi_{010} \\ \varphi_{100} \end{bmatrix} = \begin{bmatrix} 1 & \varphi_{001}^* & \varphi_{010}^* & \varphi_{100}^* \end{bmatrix} \begin{bmatrix} \varphi_{001} \\ 1 \\ 0 \\ 0 \end{bmatrix} = \varphi_{001} + \varphi_{001}^* \tag{B.9}$$

This is intuitive because for a single qubit precessing on the equator of the Bloch sphere measuring $< \sigma^x >$ alone does not indicate which direction the Bloch vector is precessing!

The naive attempt of measuring the on-site population of qubit 1 $\hat{n}_1$ yields the eigenvalue differences since

$$\begin{bmatrix} 1 & \varphi_{001}^* & 0 & 0 \end{bmatrix} \begin{bmatrix} 0 & 0 & 0 & 0 \\ 0 & 1 & 0 & 0 \\ 0 & 0 & 0 & 0 \\ 0 & 0 & 0 & 0 \end{bmatrix} \begin{bmatrix} 1 \\ \varphi_{001} \\ 0 \\ 0 \end{bmatrix} = \mid \varphi_{001} \mid^2 \tag{B.10}$$

The numerics below illustrate these points:

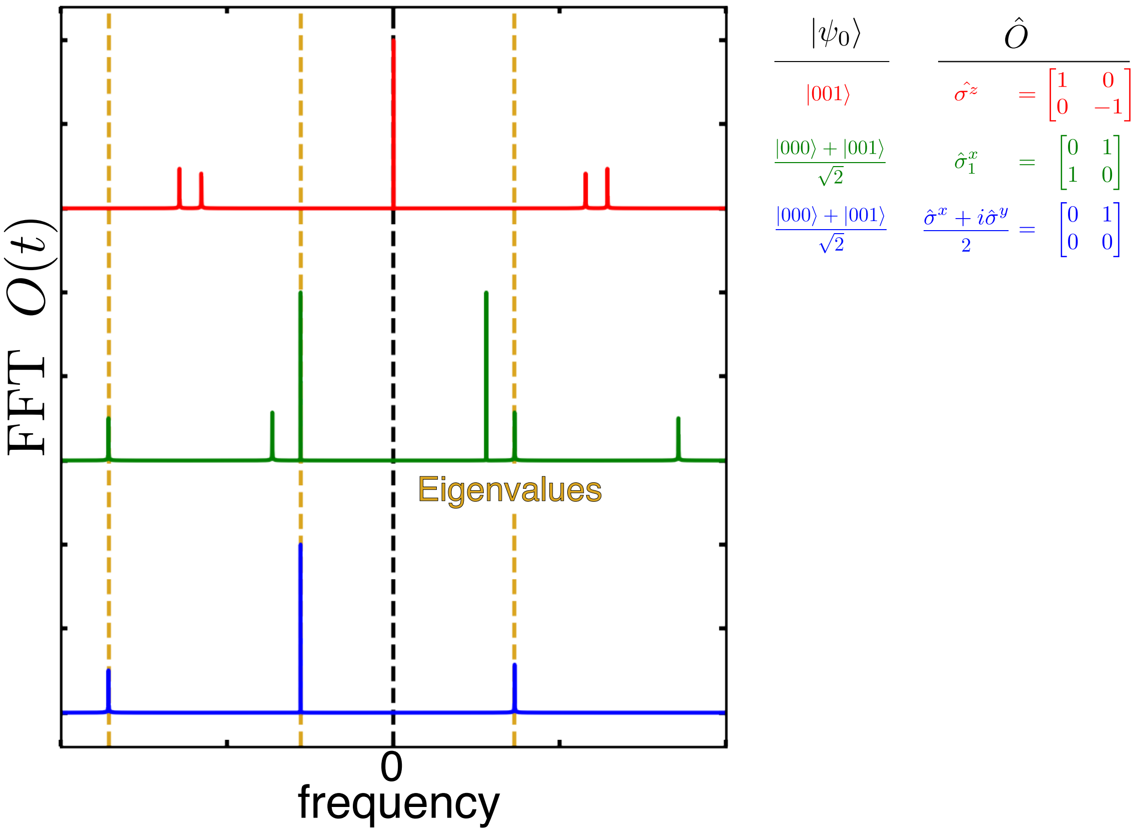

Figure B.2: The spectrum of $\hat{O} = \sigma^z$ is comprised of the differences of eigenvalues. The spectrum of $\hat{O} = \sigma^x$ contains the eigenvalues and their mirrored frequencies. The spectrum of $\hat{O} = \sigma^x + i\sigma^y$ isolates the eigenvalues.

B.3 Control model optimization

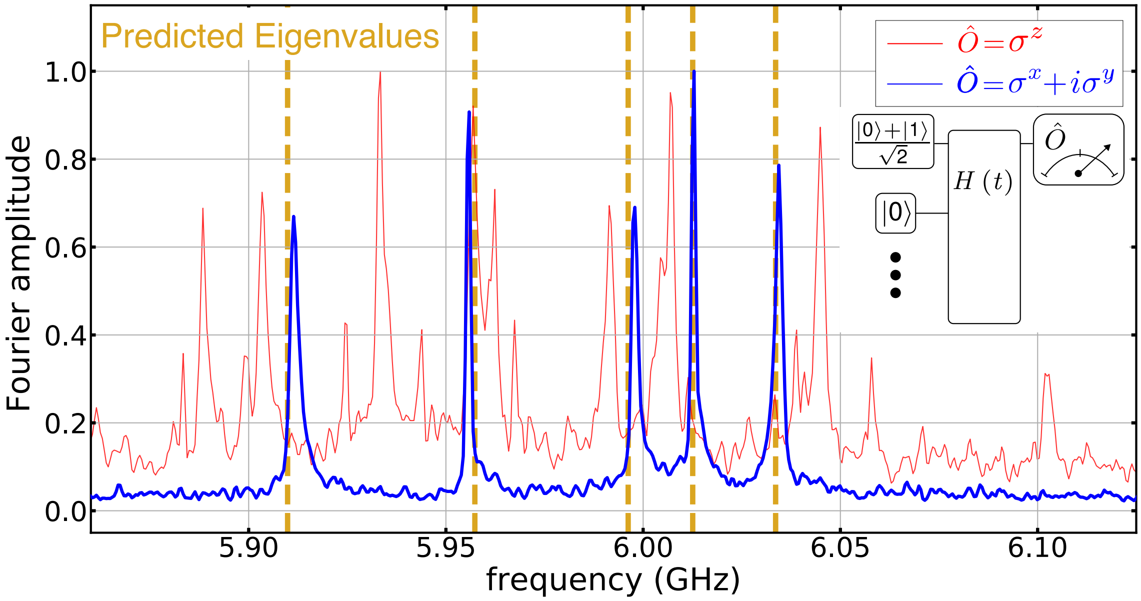

Figure B.3: Many-body Ramsey five qubit data. The fourier domain data for measurement observables $\langle\hat{O}\rangle = \langle\sigma^z\rangle$ (red) and $\langle\sigma^x + i\sigma^y\rangle$ (blue). The spectrum of $\left\langle\sigma^z(t)\right\rangle$ is composed of artifacts from eigenvalue differences. The spectrum of $\left\langle\sigma^x(t)\right\rangle + i\left\langle\sigma^y(t)\right\rangle$ recovers the eigenvalues of H.

Because the many-body Ramsey extracts the eigenvalues of the Hamiltonian that was actually generated in the experiment, we can compare the extracted eignevalues with those predicted by our circuit parameterization and use the difference as a control error metric. A comparison of predicted eigenvalues for a single Hamiltonian instance and observed Fourier domain data from the Many-body Ramsey technique is the subject of Fig. B.3. With this error metric established, we can optimize the parameters of our control model to give a more accurate parameterization of the circuit.

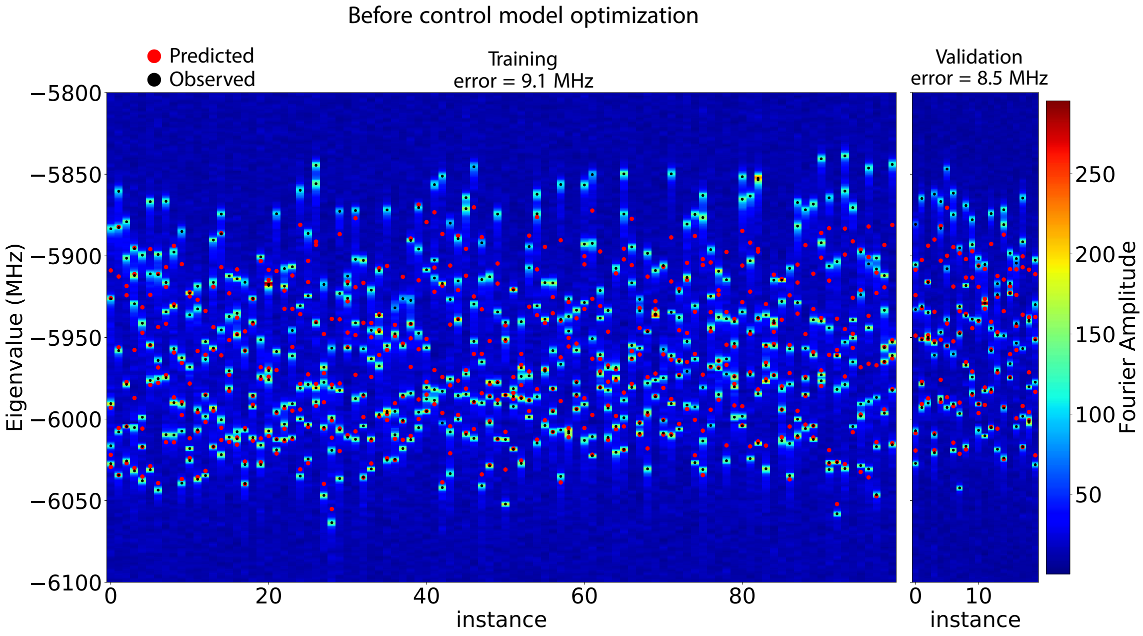

Figure B.4: Five qubit many-body Ramsey spectroscopy data overlayed with predictions from control model prior to optimization.

After using the conventional spectroscopy, described in above in section B.1, to measure the circuit model parameters using a series of single and two qubit measurements we benchmark the collective dynamics of the full system using the many-body Ramsey technique described in section B.2

The result is shown in fig. B.4. The 2D color plot is the raw Fourier data for each of 100 training instances. This data is overlayed with the control model predictions (red circles) and peak positions extracted with our analysis algorithm (black circles). The error per eigenvalue is extracted to be 9 MHz. This large error results primarily from the fact that the control bias conditions are different in the case that we characterize the single and two qubit systems from the case that we characterize the full system collective dynamics with many-body Ramsey. This idea is sketched in Fig. B.5.

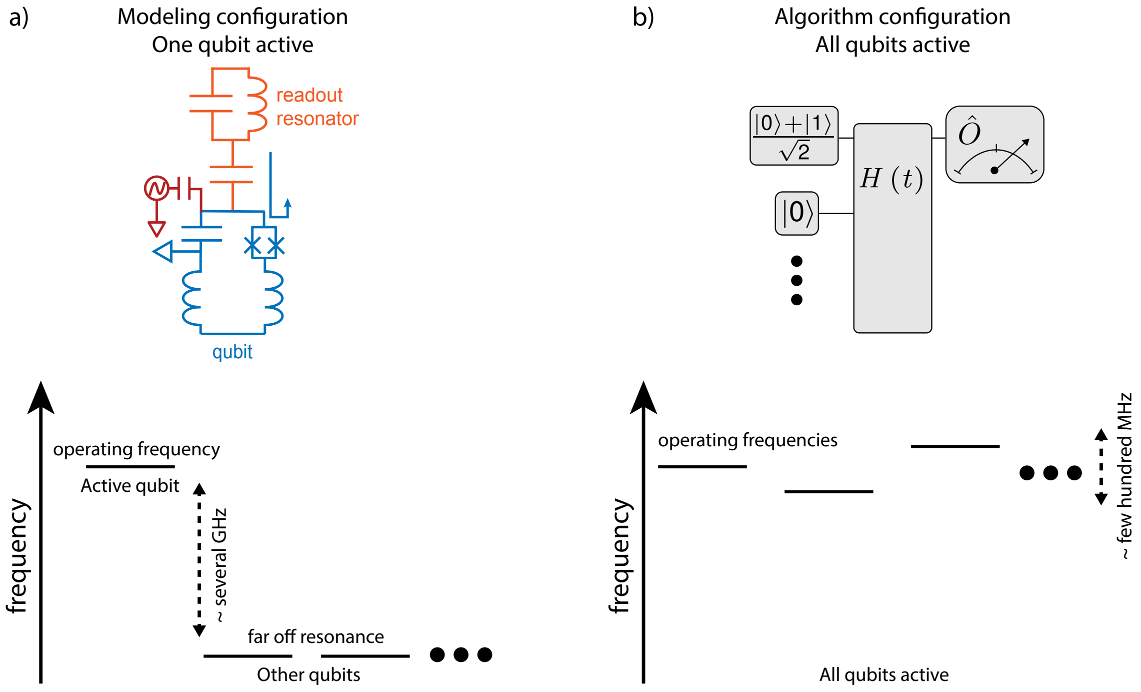

Figure B.5: Schematic illustrating the qubit frequency configurations for the modelling spectroscopy experiments **(a)** and the Many-body Ramsey benchmarking experiments **(b)**.

We can improve the control model by numerically optimizing the circuit parameters, using the error per eigenvalue as a cost function. In this optimization step we only allow physically justified parameters to vary. That is, the flux offsets are expected to benefit from optimization because the control bias currents are different in the spectroscopic modelling configuration and the many-body Ramsey benchmarking configuration. In contrast, parameters such as the capacitance and geometric induc-

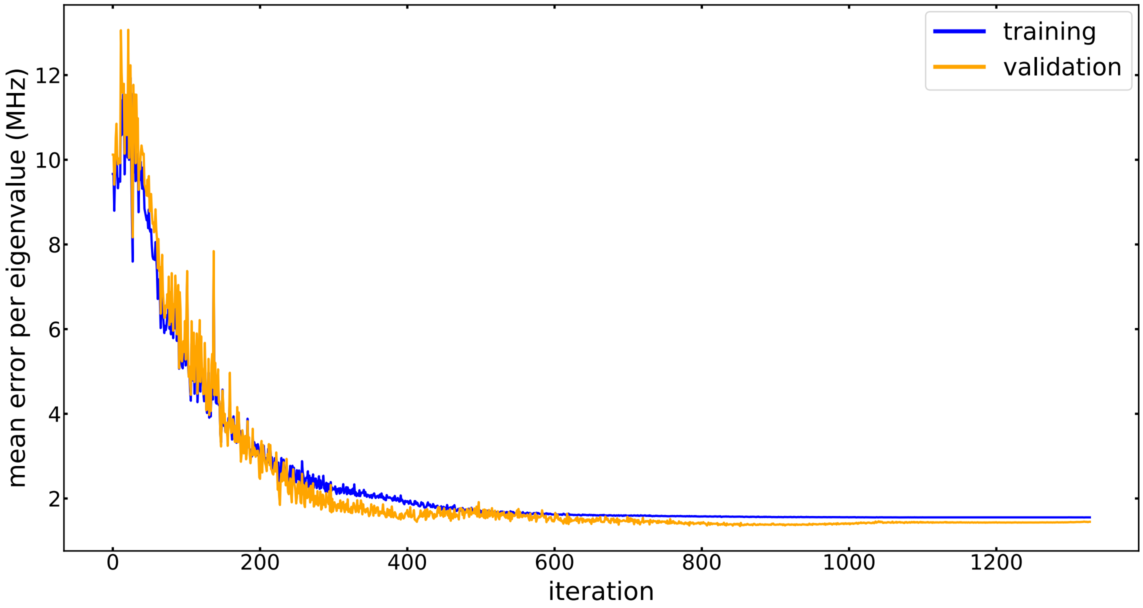

Figure B.6: Error per eigenvalue for the training and validation splits during optimization. Data shown is for five qubit Hamiltonians.

tance are not expected to have changed between bias configurations and are held fixed during the optimization. Next, we follow the standard optimization procedure of dividing our full data set into training and validation subsets. We then optimize the control model by minimizing the average error per eigenvalue of the training data only. The error per eigenvalue at each iteration of the optimization process is shown in Fig. B.6. The predictions from the optimized control model are overlayed on the original fourier data in Fig. B.7

In Fig. B.8 we show 9 qubit validation data with a validation error rate of 1.2 MHz per eigenvalue. This shows that the MHz level error rate is maintained as we scale to larger numbers of qubits.

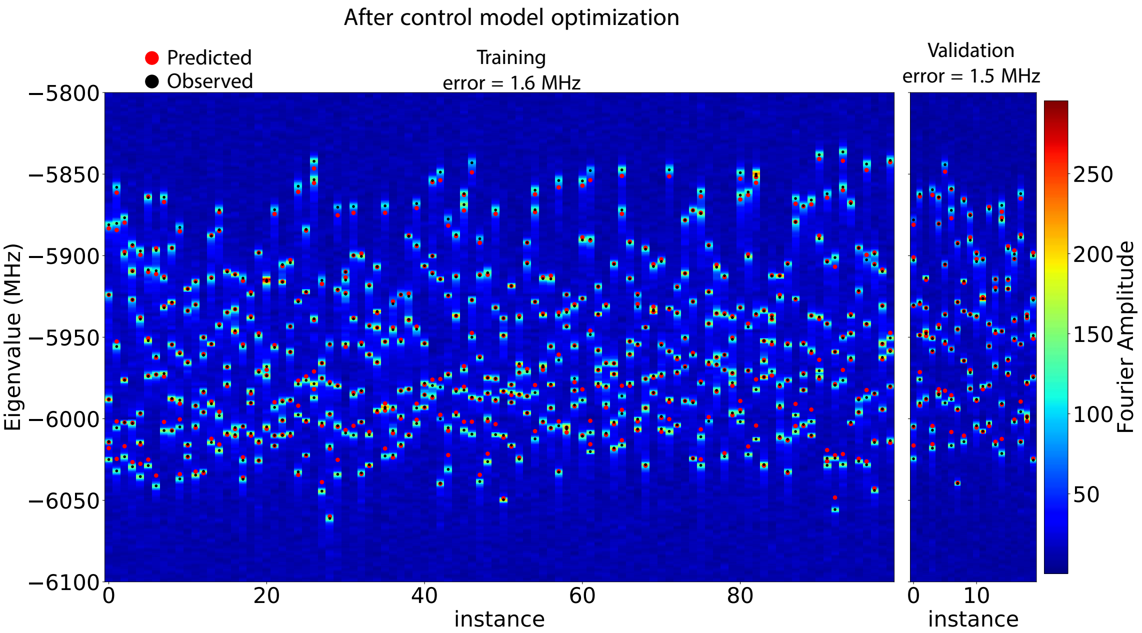

Figure B.7: Five qubit many-body Ramsey spectroscopy data overlayed with predictions from control model after optimization.

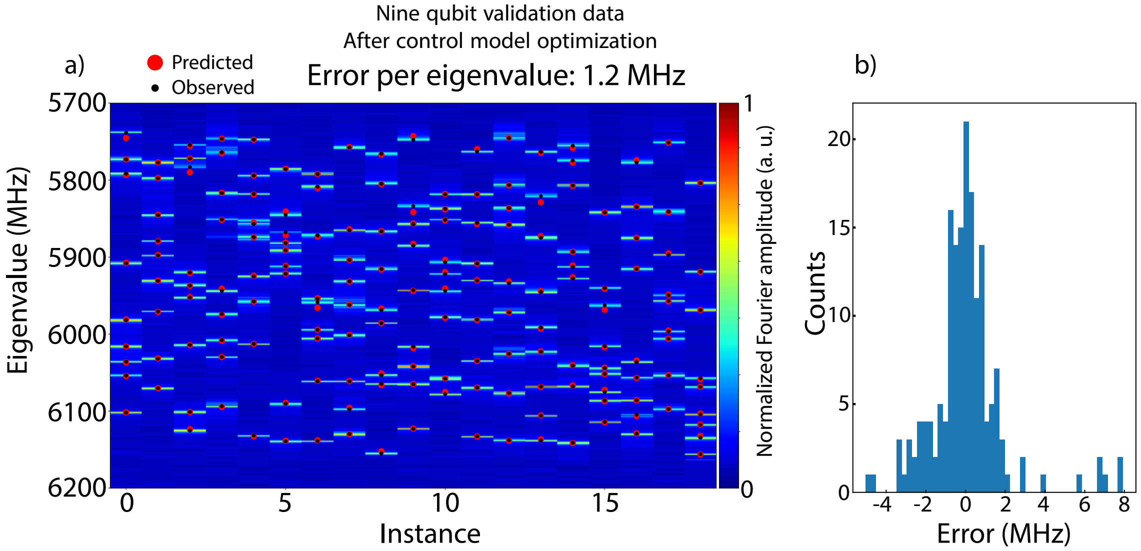

Figure B.8: Manybody Ramsey calibration data for a nine qubit linear chain a) Raw Fourier data from Many-body Ramsey spectroscopy. b) Histogram of errors for each eigenvalue.

B.4 Connection between many-body Ramsey spectroscopy and unitary tomography (2 qubit particle conserving evolution)

In the recent demonstration of quantum supremacy [6] the two qubit gates were photon number conserving unitaries from a class of unitaries known as the Fermionic Simulation or FSim class[130]. The matrix elements for the two qubit unitaries were inferred by optimizing the gate parameters to the cross-entropy benchmarking fidelity. The initial guesses for this optimization process were provided by a technique we refer to as unitary tomography. This technique is now widely used for two qubit gate calibration in the Martinis group / Google AI Quantum lab. Here we highlight the connection between the many-body Ramsey technique discussed in the previous section and the simple, powerful unitary tomography technique.

We wish to measure the matrix elements of a generic two qubit photon conserving unitary U. In order to probe U, we can apply the unitary to an initial state of our choice. We can also perform tomographic rotations prior to measurement.

$$\left\langle \hat{O} \right\rangle = \langle \psi_0 | U^\dagger \hat{O} U | \psi_0 \rangle \tag{B.11}$$

where the experimenter has control over $|\psi_0\rangle$ and $\hat{O}$ A generic two qubit unitary U has a matrix representation as below using the basis $|00\rangle, |01\rangle, |10\rangle, |11\rangle$

$$U = \begin{bmatrix} U_{00} & U_{01} & U_{02} & U_{03} \\ U_{10} & U_{11} & U_{12} & U_{13} \\ U_{20} & U_{21} & U_{22} & U_{23} \\ U_{30} & U_{31} & U_{32} & U_{33} \end{bmatrix} \tag{B.12}$$

which can be simplified for the FSim class.

$$U = \begin{bmatrix} 1 & 0 & 0 & 0 \\ 0 & U_{11} & U_{12} & 0 \\ 0 & U_{21} & U_{22} & 0 \\ 0 & 0 & 0 & U_{33} \end{bmatrix} \tag{B.13}$$

We wish to ascertain the matrix elements of this unitary transformation.

The procedure for doing this is exactly the same as for many-body Ramsey spectroscopy and is illustrated in Fig. B.9. It consists of preparing a qubit in the superposition state with a $\pi/2$ pulse, acting on the two qubit system with the unitary of interest, and measuring the observable $\langle\sigma^x\rangle + i\langle\sigma^y\rangle$. In this case our choice of which qubits were initialized and measured determines which unitary matrix element is extracted. Also in contrast with many-body Ramsey spectroscopy, we do not need to measure a full time series, but rather obtain our answer by analyzing a single application of the Unitary.

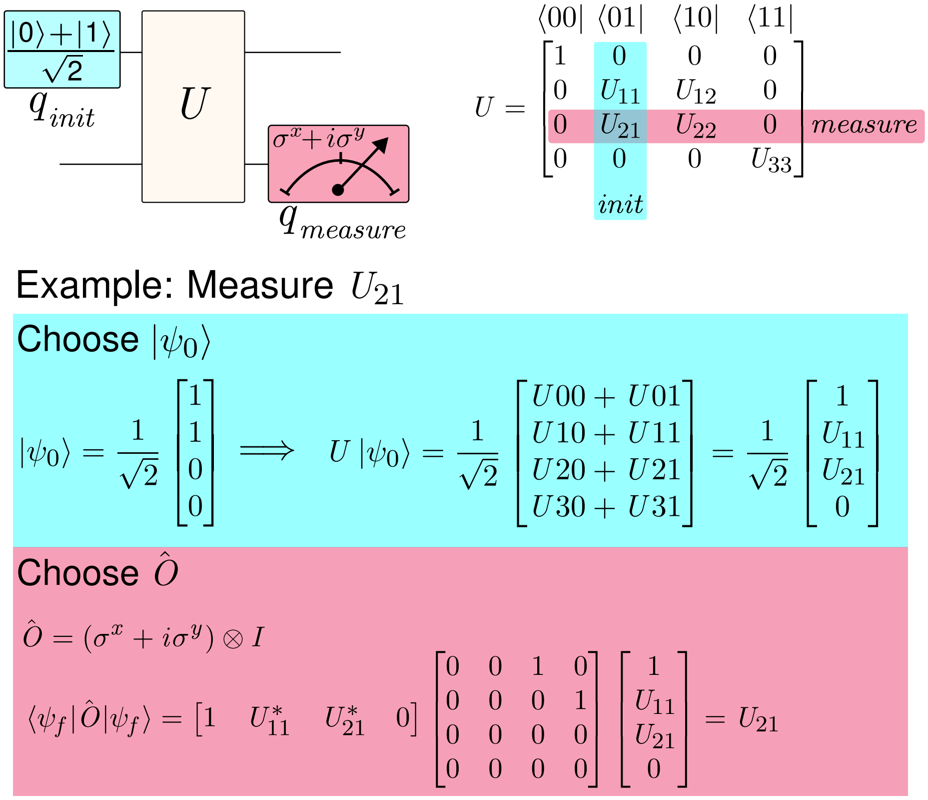

Figure B.9: A schematic diagram of the unitary tomography procedure for measuring the matrix elements of U

The mechanics of this method are best clarified by working a simple example. If we initialize the left qubit

$$|\psi_0\rangle = \frac{1}{\sqrt{2}}\begin{bmatrix}1\\1\\0\\0\end{bmatrix} \tag{B.14}$$

then

$$U|\psi_0\rangle = \frac{1}{\sqrt{2}}\begin{bmatrix}U00+U01\\U10+U11\\U20+U21\\U30+U31\end{bmatrix} = \frac{1}{\sqrt{2}}\begin{bmatrix}1\\U_{11}\\U_{21}\\0\end{bmatrix} \tag{B.15}$$

So that it is clear we are selecting elements from the first column of the single photon subspace. On the other hand, if we initialize the second qubit then we select the corresponding column of the unitary

$$|\psi_0\rangle = \frac{1}{\sqrt{2}}\begin{bmatrix}1\\0\\1\\0\end{bmatrix} \implies |\psi_f\rangle = \frac{1}{\sqrt{2}}\begin{bmatrix}1\\U_{12}\\U_{22}\\0\end{bmatrix} \tag{B.16}$$

Isolating a particular row of the unitary is achieved through the choice of which qubit is used to measure $\left\langle \sigma^x + i\sigma^y \right\rangle$. Explicitly, the measurement operator for a measurement on qubit 1 is :

$$\hat{O} = \frac{1}{2} I \otimes (\sigma^x + i\sigma^y) = \begin{bmatrix}1 & 0\\0 & 1\end{bmatrix} \otimes \begin{bmatrix}0 & 1\\0 & 0\end{bmatrix} = \begin{bmatrix}0 & 1 & 0 & 0\\0 & 0 & 0 & 0\\0 & 0 & 0 & 1\\0 & 0 & 0 & 0\end{bmatrix} \tag{B.17}$$

so that

$$\psi_f = \begin{bmatrix}1\\U_{11}\\U_{21}\\0\end{bmatrix} \implies \langle\psi_f|\hat{O}|\psi_f\rangle = \begin{bmatrix}1 & U_{11}^* & U_{21}^* & 0\end{bmatrix}\begin{bmatrix}0 & 1 & 0 & 0\\0 & 0 & 0 & 0\\0 & 0 & 0 & 1\\0 & 0 & 0 & 0\end{bmatrix}\begin{bmatrix}1\\U_{11}\\U_{21}\\0\end{bmatrix} = U_{11} \tag{B.18}$$

For a measurement on qubit 2

$$\hat{O} = \frac{1}{2}(\sigma^x + i\sigma^y) \otimes I = \begin{bmatrix}0 & 1\\0 & 0\end{bmatrix} \otimes \begin{bmatrix}1 & 0\\0 & 1\end{bmatrix} = \begin{bmatrix}0 & 0 & 1 & 0\\0 & 0 & 0 & 1\\0 & 0 & 0 & 0\\0 & 0 & 0 & 0\end{bmatrix} \tag{B.19}$$

so that

$$\psi_f = \begin{bmatrix} 1 \\ U_{11} \\ U_{21} \\ 0 \end{bmatrix} \implies \langle \psi_f | \hat{O} | \psi_f \rangle = \begin{bmatrix} 1 & U_{11}^* & U_{21}^* & 0 \end{bmatrix} \begin{bmatrix} 0 & 0 & 1 & 0 \\ 0 & 0 & 0 & 1 \\ 0 & 0 & 0 & 0 \\ 0 & 0 & 0 & 0 \end{bmatrix} \begin{bmatrix} 1 \\ U_{11} \\ U_{21} \\ 0 \end{bmatrix} = U_{21} \tag{B.20}$$

We have succeeded in measuring a single matrix element of the unitary, by mapping its magnitude and phase onto the single qubit magnitude and phase. This procedure generalizes trivially to the single photon manifold of multi-qubit systems.

Appendix C

Supplemental information for Growth and preservation of entanglement in a many-body localized system

C.1 Device and calibration, Figs. C.1-C.3

C.1.1 Circuit schematic

The nearest-neighbor coupled, linear chain device used in Figs. 5.2 - 5.4 features 9 frequency tunable transmon qubits with tunable inter-qubit coupling. An optical

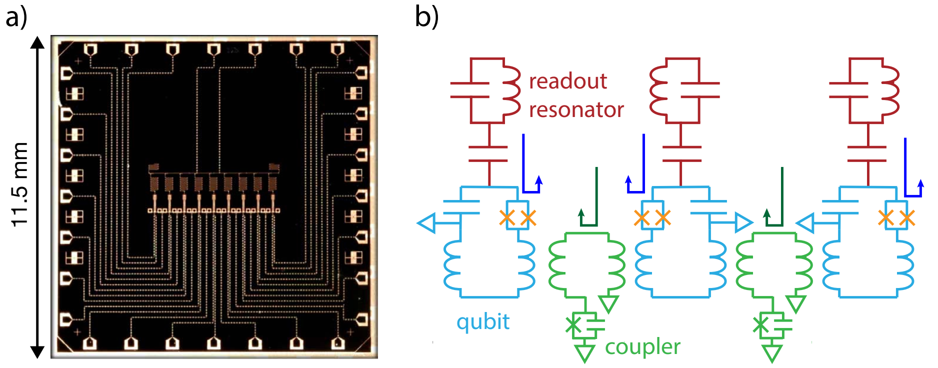

$$H_{BH}=\underbrace{\sum_{i}^{N_{coupler}} J_{i,i+1}\left(a_i^\dagger a_{i+1}+a_i a_{i+1}^\dagger\right)}_{\text{coupling (hopping)}}+\underbrace{\sum_{i}^{N_{qubit}} h_i n_i}_{\text{frequency detuning}}+\underbrace{\frac{U}{2}\sum_{i}^{N_{qubit}} n_i(n_i-1)}_{\text{qubit nonlinearity}}$$

Figure C.1: The 9 qubit linear chain device. This device was used in Figs. 5.2 - 5.4. **(a)** Optical micrograph of the 9 qubit linear-chain device. **(b)** Circuit diagram for a three qubit subsection of the device.

micrograph is of this device is shown in Fig. C.1 (a). The design details are discussed further in [26]. The effective circuit model for a three qubit, two coupler subsection of the device is shown in panel (b). Following [26], we infer the values of the circuit model parameters for this device from spectroscopic measurements. The dynamics of this device are described by a Bose-Hubbard Hamiltonian with tunable coefficients. We use the parameterized circuit model to create a mapping between the experimentally controlled bias currents and the resultant Hamiltonian coefficients. The circuit model measurements are made as a series of single and two qubit measurements. Once the circuit model has been developed, we benchmark the 9-qubit collective dynamics as described in Fig. C.3.

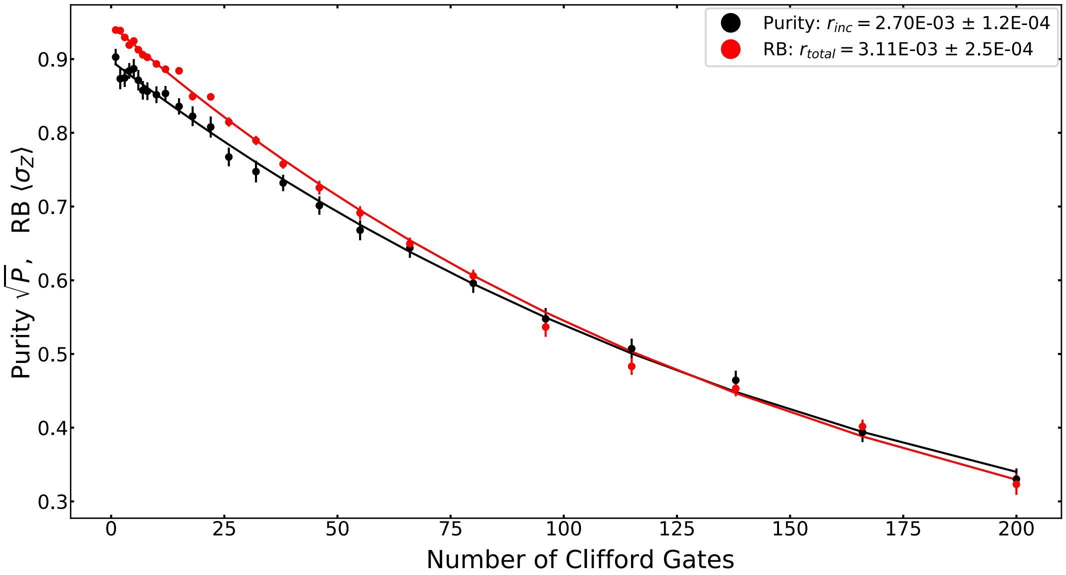

Figure C.2: Single qubit gate performance. Clifford based randomized benchmarking (RB), shown in red, characterizes the total error rate per Clifford. Purity benchmarking, shown in black, characterizes the total incoherent error rate per Clifford.

C.1.2 Single qubit gate error rate

We use Clifford based randomized benchmarking (RB) and purity benchmarking to quantify the total error rate and the error rate due to decoherence per Clifford for the single qubit gates in our algorithm. The data shown in Fig. C.2 is for a typical qubit. The total and incoherent error rates per Clifford are extracted to be 3.1×10^{-3} and 2.7×10^{-3}. Since there are relatively few single qubit gates in our analog algorithms this is not a significant source of error.

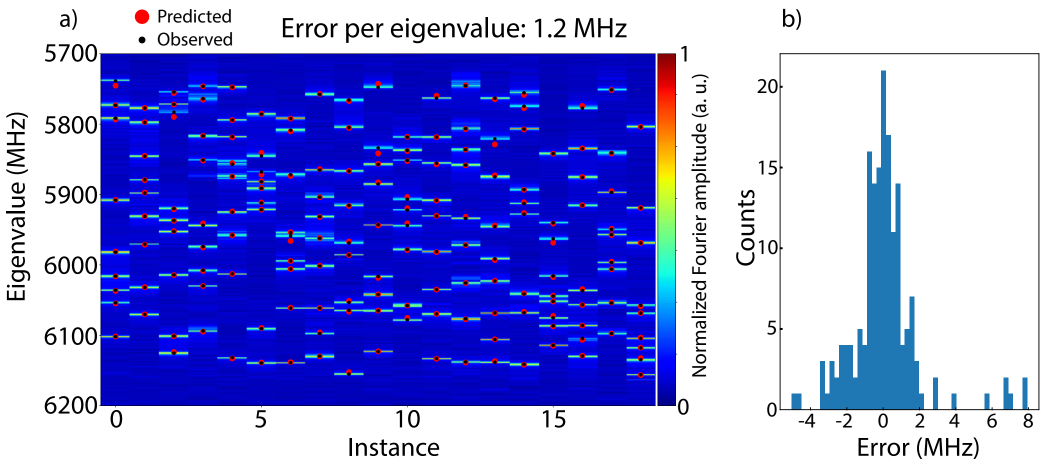

Figure C.3: Many-body Ramsey calibration data for 9 qubit randomly generated Hamiltonians. (a) Fourier data for 18 instances of randomly generated Hamiltonians overlayed with the control model predictions of the eigenvalues. **(b)** A histogram of the difference between the control model predicted eigenvalues and the experimentally observed peaks.

C.1.3 Manybody Hamiltonian benchmarking

In order to benchmark our ability to set multi-qubit time-independent Hamiltonians we compare the eigenvalues predicted by our control model with those observed by using the manybody Ramsey spectroscopy technique[103]. We prepare a qubit in the superposition state $|\psi_0\rangle = \left(\frac{|0\rangle+|1\rangle}{\sqrt{2}}\right) \otimes |0, \ldots, 0\rangle_{\text{Other}}$, evolve the system under a 9 qubit time-independent Hamiltonian, and observe $\langle \sigma^x + i\sigma^y \rangle$ of the initialized qubit vs evolution time. The eigenvalue spectrum can then be recovered by Fourier transforming this time-series. This procedure is repeated for each of the qubits in our system and a composite spectrum is assembled from these measurements. We then compare the eigenvalues predicted by the parameterized circuit model and with those extracted experimentally. Example calibration data for the 9 qubit linear chain geometry is shown is Fig. C.3.

To make a stressful test and benchmark our control model over a wide parameter space we perform manybody Ramsey spectroscopy over several instances of randomly generated Hamiltonians. In the 9 qubit data shown here, the coefficients of our target Bose-Hubbard Hamiltonian were taken to be independent random variables with $J_{ij} \in [0, 45]$MHz and $h_i \in [-200, 200]$ MHz. In Fig. C.3 (a) the 2D color map shows the composite spectra for these instances. The 2D plot is overlayed with the eigenvalue predictions from the control model (red circles) and the detected peak locations (black circles). In (b) we report the distribution of errors obtained from the difference of the predicted and observed eigenvalues for each instance. The average error per eigenvalue for these Hamiltonian instances is 1.2 MHz.

C.2 Transport measurements, Figs. C.4-C.6

C.2.1 Transport measurement instances

In Fig. C.4 we show data from the transport measurements before disorder averaging. The data shown is for $n_{ph} = 2$ and selected values of disorder parameter w for $J = 40$ MHz. The disorder averaged data (black lines) is contained in Fig. 5.2 (a), and the histograms in Fig. 5.2 (b) of the main text are time slices of this data at

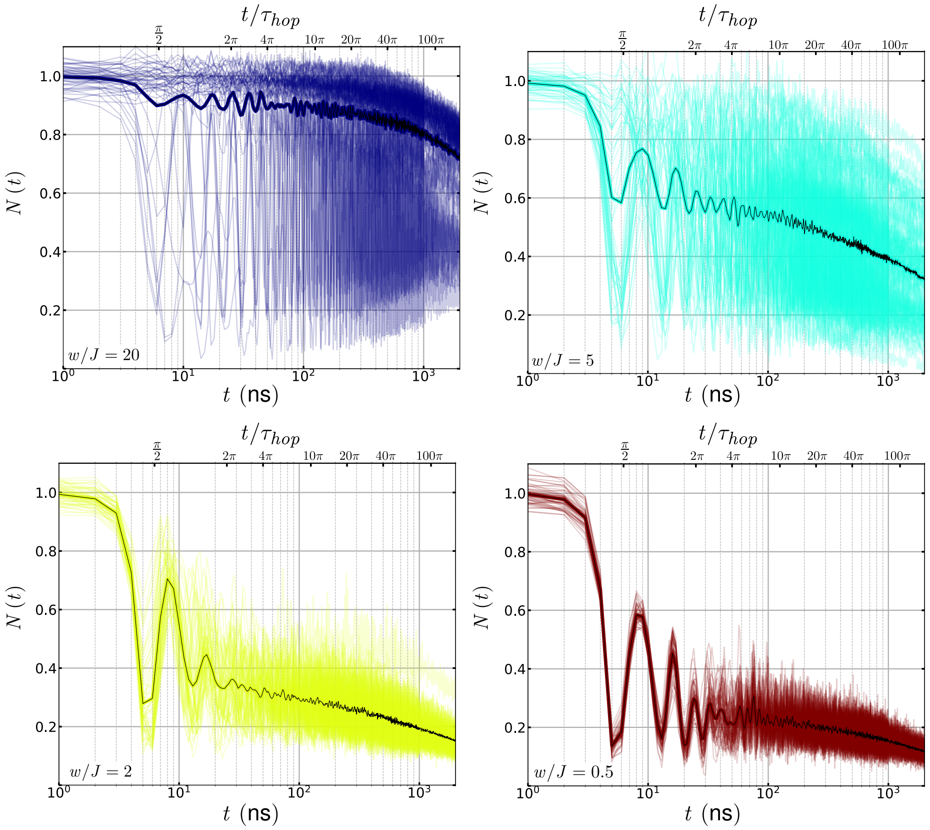

Figure C.4: Transport measurement instances. Instances of $N(t)$ for the transport protocol of Fig. 5.2 prior to disorder averaging. Data shown here is for $J = 40\,\mathrm{MHz}$ and $n_{ph} = 2$.

100 ns. The spread in values at short time is primarily due to readout error, as state preparation error is small.

C.2.2 Decoherence effects

In chapter 5 we report on short-time dynamics $t \lesssim 100\,\mathrm{ns}$, before our system is dominated by decoherence. In reality, our 9 qubit chain is an open system, subject to both relaxation and dephasing because of its coupling to the environment. The characteristic relaxation time T_1 is $\sim 10\mu$s and the characteristic dephasing time is a few μs. In Fig. C.5 we provide additional data as an estimate of the importance of these open system effects. In panel (a) we show the disorder averaged population vs time data for $n_{ph} = 1$. In panel (b) we show the population vs time data for $n_{ph} = 1$ after correcting for relaxation (photon loss) using a simple single qubit T_1 model $\overline{N^{corrected}(t)} = \overline{N(t)}/e^{(-t/10\mu s)}$. At high disorder, where the localization length is shorter than one lattice site, single qubit T_1 (photon loss to the environment) is the dominant mechanism by which a photon leaves the observation site and this correction works well, as indicated by the fact that the population has taken a stationary value. At low disorder, in the diffusive regime, the excitations are able to distribute themselves evenly across the chain and we expect the T_1 correction to work well in this case as well. Referring to Fig. 5.2 (c) we see that at 100 ns in the diffusive regime at low disorder we measure the thermal expectation values. This indicates clearly that relaxation effects are not significant in the first 100 ns. And that any apparent loss is due to transport within the 9 qubit chain and not photon loss. For intermediate disorders there appears to be additional photon loss since the onsite population declines. However, the decrease in observed population at the observation site is attributed to dephasing assisted delocalization.[119–123]

When the LIOM extends over multiple lattice sites, dephasing between the sites breaks down the localized wave-packet by destroying the quantum interference pattern that causes the localization. This breakdown of coherence between different parts of the wave packet enables transport of the excitation across the 9 qubit chain. Crucially, we note that neither T_1 relaxation nor dephasing between the lattice sites significantly influence the dynamics at higher disorders or short times. This feature is captured in Fig. 5.4 (b) where we note that $\overline{\langle \sigma^z \rangle}$ is nearly constant between 10 ns and 100 ns. In Fig. C.5 (c) and (d) we show the raw and T_1 corrected data for $n_{ph} = 2$.

C.2.3 Two state occupation

A critical feature of our system is that multiple excitations in the system may interact via the Hubbard interaction. The form of this interaction $H_{int} = \frac{U}{2} \sum_{n=1}^{n_Q} a_n^\dagger a_n (a_n^\dagger a_n - 1)$ indicates that it is only activated when there are multiple excitations on the same lattice site. Thus the interaction effects that we report in the main text require occupation of the higher levels of our Bose-Hubbard lattice. In Fig. C.6 we report the $|2\rangle$ population vs time for a system initially in the state $|\psi_0\rangle = |000000101\rangle$ and observed on the right-most qubit. We find that the $|2\rangle$ state population is typically at the 2 % level, achieves its maximum value early in the evolution, and does not progressively grow larger with time.

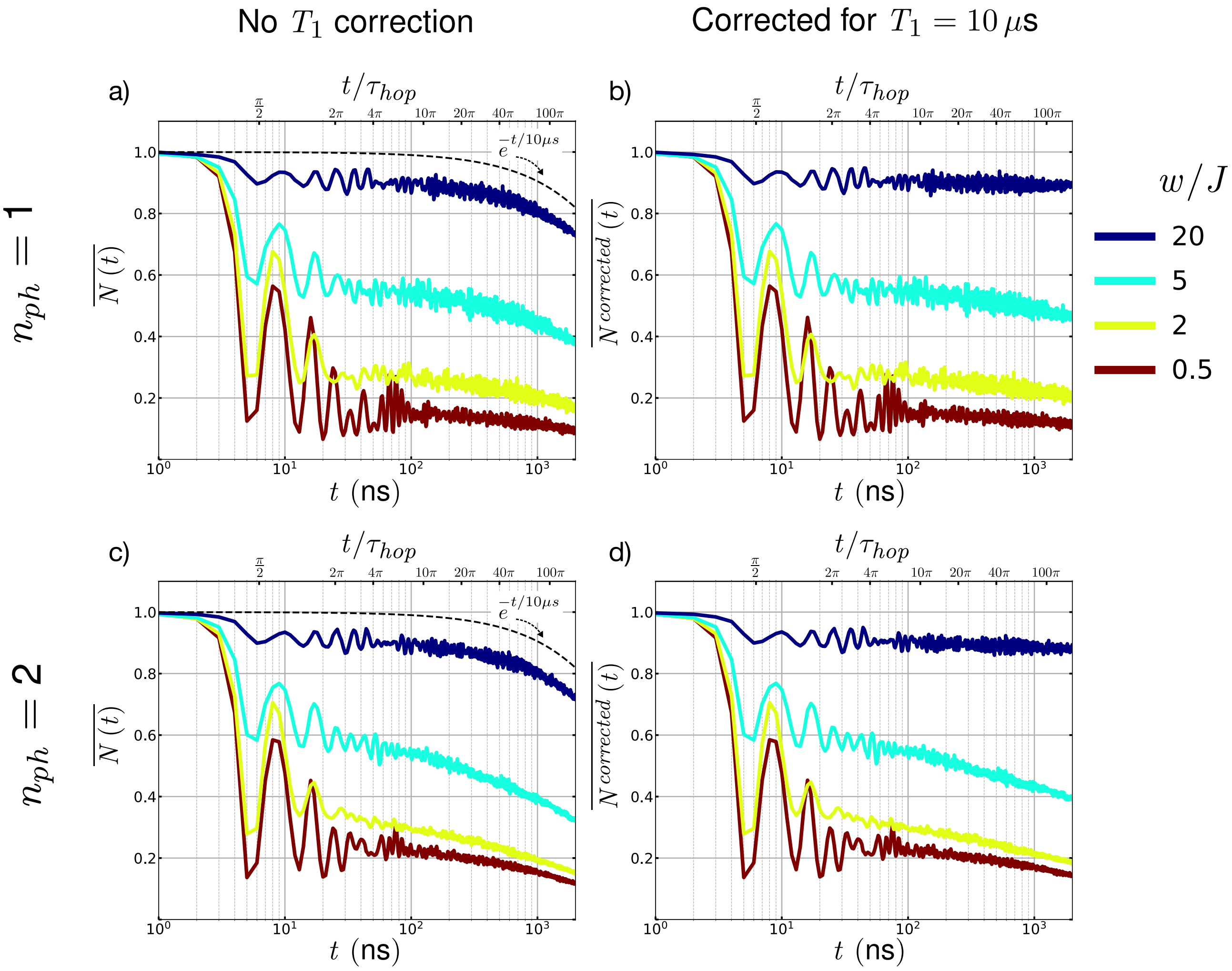

Figure C.5: Transport Measurements: Decoherence Effects. **(a)** The raw disorder averaged transport data for $n_{ph} = 1$ **(b)** The data from (a) corrected for a simple energy relaxation model $\overline{N^{corrected}(t)} = \overline{N(t)}/e^{(-t/10\mu s)}$. **(c)** The raw disorder averaged transport data for $n_{ph} = 2$. **(d)** The disorder averaged transport data with T_1 correction.

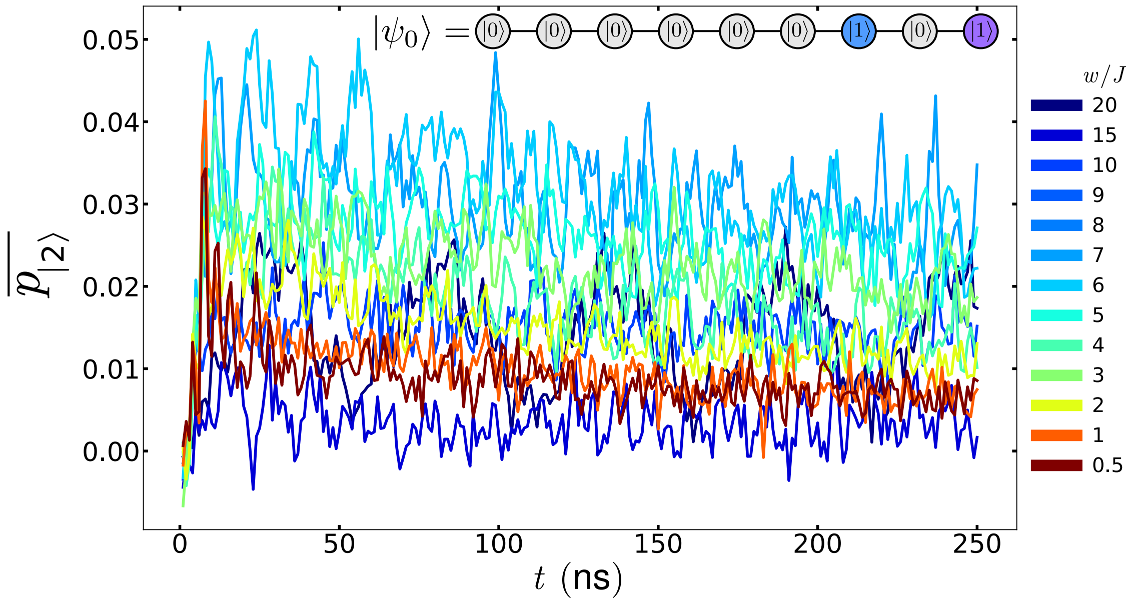

Figure C.6: Transport Measurements: Two state occupation.

C.3 Interferometric protocols, Figs. C.7-C.10

In order to gain some insights about the echo sequences, we first consider the case of very strong disorder, where the local integrals of motion (LIOMs) τ_i^z are close to the physical spins S_i^z (represented by the two lowest energy levels of a qubit), and assume that we directly manipulate LIOMs. First, we will consider the spin echo sequence illustrated graphically in Fig. C.7 [110]. Assuming we start from the vacuum state $|\psi_0\rangle = |0\rangle \otimes |\{\tau_j\}\rangle$, we initiate the dynamics by applying a $\pi/2$ pulse:

$$|\psi\rangle = \frac{1}{\sqrt{2}}(|0\rangle + i\,|1\rangle) \otimes |\{\tau_j\}\rangle \tag{C.1}$$

When the system evolves for times $t/2$, the spin at site i experiences an effective magnetic field, that depends on the states of the other LIOMs, see Eq. (2) in the main text,

$$\varDelta_i = \tilde{h}_i + \sum_j J_{ij}\tau_j^z + \sum_{j,k} J_{ijk}\tau_j^z\tau_k^z + \dots . \tag{C.2}$$

C.3.1 Echo pulse sequences

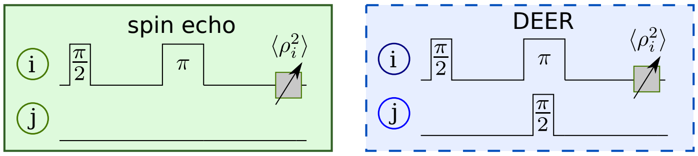

Figure C.7: Pulse sequence schematics for spin and DEER echo. DEER echo differs from spin echo by the addition of a remote $\pi/2$ pulse simultaneous with the spin echo π pulse between the free precession intervals.

The π rotation halfway through the spin-echo sequence then inverts the effective magnetic field $\mathit{\Delta}_i \to -\mathit{\Delta}_i$ which is precisely canceled after another time evolution for $t/2$. At the end of the protocol we measure the purity, which is advantageous over measuring a single spin component, because it is less prone to running field gradients and external perturbations. For the spin-echo sequence on the LIOMs we find a perfect purity of one. In a true measurement on our device the echo is performed on the physical spins, which possess a finite operator overlap with the LIOMs which is less than one. This leads to a spin echo signal that saturates to a finite value that decreases with decreasing disorder strength [110].

In the DEER echo sequence we similarly perform a spin echo measurement on site i as before, However, half-way through the time evolution we modify a second part of the system, say site j by applying a $\pi/2$ pulse, see Fig. S7. The effective magnetic field for the backward evolution $\tilde{\mathit{\Delta}}_i$, deviates from the field $\mathit{\Delta}_i$ of the forward evolution in all the terms containing τ_j^z. In summary, the state after the second time evolution is therefore

$$\begin{aligned} |\psi_D(t)\rangle = \frac{1}{2}[\,|1\rangle \otimes |...0_j...\rangle + e^{i(\mathit{\Delta}_i - \tilde{\mathit{\Delta}}_i)t - i\mathit{\Delta}_j t}\,|1\rangle \otimes |...1_j...\rangle - \\ |0\rangle \otimes |...0_j...\rangle - e^{-i(\mathit{\Delta}_i - \tilde{\mathit{\Delta}}_i)t - i\mathit{\Delta}_j t}\,|0\rangle \otimes |...1_j...\rangle] \end{aligned} \tag{C.3}$$

and the measurement of the purity then yields

$$\mathrm{tr}\left(\rho^2\right) = \cos^2\left[\left(\mathit{\Delta}_i - \tilde{\mathit{\Delta}}_i\right)t\right]. \tag{C.4}$$

Due to the interaction between the τ bits at site i and j, the phases do not cancel anymore and the signal decays. The difference between spin and DEER echo is thus a pure interaction effect which would not appear in the noninteracting localized phase. The advantage of performing a differential measurement of the two echo protocols is that even in the presence of noise, deviations of the two echo signals, demonstrates a clear interaction effect and hence is able to unambiguously measure the interacting character of the LIOMs. Because these interaction effects are due to the local occupation of higher orbitals we numerically estimate the population of multiply excited states $n_i^{max} = 1, 2$ during the DEER echo protocol for a evolution time of $t = 63\,\mathrm{ns}$ in Fig. C.8.

In the experimental measurement of the purity, local occupations higher than two are not taken into account. This leads to a leakage of the measurement as characterized by the finite value of $\langle \sigma_i^z \rangle$ in Fig. 3 (b) of the main text. Moreover, we numerically estimate this effect by resolving the probabilities for maximum local occupations $n_i^{max} = 1, 2$ during the DEER echo protocol for a evolution time of $t = 63\,\mathrm{ns}$ in Fig. C.8. From that it can be deduced that leakage effects are not severe, and in particular does not change the qualitative difference between the spin echo and DEER echo protocols.

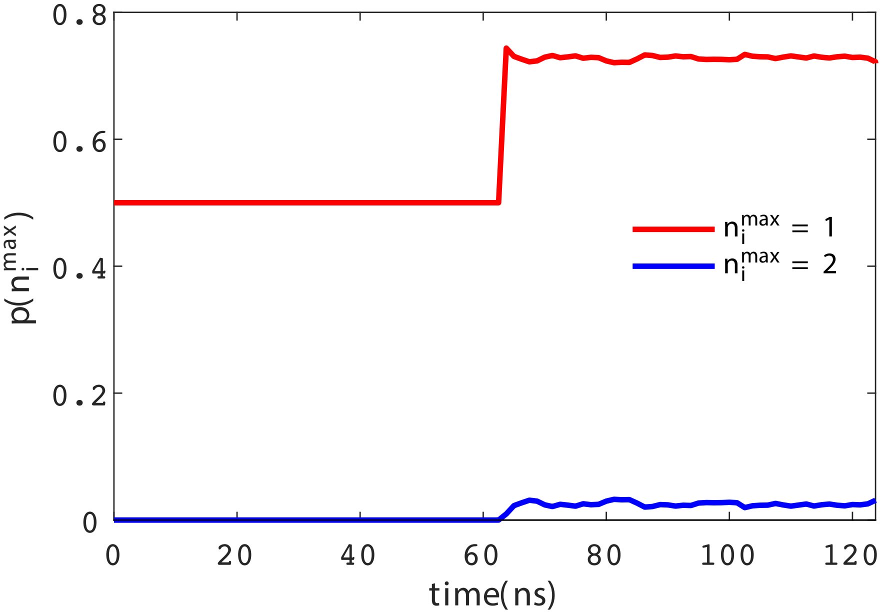

Figure C.8: Numerical estimate of the occupation of higher transmon levels during the DEER echo protocol. Calculation shown here for for the one, and two excitation states

C.3.2 Maximum local occupation

Probability for maximum local occupations of $n_i^{max} = 1, 2$ during the DEER echo protocol for $L = 9$ sites, an evolution time of $T = 63$ns, coupling $J = 2\pi \cdot 40$MHz, disorder strength $w/J = 10$ and interaction $U/J = 4$.

C.3.3 Comparison with numerics for echo experiments

In Fig. C.9 we compare the data from the interferometric pulse sequences presented in Fig. 5.3 of the main text with numeric predictions. In panels (a) and (b) we compare the onsite population at the spin echo qubit. Although there is a strong correspondence, we observe greater diffusion off site (larger σ^z)) in the experiment than in the numerics. There is also less contrast in the experiment than in the numerics. It is likely that these differences are related to the transient pulse response of our system and open systems effects, however further investigation is needed to make a conclusive determination.

C.3.4 Extended data

In Fig. C.10 we show extended data for echo sequence measurements for several values of of the disorder parameter w with J held fixed at 40 MHz. Compared with Fig. 3 of the main text, the initial state for these measurements had an additional excitation at the indicated position (purple). We observe a strong interferometric

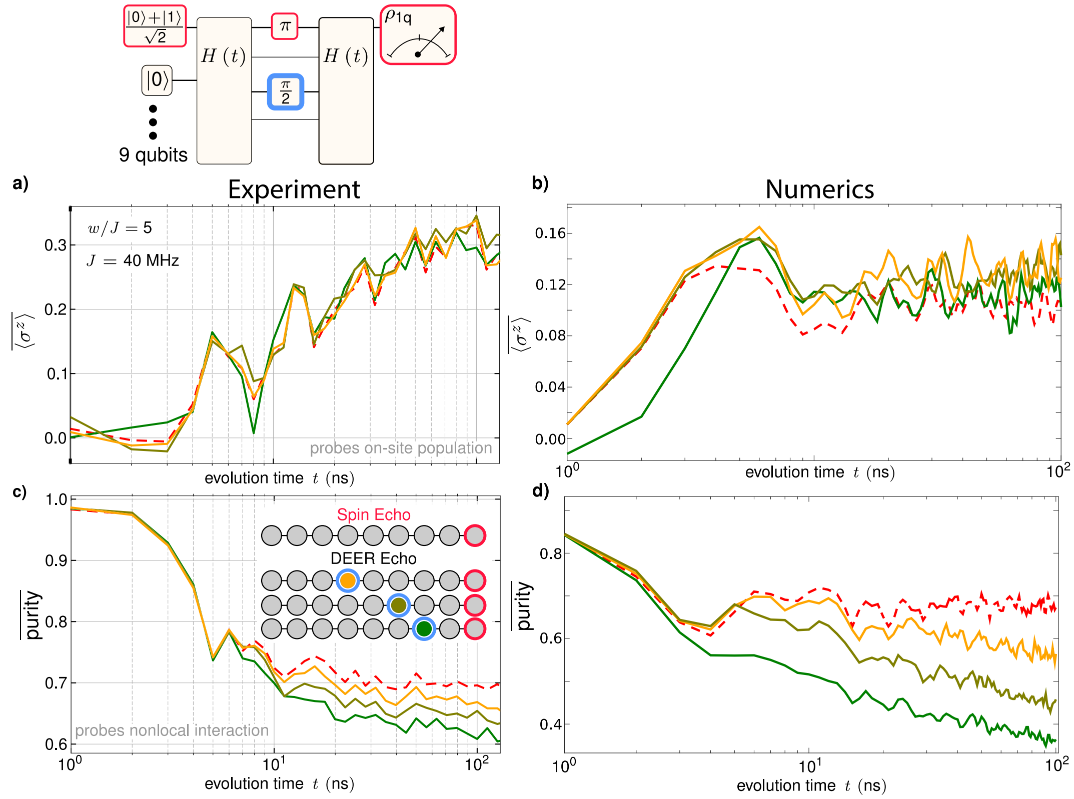

Figure C.9: Comparison with numerics for echo experiments. **(a)** and **(b)** Disorder averaged expectation value of σ^z showing population at the observation site for experimental observations and numerical prediction. The lack of dependence of $\overline{\langle\sigma^z\rangle}$ on the DEER pulse indicates localization in our system. **(c)** and **(d)** Disorder averaged purity of the reduced single qubit density matrix at the observation site. The contrast between spin-echo and DEER echo demonstrates that the local phase accumulation is conditional on the remote population. This is a direct measure of the nonlocal interaction strength.

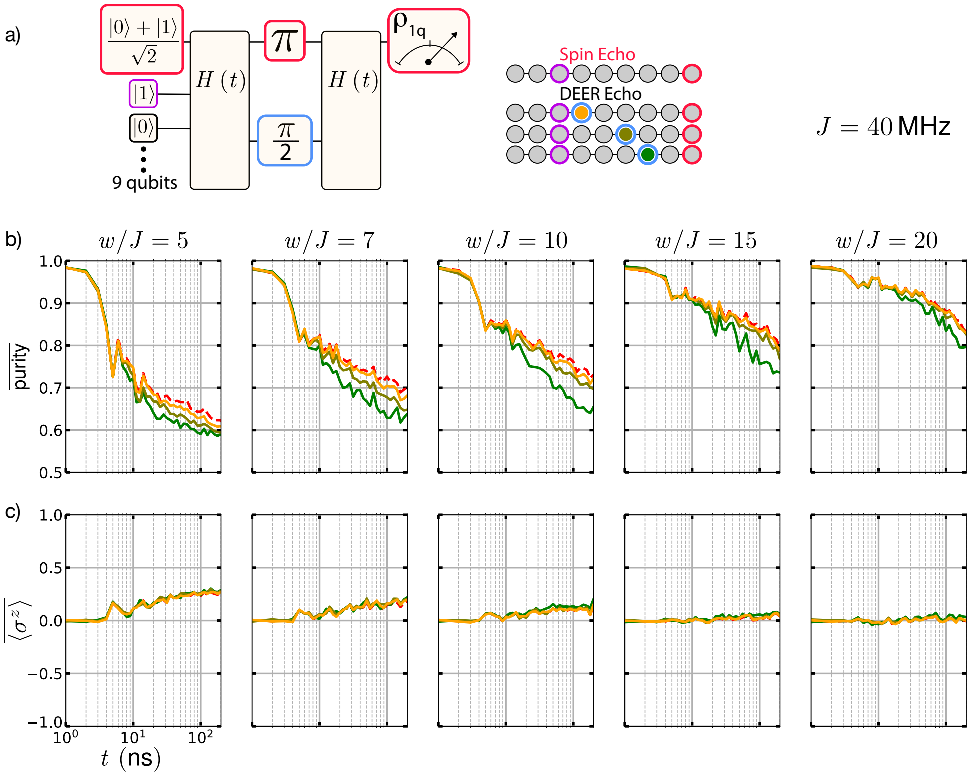

Figure C.10: Interferometric Protocols: Extended Data. **(a)** Spin and DEER echo pulse sequences. We the blue outline indicates the position of the DEER echo pulse, and the position of an additional excitation is indicated in purple. **(b)** purity of the single qubit density matrix after the spin echo (dashed red lines) and DEER echo (solid lines) experiments. **(c)** $\langle\sigma^z\rangle$ monitored over the echo experiments.

signature in the purity, indicating nonlocal interaction. In these measurements σ^z does not depend on the position of the echo pulses, indicating localization.

C.4 Entanglement measures

The distillable entanglement of the two qubit density matrix $E_D(\rho_{2q})$ is lower bounded by the coherent information entropy

$$E_D(\rho_{2q}) \geq S(\rho_{1q}) - S(\rho_{2q}), \tag{C.5}$$

where $\rho_{1q,2q}$ are the reduced density matrices of one of the two qubits and the two qubit subsystem, respectively, and $S(\rho)$ is the von Neumann entanglement entropy. An upper bound to the distillable entanglement is provided by the logarithmic negativity[131] which is defined as

$$E_N(\rho_2) = \log_2 ||\rho_2^{T_A}||_1. \tag{C.6}$$

Here, $\rho_2^{T_A}$ is the partial transpose of the reduced density matrix with respect to one of the qubits and $||\cdot||_1$ denotes the trace norm.

A second operational entanglement measure is the entanglement of formation, which is a measure for the entanglement needed to create a given entangled state.It is defined as

$$E_F(\rho) = \epsilon(\mathcal{C}(\rho)) \tag{C.7}$$

with

$$\epsilon(x) = -h_+(x)\log_2 h_+(x) - h_-(x)\log_2 h_-(x) \tag{C.8}$$

where

$$h_\pm(x) = -\frac{1}{2}\left(1 \pm \sqrt{1-x^2}\right). \tag{C.9}$$

The concurrence $\mathcal{C}(\rho)$ of a mixed state of two qubits is defined as

$$\mathcal{C}(\rho) = \max\left(0, \lambda_1 - \lambda_2 - \lambda_3 - \lambda_4\right), \tag{C.10}$$

where λ_i are the eigenvalues of

$$R = \sqrt{\sqrt{\rho}\tilde{\rho}\sqrt{\rho}} \tag{C.11}$$

and

$$\tilde{\rho} = (\sigma_y \otimes \sigma_y)\rho^*(\sigma_y \otimes \sigma_y). \tag{C.12}$$

C.5 Density matrix evolution numerics comparison, Figs. C.11 - C.15

In the main text we observe the entropy accumulation of an x-polarized subsystem in an MBL environment. The von Neumann entropy represents contributions from entanglement within the 9 qubit system, as well as from open system effects. In Figs. C.11-C.15 we provide supporting information to assist the reader in estimating the role of open systems effects in our experiment. We find that a good estimate of the contribution to the von Neumann entropy coming from coupling to the open system is provided by the entropy of the $J = 0$ curve. In the $J = 0$ case we do not expect interaction with the environmental qubits and attribute observed entropy in that case to extrinsic dephasing and relaxation processes.

C.5.5 Long time numerics for superposition initial state.

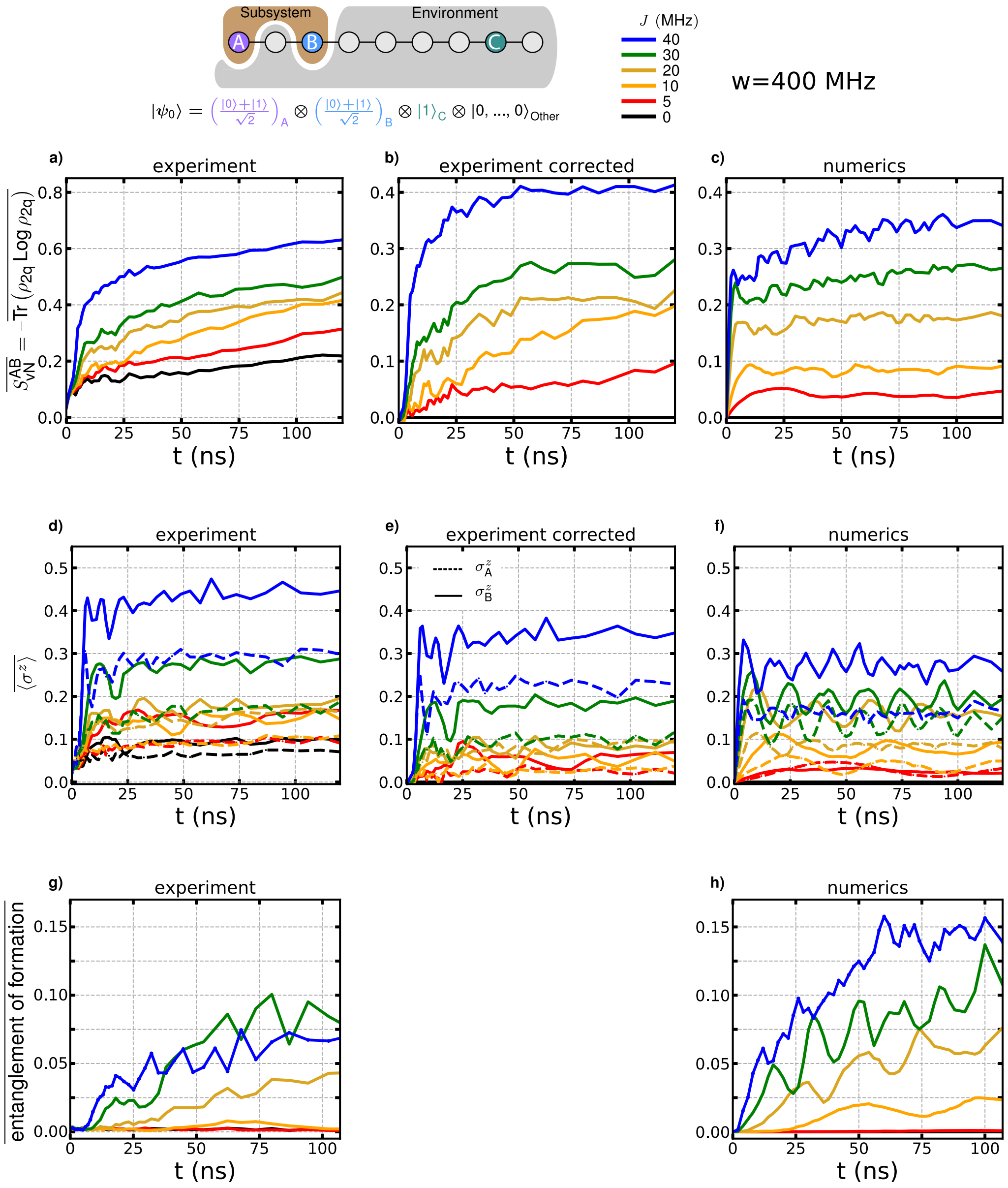

Figure C.11: Entropy Comparison with Numerics **(a)** Raw experimental observations from the two qubit density matrix measurements. The $J = 0$ data acts as a control experiment. We attribute entropy accumulation in the control experiment to open system effects **(b)** Experimental data after subtracting the baseline entropy measured in the control experiment from each of the data series. **(c)** Result of exact diagonalization numerics. **(d)** Raw experimental observation of σ^z, quantifying population. For the $J = 0$ baseline case we attribute the non-zero σ^z to state initialization error, and relaxation processes T1. **(e)** Experimental data corrected by subtracting the value of σ^z in the $J = 0$ control experiment from each of the data series. **(c)** Prediciton from exact diagonalization numerics. **(g)** Entanglement of formation as observed in the experiment. This is an affirmative observation of quantum correlation between sites A and B which cannot be attributed to open system effects, in contrast to the von Neumann entropy. The EOF observed in the experiment is slightly damped due to open system effects.

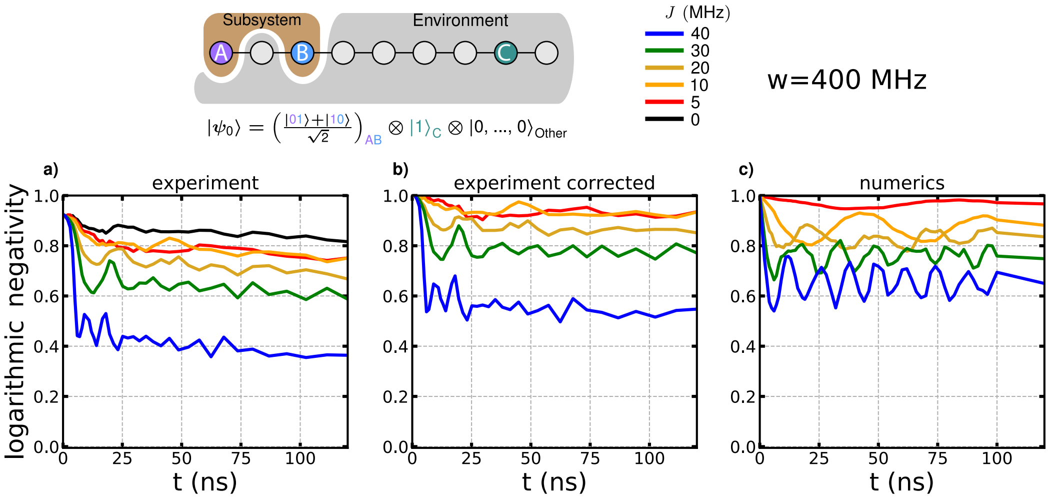

Figure C.12: entropy comparison with numerics **(a)** logarithmic negativity as observed in the experiment. the black $J = 0$ curve is our control experiment, and departure of the logarithmic negativity from 1 is attributed to state initialization error and open systems effects. **(b)** experimental data corrected for the loss of correlation observed in the $J = 0$ case. The correction was performed by adding (1 - logarithmic negativity($J = 0$)) to each data series. **(c)** prediction from exact diagonalization numerics.

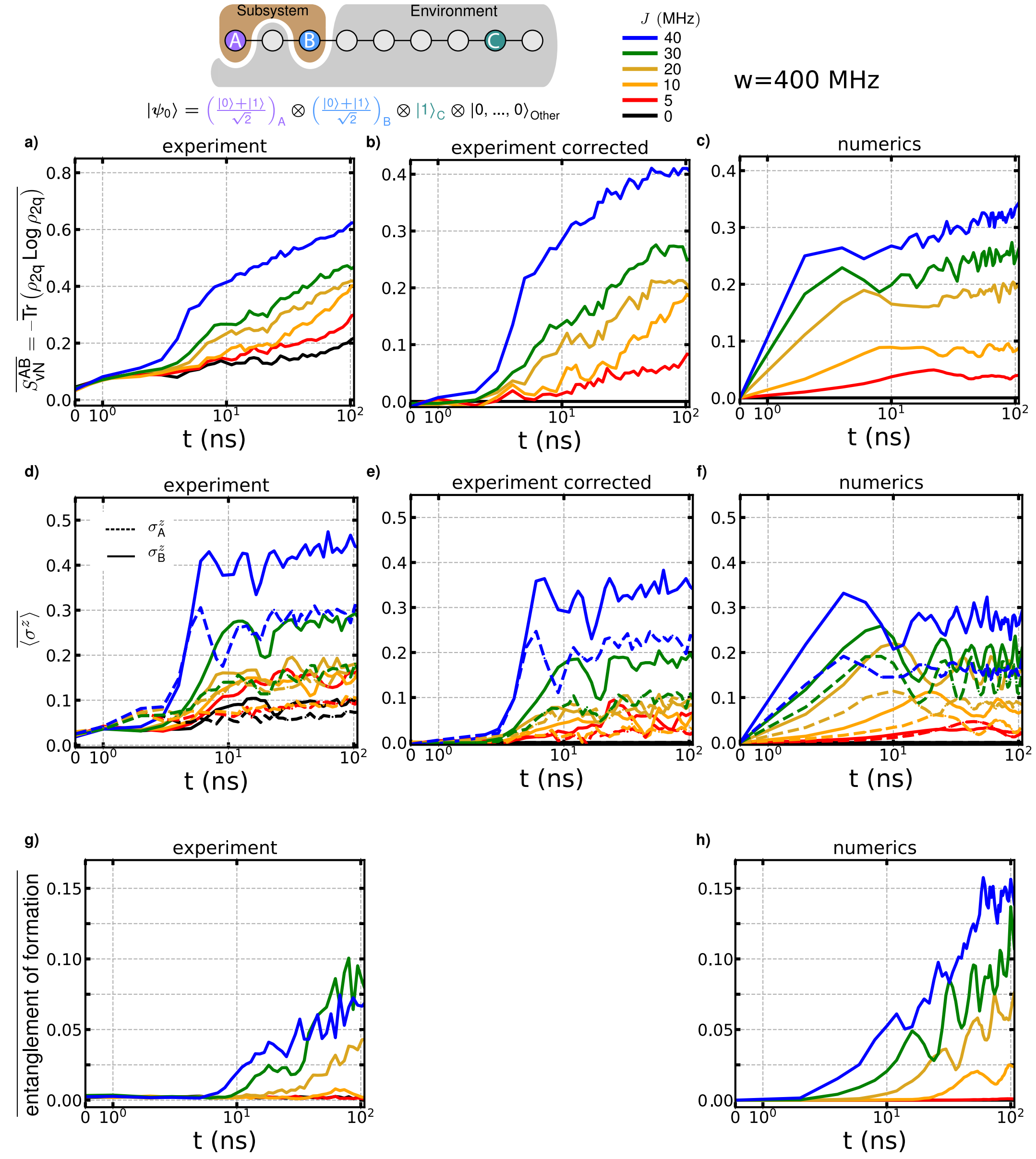

Figure C.13: Data from Fig. C.11 plotted on semi-log axes to emphasize scaling. The disagreement at short times is attributed to the transient respose of the control pulses.

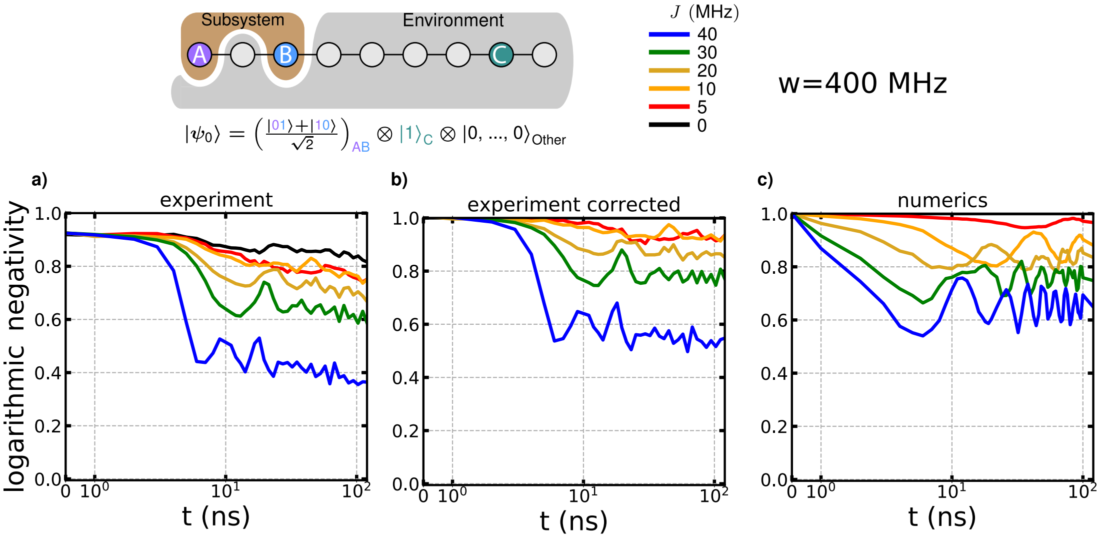

Figure C.14: Data from Fig. C.12 plotted on semi-log axes to emphasize scaling. The disagreement at short times is attributed to the transient respose of the control pulses.

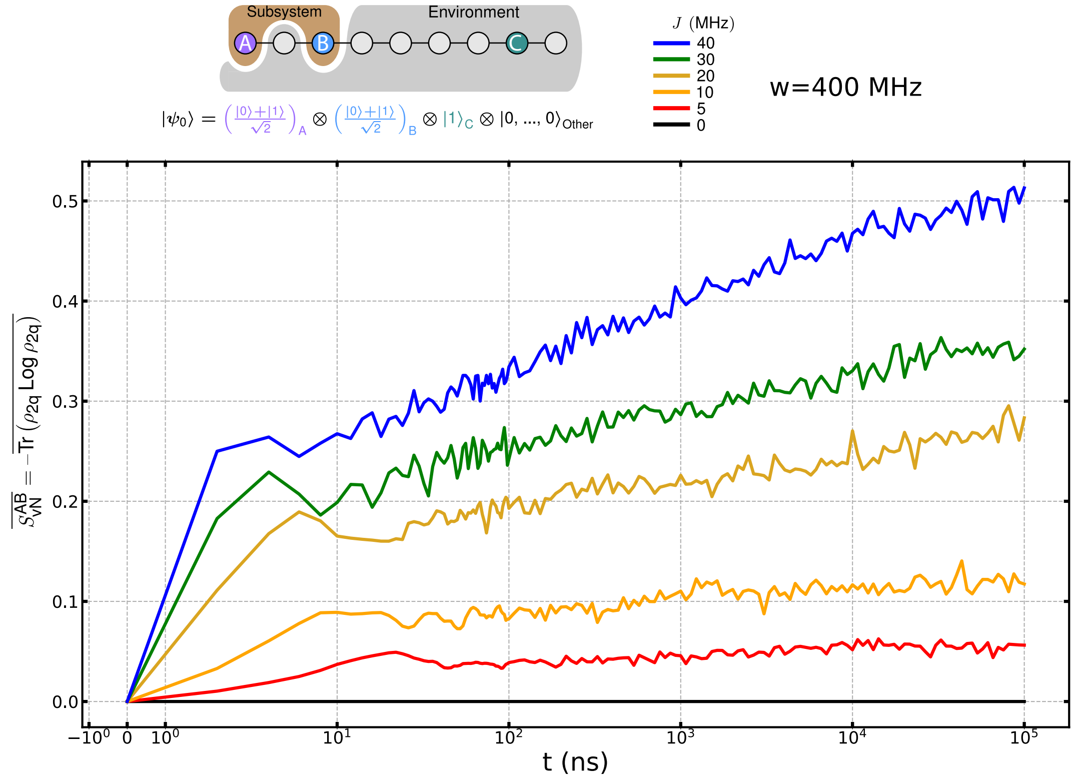

Figure C.15: Entropy comparison with numerics. Numerics to longer times than are accessible in the experiment illustrating the predicted logarithmic growth of entanglement for our system.

C.6 Sensitivity to nonlinearity U, Figs. C.16-C.18

The Hamiltonian parameter U varies weakly as a function of the qubit frequencies and inter-qubit coupling. U cannot be controlled independently in our system. Here we provide numerical evidence that the dynamics that we report in the MBL regime are not sensitive to this parameter.

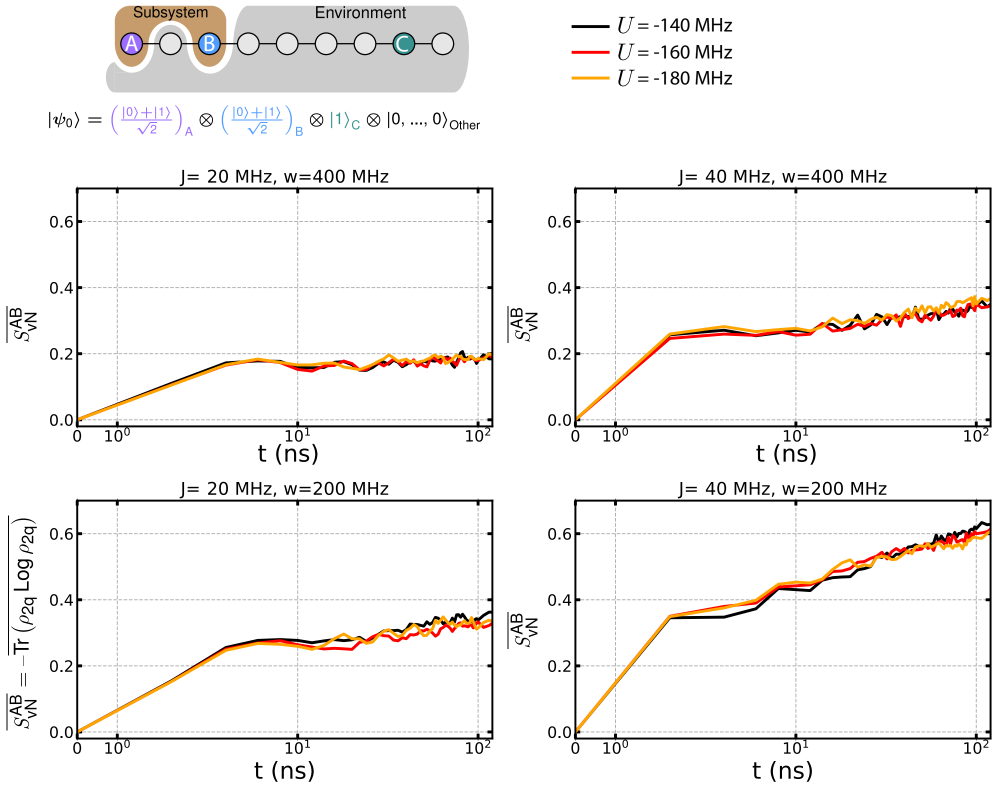

Figure C.16: Disorder averaged von Neumann entropy vs. U for selected couplings and disorder magnitudes. The von Neumann entropy observed in the experiment is predicted to be insensitive to the precise value of U.

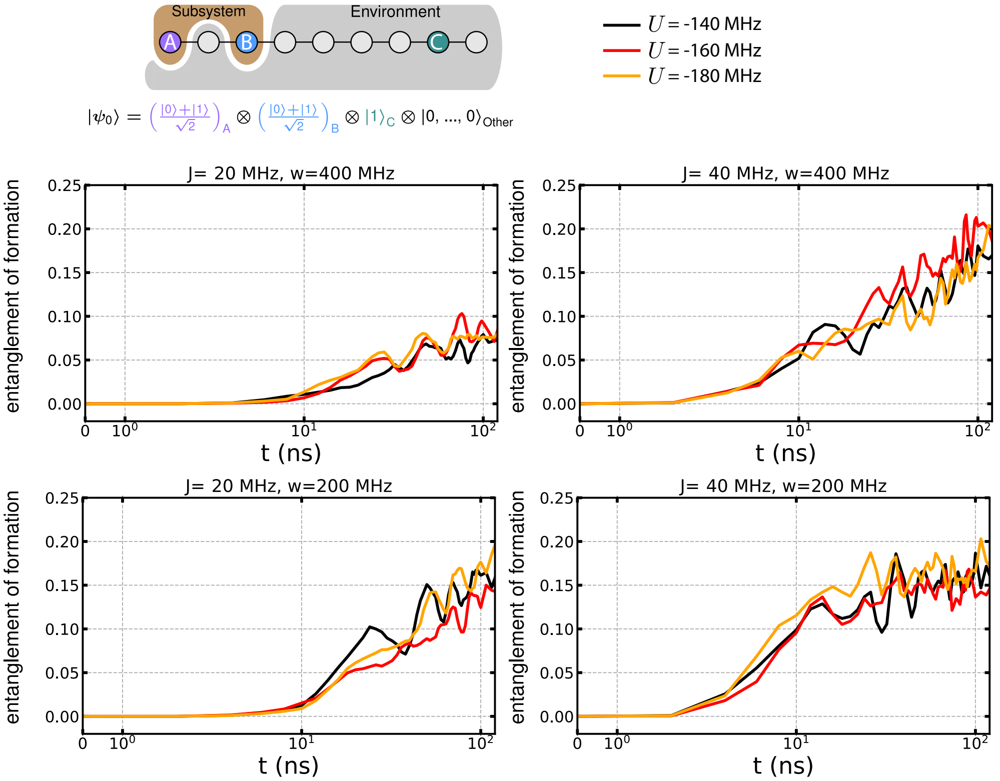

Figure C.17: Disorder averaged entanglement of formation vs. U for selected couplings and disorder magnitudes. The entanglement of formation observed in the experiment is predicted to be insensitive to the precise value of U.

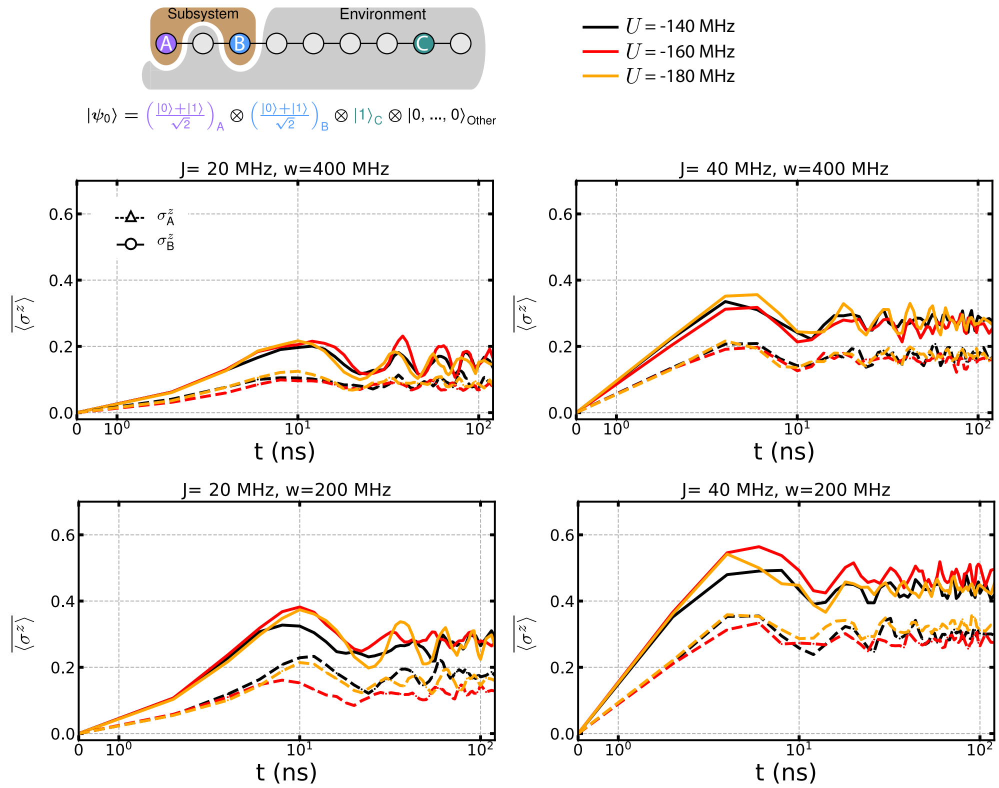

Figure C.18: $\overline{\langle\sigma^z\rangle}$ vs. U for selected couplings and disorder magnitudes. The onsite population observed in the experiment is predicted to be insensitive to the precise value of U.

C.7 Extended data for 1D qubit array, Fig. C.19

C.7.1 Distillable entanglement in MBL and diffusive regimes

In a 1D system we investigate the formation and preservation of entanglement between two qubits A and B that are embedded in a many-body localized environment as illustrated in Fig. S19 (a) and contrast this behavior with a system in the diffusive regime. The entanglement of formation quantifies the amount of entanglement directly between qubits A and B that would be required to produce the observed two-qubit mixed state density matrix.In panel (b), we initialize the sub-system into an unentangled product state of single qubit superpositions and observe the development of entanglement between our sub-system qubits. At high disorder, associated with the localized phase, entanglement grows continuously between the spatially separated sites. At low disorder, corresponding with the ergodic phase, we observe brief intervals of significant entanglement as the excitations delocalize across the full 9 qubit system. However, this behavior is quickly damped as the excitations are absorbed by environmental qubits, as the full 9-qubit system thermalizes.

Systems in the MBL and diffusive regimes also differ in their ability to retain correlation between their constituent parts. This is illustrated in Fig. C.19 (B) where we prepare a distant Bell state between the first and the third qubit and study the entanglement dynamics. While dephasing between LIOMs will ultimately destroy the entanglement, it will only due so on exponentially long times due to the localization. Crucially, the subsystem is in a mixed state, because it is coupling to the other 7 qubits of our device. We therefore characterize the entanglement of the 2-body mixed density matrix $\rho_{2q}(t)$ using an operational entanglement measure. In particular, we focus on the distillable entanglement, i.e., the entanglement which can be extracted from the mixed density matrix, that is upper bounded by logarithmic negativity entropy and lower bounded by the coherent information entropy. These bounds are shown in panel (c). For weak disorder (red), the prepared quantum information is immediately lost because the quantum dynamics entangles the subsystem with its environment and a featureless high temperature state is attained locally. This behavior can also be understood in terms of the monogamy of entanglement.[125] Although the two qubit subsystem is initially prepared in a maximally entangled state the degree of quantum correlation between subsystem sites decreases as the subsystem exchanges information with the environment and entangles with it. This monogamic principle also explains the damping of the peak in the low disorder data of panel (b). However, for strong disorder (blue) the distillable entanglement is sizable over long times, and hence the density matrix can be used as quantum resource. This is exemplified in panel (d) which shows the tomographic reconstruction of the two qubit density matrix for a single disorder instance as it evolves in time. These results show that a many-body localized system can efficiently retain quantum information over long time scales.

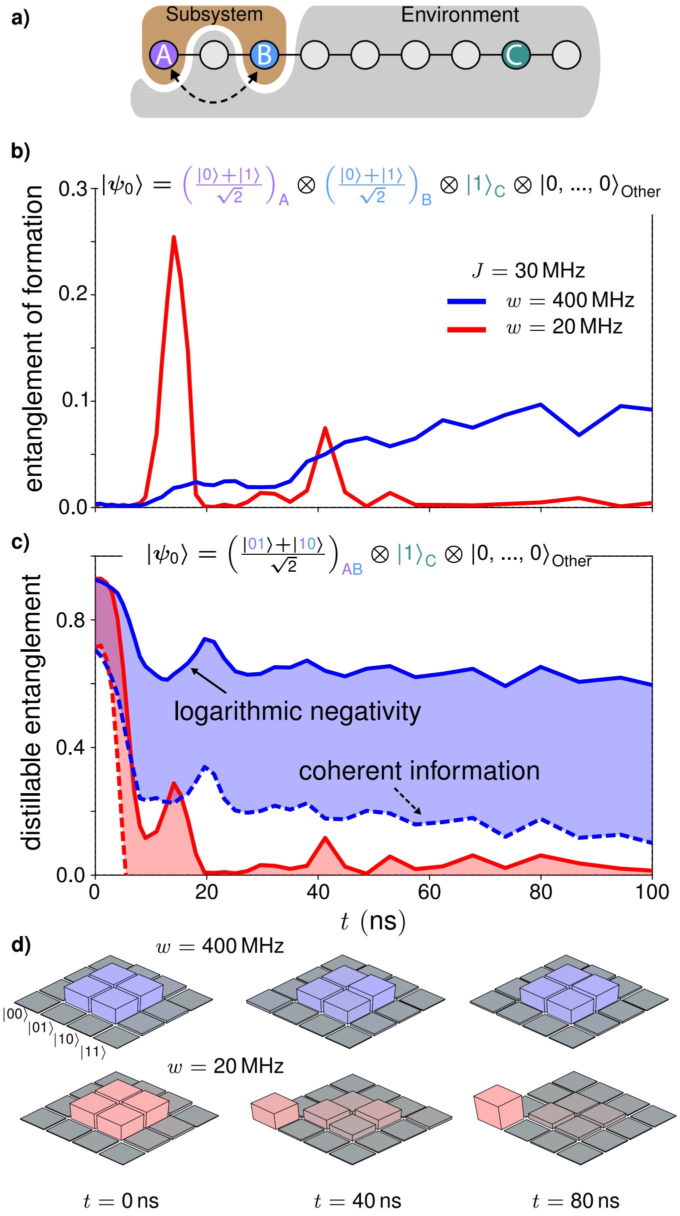

Figure C.19: Entanglement of formation and distillable entanglement in MBL and diffusive regimes **(a)** Schematic diagram emphasizing our focus on the entanglement between qubits A and B which are embedded in an environment. **(b)** To observe the development of entanglement between sites A and B the sub-system is initialized in a product of single qubit superposition states and the entanglement of formation of the two qubit density matrix is extracted. **(c)** We demonstrate the capability of the MBL phase to preserve entanglement initializing the sub-system into a maximally entangled Bell pair and observing the decay of quantum correlations. We extract the logarithmic negativity and coherent information from measurements of the two-qubit sub-system density matrix. These provide, respectively, upper and lower bounds on the distillable entanglement within the sub-system. **(d)** Representative density matrices from single disorder instances contained in **(c)** at high and low disorder.

C.8 Extended data for 2D qubit arrays, Fig. C.20

C.8.1 Onsite population for 2D qubit arrays

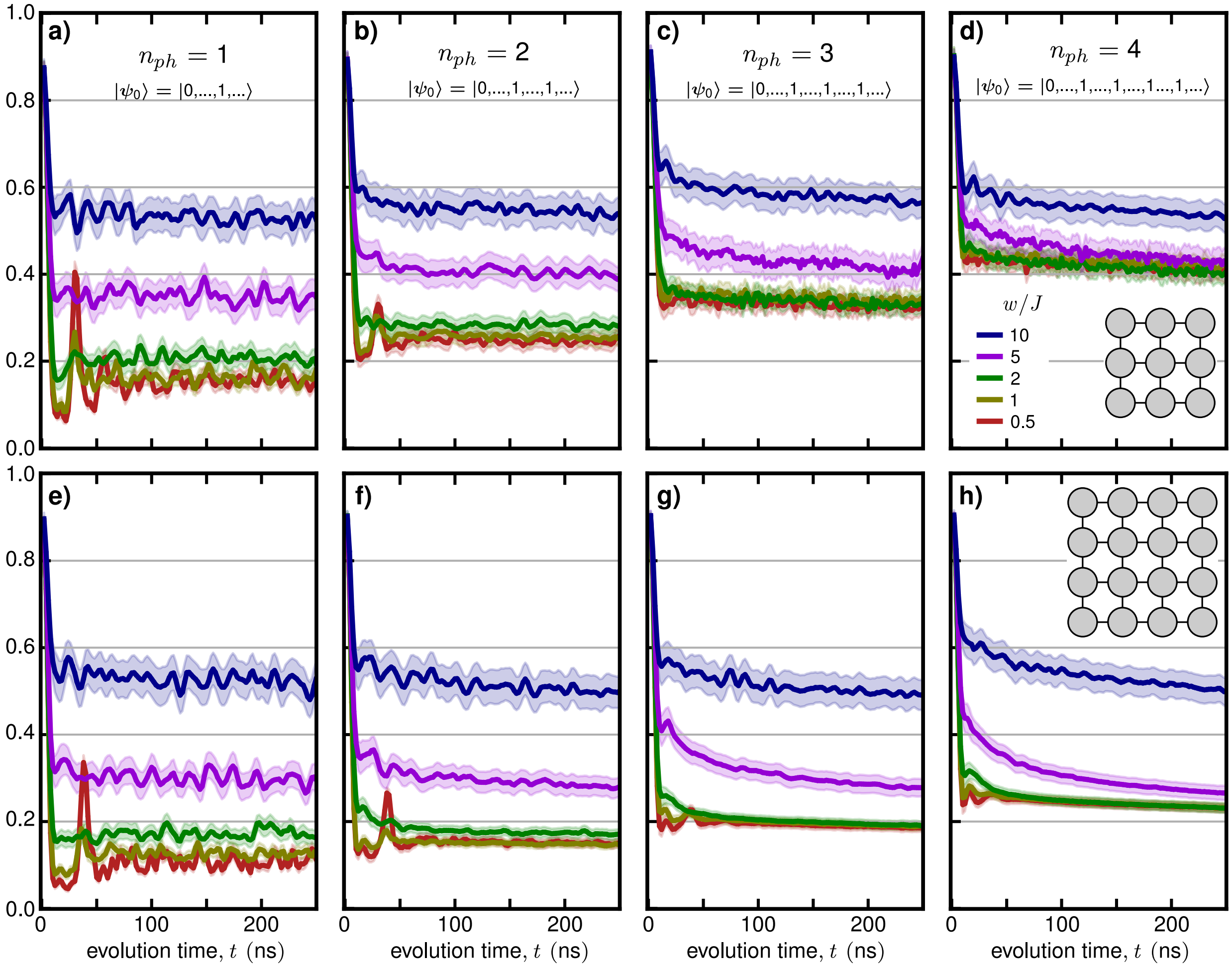

Figure C.20: Extended data for onsite population of 2D arrays. (a-d) Onsite population for $n_{ph} = 1, 2, 3, 4$ on a 3x3 array of qubits. **(e-h)** Onsite population for $n_{ph} = 1, 2, 3, 4$ on a 4x4 array of qubits.

In Fig. C.20, we show extended data for the onsite population for 2D geometries, for $n_{ph} = 1, 2, 3, 4$. The initial location of the excitations was randomized between runs but the observation site was always one of the initially excited qubits. Similar to the 1D geometries, with sufficient disorder the onsite population takes a non-thermal stationary value and is consistent with many-body localization. In the 2D geometries the onsite population consistent with thermalization at higher disorders when there are more photons in the system (greater n_{ph}), as in the 1D case.

Bibliography

1. Schrödinger, E. An Undulatory Theory of the Mechanics of Atoms and Molecules. *Phys. Rev.* **28,** 1049–1070. https://link.aps.org/doi/10.1103/PhysRev.28.1049 (6 Dec. 1926).
2. Feynman, R. P. Simulating physics with computers. *International Journal of Theoretical Physics* **21,** 467–488. ISSN: 1572-9575. https://doi.org/10.1007/BF02650179 (June 1982).
3. Leggett, A. Macroscopic Quantum Systems and the Quanatum Theory of Measurement. *Supplement on the Progress of Theoretical Physics* **69** (1980).
4. Martinis, J. M., Devoret, M. H. & Clarke, J. Energy-Level Quantization in the Zero-Voltage State of a Current-Biased Josephson Junction. *Phys. Rev. Lett.* **55,** 1543–1546. https://link.aps.org/doi/10.1103/PhysRevLett.55.1543 (15 Oct. 1985).

5. Nakamura, Y., Pashkin, Y. A. & Tsai, J. S. Coherent control of macroscopic quantum states in a single-Cooper-pair box. *Nature* **398,** 786–788. `https://doi.org/10.1038/19718` (1999).

6. Arute, F. *et al.* Quantum supremacy using a programmable superconducting processor. *Nature* **574,** 505–510. `https://doi.org/10.1038/s41586-019-1666-5` (2019).

7. Martinis, J. M. *et al.* Decoherence in Josephson Qubits from Dielectric Loss. *Phys. Rev. Lett.* **95,** 210503. `https://link.aps.org/doi/10.1103/PhysRevLett.95.210503` (21 Nov. 2005).

8. Pozar, D. *Microwave Enginneering 3rd edition* ISBN: 0-47144878-8 (John Wiley & Sons, Inc., Hoboken , NJ, USA, 2005).

9. Gao, J. *The Physics of Superconducting Microwave Resonators* PhD thesis (California Institute of Technology, Pasadena, CA, 2008).

10. Barends, R. *Photon-detecting superconducting resonators* PhD thesis (TU Delft, Leiden, The Netherlands, 2009).

11. Mazin, B. *Microwave Kinetic Inductance Detectors* PhD thesis (California Institute of Technology, Pasadena, CA, 2004).

12. Sank, D. *Fast, Accurate State Measurement in Superconducting Qubits* PhD thesis (UC - Santa Barbara, Santa Barbara, CA, 2014).

13. Chen, Z. *Metrology of Quantum Control and Measurement in Superconducting Qubits* PhD thesis (UC - Santa Barbara, Santa Barbara, CA, 2018).

14. Neill, C. *A path towards quantum supremacy with superconducting qubits* PhD thesis (UC - Santa Barbara, Santa Barbara, CA, 2017).

15. Duzer, T. V. & Turner, C. W. *Principles of Superconductive Devices and Circuits, (Second Ed.)* ISBN: 0-13-262742-6 (Prentice Hall PTR, Upper Saddle River, NJ, USA, 1999).

16. Koch, J. *et al.* Charge-insensitive qubit design derived from the Cooper pair box. *Phys. Rev. A* **76,** 042319. `https://link.aps.org/doi/10.1103/PhysRevA.76.042319` (4 Oct. 2007).

17. Krantz, P. *et al.* A quantum engineers guide to superconducting qubits. *Applied Physics Reviews* **6,** 021318. ISSN: 1931-9401. `http://dx.doi.org/10.1063/1.5089550` (June 2019).

18. Roushan, P. Unpublished (2019).

19. Kher, A. *Superconducting Nonlinear Kinetic Inductance Devices* PhD thesis (CALIFORNIA INSTITUTE OF TECHNOLOGY, Pasadena, CA, 2016).

20. Megrant, A. *et al.* Planar superconducting resonators with internal quality factors above one million. *Applied Physics Letters* **100,** 113510. eprint: `https:`

//doi.org/10.1063/1.3693409. https://doi.org/10.1063/1.3693409 (2012).

21. Josephson, B. Possible new effects in superconductive tunnelling. *Physics Letters* **1,** 251–253. ISSN: 0031-9163. http://www.sciencedirect.com/science/article/pii/0031916362913690 (1962).

22. Ambegaokar, V. & Baratoff, A. Tunneling Between Superconductors. *Phys. Rev. Lett.* **10,** 486–489. https://link.aps.org/doi/10.1103/PhysRevLett.10.486 (11 June 1963).

23. Paik, H. *et al.* Observation of High Coherence in Josephson Junction Qubits Measured in a Three-Dimensional Circuit QED Architecture. *Phys. Rev. Lett.* **107,** 240501. https://link.aps.org/doi/10.1103/PhysRevLett.107.240501 (24 Dec. 2011).

24. Barends, R. *et al.* Coherent Josephson Qubit Suitable for Scalable Quantum Integrated Circuits. *Phys. Rev. Lett.* **111,** 080502. https://link.aps.org/doi/10.1103/PhysRevLett.111.080502 (8 Aug. 2013).

25. Chen, Y. *et al.* Qubit Architecture with High Coherence and Fast Tunable Coupling. *Phys. Rev. Lett.* **113,** 220502. https://link.aps.org/doi/10.1103/PhysRevLett.113.220502 (22 Nov. 2014).

26. Neill, C. *et al.* A blueprint for demonstrating quantum supremacy with superconducting qubits. *Science* **360,** 195–199. ISSN: 0036-8075. eprint: `https://science.sciencemag.org/content/360/6385/195.full.pdf`. https://science.sciencemag.org/content/360/6385/195 (2018).

27. Leduc, H. G. *et al.* Titanium nitride films for ultrasensitive microresonator detectors. *Applied Physics Letters* **97,** 102509. eprint: `https://doi.org/10.1063/1.3480420`. https://doi.org/10.1063/1.3480420 (2010).

28. Vissers, M. R. *et al.* Low loss superconducting titanium nitride coplanar waveguide resonators. *Applied Physics Letters* **97,** 232509. eprint: `https://doi.org/10.1063/1.3517252`. https://doi.org/10.1063/1.3517252 (2010).

29. Sage, J. M., Bolkhovsky, V., Oliver, W. D., Turek, B. & Welander, P. B. Study of loss in superconducting coplanar waveguide resonators. *Journal of Applied Physics* **109,** 063915. eprint: `https://doi.org/10.1063/1.3552890`. https://doi.org/10.1063/1.3552890 (2011).

30. Vissers, M. R., Kline, J. S., Gao, J., Wisbey, D. S. & Pappas, D. P. Reduced microwave loss in trenched superconducting coplanar waveguides. *Applied Physics Letters* **100,** 082602. eprint: `https://doi.org/10.1063/1.3683552`. https://doi.org/10.1063/1.3683552 (2012).

31. Diener, P., Leduc, H. G., Yates, S. J. C., Lankwarden, Y. J. Y. & Baselmans, J. J. A. Design and Testing of Kinetic Inductance Detectors Made of Titanium Nitride. *Journal of Low Temperature Physics* **167,** 305–310. ISSN: 1573-7357. https://doi.org/10.1007/s10909-012-0484-z (May 2012).

32. Mazin, B. A. *et al.* A superconducting focal plane array for ultraviolet, optical, and near-infrared astrophysics. *Opt. Express* **20,** 1503–1511. http://www.opticsexpress.org/abstract.cfm?URI=oe-20-2-1503 (Jan. 2012).

33. Cecil, T. *et al.* Kinetic Inductance Detectors for X-Ray Spectroscopy. *Physics Procedia* **37.** Proceedings of the 2nd International Conference on Technology and Instrumentation in Particle Physics (TIPP 2011), 697–702. ISSN: 1875-3892. http://www.sciencedirect.com/science/article/pii/S1875389212017609 (2012).

34. Noroozian, O., Day, P. K., Eom, B. H., Leduc, H. G. & Zmuidzinas, J. Crosstalk Reduction for Superconducting Microwave Resonator Arrays. *IEEE Transactions on Microwave Theory and Techniques* **60,** 1235–1243. ISSN: 0018-9480 (May 2012).

35. Calvo, M. *et al.* LEKIDs Developments for mm-Wave Astronomy. *Journal of Low Temperature Physics* **167,** 379–385. ISSN: 1573-7357. https://doi.org/10.1007/s10909-012-0553-3 (May 2012).

36. Ho Eom, B., Day, P. K., LeDuc, H. G. & Zmuidzinas, J. A wideband, low-noise superconducting amplifier with high dynamic range. *Nature Physics* **8.** `https://doi.org/10.1038/nphys2356` (July 2012).

37. Krockenberger, Y., Karimoto, S.-i., Yamamoto, H. & Semba, K. Coherent growth of superconducting TiN thin films by plasma enhanced molecular beam epitaxy. *Journal of Applied Physics* **112,** 083920. eprint: `https://doi.org/10.1063/1.4759019`. `https://doi.org/10.1063/1.4759019` (2012).

38. Driessen, E. F. C., Coumou, P. C. J. J., Tromp, R. R., de Visser, P. J. & Klapwijk, T. M. Strongly Disordered TiN and NbTiN *s*-Wave Superconductors Probed by Microwave Electrodynamics. *Phys. Rev. Lett.* **109,** 107003. `https://link.aps.org/doi/10.1103/PhysRevLett.109.107003` (10 Sept. 2012).

39. Kumar, N., McGinn, J. T., Pourrezaei, K., Lee, B. & Douglas, E. C. Transmission electron microscopy studies of brown and golden titanium nitride thin films as diffusion barriers in very large scale integrated circuits. *Journal of Vacuum Science & Technology A* **6,** 1602–1608. eprint: `https://doi.org/10.1116/1.575335`. `https://doi.org/10.1116/1.575335` (1988).

40. Mandl, M., Hoffmann, H. & Kucher, P. Diffusion barrier properties of Ti/TiN investigated by transmission electron microscopy. *Journal of Applied Physics* **68,** 2127–2132 (Oct. 1990).

41. Logothetidis, S., Meletis, E., Stergioudis, G. & Adjaottor, A. Room temperature oxidation behavior of TiN thin films. *Thin Solid Films* **338,** 304–313. ISSN: 0040-6090. http://www.sciencedirect.com/science/article/pii/S0040609098009754 (1999).

42. Chowdhury, R., Vispute, R. D., Jagannadham, K. & Narayan, J. Characteristics of titanium nitride films grown by pulsed laser deposition. *Journal of Materials Research* **11,** 1458–1469 (1996).

43. Chappé, J.-M. *et al.* Titanium oxynitride thin films sputter deposited by the reactive gas pulsing process. *Applied Surface Science* **253,** 5312–5316. ISSN: 0169-4332. http://www.sciencedirect.com/science/article/pii/S0169433206015273 (2007).

44. Radecka, M. *et al.* Chemical composition, crystallographic structure and impedance spectroscopy of titanium oxynitride TiNxOy thin films. *Solid State Ionics* **192.** Proceedings of the 17th International Conference on Solid State Ionics, 693–698. ISSN: 0167-2738. http://www.sciencedirect.com/science/article/pii/S0167273810004194 (2011).

45. Williams, D. S. *et al.* Nitrogen, oxygen, and argon incorporation during reactive sputter deposition of titanium nitride. *Journal of Vacuum Science & Technology B: Microelectronics Processing and Phenomena* **5,** 1723–1729. eprint:

https://avs.scitation.org/doi/pdf/10.1116/1.583654. https://avs.scitation.org/doi/abs/10.1116/1.583654 (1987).

46. Ahn, K., Wittmer, M. & Ting, C. Investigation of Tin films reactively sputtered using a sputter gun. *Thin Solid Films* **107** (1983).

47. Schiller, S., Beister, G. & Sieber, W. Reactive high rate D.C. sputtering: Deposition rate, stoichiometry and features of TiOx and TiNx films with respect to the target mode. *Thin Solid Films* **111,** 259–268. ISSN: 0040-6090. http://www.sciencedirect.com/science/article/pii/0040609084901470 (1984).

48. Johansson, B. O., Sundgren, J., Greene, J. E., Rockett, A. & Barnett, S. A. Growth and properties of single crystal TiN films deposited by reactive magnetron sputtering. *Journal of Vacuum Science & Technology A* **3,** 303–307. eprint: https://doi.org/10.1116/1.573255. https://doi.org/10.1116/1.573255 (1985).

49. Wriedt, H. A. & Murray, J. L. The N-Ti (Nitrogen-Titanium) system. *Bulletin of Alloy Phase Diagrams* **8,** 378–388. ISSN: 0197-0216. https://doi.org/10.1007/BF02869274 (Aug. 1987).

50. Vissers, M. R. *et al.* Characterization and in-situ monitoring of substoichiometric adjustable superconducting critical temperature titanium ni-

tride growth. *Thin Solid Films* **548,** 485–488. ISSN: 0040-6090. http://www.sciencedirect.com/science/article/pii/S0040609013012297 (2013).

51. Penilla, E. & Wang, J. Pressure and Temperature Effects on Stoichiometry and Microstructure of Nitrogen-rich TiN Thin Films Synthesized via Reactive Magnetron DC-sputtering. *J. Nanomaterials* **2008,** 29:1–29:9. ISSN: 1687-4110. https://doi.org/10.1155/2008/267161 (Jan. 2008).

52. Lu, J. & Lee, C. G. Numerical estimates for energy of sputtered target atoms and reflected Ar neutrals in sputter processes. *Vacuum* **86,** 1134–1140. ISSN: 0042-207X (2012).

53. Adjaottor, A., Meletis, E., Logothetidis, S., Alexandrou, I. & Kokkou, S. Effect of substrate bias on sputter-deposited TiCx, TiNy and TiCxNy thin films. *Surface and Coatings Technology* **76-77,** 142–148. ISSN: 0257-8972 (1995).

54. Thornton, J. A. & Hoffman, D. W. The influence of discharge current on the intrinsic stress in Mo films deposited using cylindrical and planar magnetron sputtering sources. *Journal of Vacuum Science & Technology A* **3,** 576–579. eprint: `https://doi.org/10.1116/1.572997` (1985).

55. Patsalas, P., Charitidis, C. & Logothetidis, S. The effect of substrate temperature and biasing on the mechanical properties and structure of sputtered titanium nitride thin films. *Surface and Coatings Technology* **125,** 335–340.

ISSN: 0257-8972. http://www.sciencedirect.com/science/article/pii/S0257897299006064 (2000).

56. Private communication with H. G. LeDuc and B. Bumble.

57. Sandberg, M. *et al.* Etch induced microwave losses in titanium nitride superconducting resonators. *Applied Physics Letters* **100,** 262605. eprint: `https://doi.org/10.1063/1.4729623`. https://doi.org/10.1063/1.4729623 (2012).

58. Barends, R. *et al.* Minimizing quasiparticle generation from stray infrared light in superconducting quantum circuits. *Applied Physics Letters* **99,** 113507. eprint: `https://doi.org/10.1063/1.3638063`. https://doi.org/10.1063/1.3638063 (2011).

59. Gao, J. *et al.* Experimental evidence for a surface distribution of two-level systems in superconducting lithographed microwave resonators. *Applied Physics Letters* **92,** 152505. eprint: `https://doi.org/10.1063/1.2906373`. https://doi.org/10.1063/1.2906373 (2008).

60. Day, P. K., LeDuc, H. G., Mazin, B. A., Vayonakis, A. & Zmuidzinas, J. A broadband superconducting detector suitable for use in large arrays. *Nature* **425,** 817–821. https://doi.org/10.1038/nature02037 (2003).

61. Mazin, B. A. *et al.* A superconducting focal plane array for ultraviolet, optical, and near-infrared astrophysics. *Opt. Express* **20,** 1503–1511. http://www.opticsexpress.org/abstract.cfm?URI=oe-20-2-1503 (Jan. 2012).

62. Mariantoni, M. *et al.* Photon shell game in three-resonator circuit quantum electrodynamics. *Nature Physics* **7,** 287 EP -. https://doi.org/10.1038/nphys1885 (Jan. 2011).

63. Barends, R. *et al.* Coherent Josephson Qubit Suitable for Scalable Quantum Integrated Circuits. *Phys. Rev. Lett.* **111,** 080502. https://link.aps.org/doi/10.1103/PhysRevLett.111.080502 (8 Aug. 2013).

64. Jeffrey, E. *et al.* Fast Accurate State Measurement with Superconducting Qubits. *Phys. Rev. Lett.* **112,** 190504. https://link.aps.org/doi/10.1103/PhysRevLett.112.190504 (19 May 2014).

65. Wang, C. *et al.* Surface participation and dielectric loss in superconducting qubits. *Applied Physics Letters* **107,** 162601. eprint: `https://doi.org/10.1063/1.4934486`. https://doi.org/10.1063/1.4934486 (2015).

66. Wisbey, D. S. *et al.* Effect of metal/substrate interfaces on radio-frequency loss in superconducting coplanar waveguides. *Journal of Applied Physics* **108,** 093918. eprint: `https://doi.org/10.1063/1.3499608`. https://doi.org/10.1063/1.3499608 (2010).

67. Song, C. *et al.* Microwave response of vortices in superconducting thin films of Re and Al. *Phys. Rev. B* **79,** 174512. https://link.aps.org/doi/10.1103/PhysRevB.79.174512 (17 May 2009).

68. Wang, C. *et al.* Measurement and control of quasiparticle dynamics in a superconducting qubit. *Nature Communications* **5,** 5836 EP -. https://doi.org/10.1038/ncomms6836 (Dec. 2014).

69. Nsanzineza, I. & Plourde, B. L. T. Trapping a Single Vortex and Reducing Quasiparticles in a Superconducting Resonator. *Phys. Rev. Lett.* **113,** 117002. https://link.aps.org/doi/10.1103/PhysRevLett.113.117002 (11 Sept. 2014).

70. Martinis, J. M. *et al.* Decoherence in Josephson Qubits from Dielectric Loss. *Phys. Rev. Lett.* **95,** 210503. https://link.aps.org/doi/10.1103/PhysRevLett.95.210503 (21 Nov. 2005).

71. Martinis, J. M., Ansmann, M. & Aumentado, J. Energy Decay in Superconducting Josephson-Junction Qubits from Nonequilibrium Quasiparticle Excitations. *Phys. Rev. Lett.* **103,** 097002. https://link.aps.org/doi/10.1103/PhysRevLett.103.097002 (9 Aug. 2009).

72. Gao, J. *et al.* Experimental evidence for a surface distribution of two-level systems in superconducting lithographed microwave resonators. *Applied Physics*

Letters **92,** 152505. eprint: `https://doi.org/10.1063/1.2906373`. https://doi.org/10.1063/1.2906373 (2008).

73. Graaf, S. E. d., Danilov, A. V., Adamyan, A., Bauch, T. & Kubatkin, S. E. Magnetic field resilient superconducting fractal resonators for coupling to free spins. *Journal of Applied Physics* **112,** 123905. eprint: `https://doi.org/10.1063/1.4769208`. https://doi.org/10.1063/1.4769208 (2012).

74. Song, C., DeFeo, M. P., Yu, K. & Plourde, B. L. T. Reducing microwave loss in superconducting resonators due to trapped vortices. *Applied Physics Letters* **95,** 232501. eprint: `https://doi.org/10.1063/1.3271523`. https://doi.org/10.1063/1.3271523 (2009).

75. Bothner, D., Gaber, T., Kemmler, M., Koelle, D. & Kleiner, R. Improving the performance of superconducting microwave resonators in magnetic fields. *Applied Physics Letters* **98,** 102504. eprint: `https://doi.org/10.1063/1.3560480`. https://doi.org/10.1063/1.3560480 (2011).

76. Bothner, D. *et al.* Reducing vortex losses in superconducting microwave resonators with microsphere patterned antidot arrays. *Applied Physics Letters* **100,** 012601. eprint: `https://doi.org/10.1063/1.3673869`. https://doi.org/10.1063/1.3673869 (2012).

77. Stan, G., Field, S. B. & Martinis, J. M. Critical Field for Complete Vortex Expulsion from Narrow Superconducting Strips. *Phys. Rev. Lett.* **92,** 097003. https://link.aps.org/doi/10.1103/PhysRevLett.92.097003 (9 Mar. 2004).

78. Tinkham, M. *Introduction to superconductivity* (2012).

79. Wenner, J. *et al.* Surface loss simulations of superconducting coplanar waveguide resonators. *Applied Physics Letters* **99,** 113513. eprint: `https://doi.org/10.1063/1.3637047`. https://doi.org/10.1063/1.3637047 (2011).

80. Megrant, A. *et al.* Planar superconducting resonators with internal quality factors above one million. *Applied Physics Letters* **100,** 113510. eprint: `https://doi.org/10.1063/1.3693409`. https://doi.org/10.1063/1.3693409 (2012).

81. Barends, R. *et al.* Minimizing quasiparticle generation from stray infrared light in superconducting quantum circuits. *Applied Physics Letters* **99,** 113507. eprint: `https://doi.org/10.1063/1.3638063`. https://doi.org/10.1063/1.3638063 (2011).

82. See supplementary material in the appendix.

83. Ohya, S. *et al.* Room temperature deposition of sputtered TiN films for superconducting coplanar waveguide resonators. *Superconductor Science and Technology* **27,** 015009 (Dec. 2013).

84. Bruno, A. *et al.* Reducing intrinsic loss in superconducting resonators by surface treatment and deep etching of silicon substrates. *Applied Physics Letters* **106,** 182601. eprint: `https://doi.org/10.1063/1.4919761`. `https://doi.org/10.1063/1.4919761` (2015).

85. Wang, H. *et al.* Improving the coherence time of superconducting coplanar resonators. *Applied Physics Letters* **95,** 233508. eprint: `https://doi.org/10.1063/1.3273372`. `https://doi.org/10.1063/1.3273372` (2009).

86. Faoro, L. & Ioffe, L. B. Internal Loss of Superconducting Resonators Induced by Interacting Two-Level Systems. *Phys. Rev. Lett.* **109,** 157005. `https://link.aps.org/doi/10.1103/PhysRevLett.109.157005` (15 Oct. 2012).

87. Faoro, L. & Ioffe, L. B. Interacting tunneling model for two-level systems in amorphous materials and its predictions for their dephasing and noise in superconducting microresonators. *Phys. Rev. B* **91,** 014201. `https://link.aps.org/doi/10.1103/PhysRevB.91.014201` (1 Jan. 2015).

88. Barends, R. *et al.* Minimal resonator loss for circuit quantum electrodynamics. *Applied Physics Letters* **97,** 023508. eprint: `https://doi.org/10.1063/1.3458705`. `https://doi.org/10.1063/1.3458705` (2010).

89. Anderson, P. W. Absence of Diffusion in Certain Random Lattices. *Phys. Rev.* **109,** 1492–1505. `https://link.aps.org/doi/10.1103/PhysRev.109.1492` (5 Mar. 1958).

90. Abrahams, E. 50 Years of Anderson Localization (2010).

91. Billy, J. *et al.* Direct observation of Anderson localization of matter waves in a controlled disorder. *Nature* **453,** 891 EP -. `https://doi.org/10.1038/nature07000` (June 2008).

92. Weaver, R. Anderson localization of ultrasound. *Wave Motion* **12,** 129–142. ISSN: 0165-2125. `http://www.sciencedirect.com/science/article/pii/0165212590900342` (1990).

93. Wiersma, D. S., Bartolini, P., Lagendijk, A. & Righini, R. Localization of light in a disordered medium. *Nature* **390,** 671–673. `https://doi.org/10.1038/37757` (1997).

94. Schwartz, T., Bartal, G., Fishman, S. & Segev, M. Transport and Anderson localization in disordered two-dimensional photonic lattices. *Nature* **446,** 52 EP -. `https://doi.org/10.1038/nature05623` (Mar. 2007).

95. Basko, D., Aleiner, I. & Altshuler, B. Metal-insulator transition in a weakly interacting many-electron system with localized single-particle states. *Annals of Physics* **321,** 1126–1205 (5 2006).

96. Gornyi, I., Mirlin, A. & Polyakov, D. Interacting Electrons in Disordered Wires: Anderson Localization and Low-T Transport. *Phys. Rev. Lett.* **95,** 206603. `http://link.aps.org/doi/10.1103/PhysRevLett.95.206603` (20 Nov. 2005).

97. Imbrie, J. Z. Diagonalization and Many-Body Localization for a Disordered Quantum Spin Chain. *Phys. Rev. Lett.* **117,** 027201. `https://link.aps.org/doi/10.1103/PhysRevLett.117.027201` (2 July 2016).

98. Schreiber, M. *et al.* Observation of many-body localization of interacting fermions in a quasirandom optical lattice. *Science,* 842–845 (349 2015).

99. Kondov, S. S., McGehee, W. R., Xu, W. & DeMarco, B. Disorder-Induced Localization in a Strongly Correlated Atomic Hubbard Gas. *Phys. Rev. Lett.* **114,** 083002. `http://link.aps.org/doi/10.1103/PhysRevLett.114.083002` (8 Feb. 2015).

100. Smith, J. *et al.* Many-body localization in a quantum simulator with programmable random disorder. *Nature Physics* **12,** 907 EP -. `https://doi.org/10.1038/nphys3783` (June 2016).

101. Choi, J. *et al.* Exploring the many-body localization transition in two dimensions. *Science* **352,** 1547–1552 (2016).

102. Bordia, P. *et al.* Probing Slow Relaxation and Many-Body Localization in Two-Dimensional Quasiperiodic Systems. *Phys. Rev. X* **7,** 041047 (2017).

103. Roushan, P. *et al.* Spectroscopic signatures of localization with interacting photons in superconducting qubits. *Science* **358,** 1175–1179. ISSN: 0036-8075. eprint: `https://science.sciencemag.org/content/358/6367/1175.full.pdf`. https://science.sciencemag.org/content/358/6367/1175 (2017).

104. Lukin, A. *et al.* Probing entanglement in a many-bodylocalized system. *Science* **364,** 256–260. ISSN: 0036-8075. eprint: `https://science.sciencemag.org/content/364/6437/256.full.pdf`. https://science.sciencemag.org/content/364/6437/256 (2019).

105. Oganesyan, V. & Huse, D. A. Localization of interacting fermions at high temperature. *Phys. Rev. B* **75,** 155111. https://link.aps.org/doi/10.1103/PhysRevB.75.155111 (15 Apr. 2007).

106. Bardarson, J. H., Pollmann, F. & Moore, J. E. Unbounded Growth of Entanglement in Models of Many-Body Localization. *Phys. Rev. Lett.* **109,** 017202. https://link.aps.org/doi/10.1103/PhysRevLett.109.017202 (1 July 2012).

107. Serbyn, M., Papi, Z. & Abanin, D. A. Universal Slow Growth of Entanglement in Interacting Strongly Disordered Systems. *Phys. Rev. Lett.* **110,** 260601. https://link.aps.org/doi/10.1103/PhysRevLett.110.260601 (26 June 2013).

108. Huse, D. A., Nandkishore, R. & Oganesyan, V. Phenomenology of fully many-body-localized systems. *Phys. Rev. B* **90,** 174202 (2014).

109. Serbyn, M., Papi, Z. & Abanin, D. A. Local Conservation Laws and the Structure of the Many-Body Localized States. **111,** 127201 (2013).

110. Serbyn, M. *et al.* Interferometric Probes of Many-Body Localization. *Phys. Rev. Lett.* **113,** 147204. https://link.aps.org/doi/10.1103/PhysRevLett.113.147204 (14 Oct. 2014).

111. Imbrie, J. Z., Ros, V. & Scardicchio, A. Local integrals of motion in many-body localized systems. *Annalen der Physik* **529.** 1600278, 1600278–n/a. ISSN: 1521-3889. http://dx.doi.org/10.1002/andp.201600278 (2017).

112. Serbyn, M., Papi, Z. & Abanin, D. A. Quantum quenches in the many-body localized phase. *Phys. Rev. B* **90,** 174302. https://link.aps.org/doi/10.1103/PhysRevB.90.174302 (17 Nov. 2014).

113. Bahri, Y., Vosk, R., Altman, E. & Vishwanath, A. Localization and topology protected quantum coherence at the edge of hot matter. *Nature Communications* **6,** 7341 (2015).

114. Gopalakrishnan, S. *et al.* Low-frequency conductivity in many-body localized systems. *Phys. Rev. B* **92,** 104202. `http://link.aps.org/doi/10.1103/PhysRevB.92.104202` (10 Sept. 2015).

115. Serbyn, M., Papi, Z. & Abanin, D. A. Criterion for Many-Body Localization-Delocalization Phase Transition. *Phys. Rev. X* **5,** 041047. `https://link.aps.org/doi/10.1103/PhysRevX.5.041047` (4 Dec. 2015).

116. Altman, E. & Vosk, R. Universal Dynamics and Renormalization in Many-Body-Localized Systems. *Annual Review of Condensed Matter Physics* **6,** 383–409. eprint: `https://doi.org/10.1146/annurev-conmatphys-031214-014701`. `https://doi.org/10.1146/annurev-conmatphys-031214-014701` (2015).

117. See supplementary material.

118. Varma, V. K., Raj, A., Gopalakrishnan, S., Oganesyan, V. & Pekker, D. Length scales in the many-body localized phase and their spectral signatures. *arXiv preprint arXiv:1901.02902* (2019).

119. nidari , Relaxation times of dissipative many-body quantum systems. *Phys. Rev. E* **92,** 042143. https://link.aps.org/doi/10.1103/PhysRevE.92.042143 (4 Oct. 2015).

120. Levi, E., Heyl, M., Lesanovsky, I. & Garrahan, J. P. Robustness of Many-Body Localization in the Presence of Dissipation. *Phys. Rev. Lett.* **116,** 237203. https://link.aps.org/doi/10.1103/PhysRevLett.116.237203 (23 June 2016).

121. Fischer, M. H., Maksymenko, M. & Altman, E. Dynamics of a Many-Body-Localized System Coupled to a Bath. *Phys. Rev. Lett.* **116,** 160401. https://link.aps.org/doi/10.1103/PhysRevLett.116.160401 (16 Apr. 2016).

122. Lüschen, H. P. *et al.* Signatures of Many-Body Localization in a Controlled Open Quantum System. *Phys. Rev. X* **7,** 011034. https://link.aps.org/doi/10.1103/PhysRevX.7.011034 (1 Mar. 2017).

123. Van Nieuwenburg, E., Malo, J. Y., Daley, A. & Fischer, M. Dynamics of many-body localization in the presence of particle loss. *Quantum Science and Technology* **3,** 01LT02 (Dec. 2017).

124. Wootters, W. K. Entanglement of Formation of an Arbitrary State of Two Qubits. *Phys. Rev. Lett.* **80,** 2245–2248. https://link.aps.org/doi/10.1103/PhysRevLett.80.2245 (10 Mar. 1998).

125. Coffman, V., Kundu, J. & Wootters, W. K. Distributed entanglement. *Phys. Rev. A* **61,** 052306. `https://link.aps.org/doi/10.1103/PhysRevA.61.052306` (5 Apr. 2000).

126. Vasseur, R., Parameswaran, S. A. & Moore, J. E. Quantum revivals and many-body localization. *Phys. Rev. B* **91,** 140202. `https://link.aps.org/doi/10.1103/PhysRevB.91.140202` (14 Apr. 2015).

127. Bañuls, M. C., Yao, N. Y., Choi, S., Lukin, M. D. & Cirac, J. I. Dynamics of quantum information in many-body localized systems. *Phys. Rev. B* **96,** 174201. `https://link.aps.org/doi/10.1103/PhysRevB.96.174201` (17 Nov. 2017).

128. Eisert, J. Private communication.

129. R Core Team. *R: A Language and Environment for Statistical Computing* ISBN 3-900051-07-0. R Foundation for Statistical Computing (Vienna, Austria, 2013). `http://www.R-project.org/`.

130. Kivlichan, I. D. *et al.* Quantum Simulation of Electronic Structure with Linear Depth and Connectivity. *Phys. Rev. Lett.* **120,** 110501. `https://link.aps.org/doi/10.1103/PhysRevLett.120.110501` (11 Mar. 2018).

131. Vidal, G. & Werner, R. F. Computable measure of entanglement. *Phys. Rev. A* **65,** 032314. `https://link.aps.org/doi/10.1103/PhysRevA.65.032314` (3 Feb. 2002).